



Final Report November 7, 2017

Ice-Ex

Heat Exchanger Analyses for Ice Storages in Solar and Heat Pump Applications

Untersuchung von Eisspeicher-Wärmeübertragern für Solar-Wärmepumpen-Heizungen

Contracting body:

Swiss Federal Office of Energy SFOE
Research Programme Solar Heat and Heat Storages
CH-3003 Bern
www.bfe.admin.ch

Contractor:

Institut für Solartechnik SPF, Hochschule für Technik Rapperswil HSR
Oberseestr. 10
CH-8640 Rapperswil
www.spf.ch

Authors:

Dr. Daniel Carbonell, dani.carbonell@spf.ch
Mattia Battaglia, mattia.battaglia@spf.ch
Daniel Philippen, daniel.philippen@spf.ch
Dr. Michel Haller, michel.haller@spf.ch

SFOE Head of domain: Andreas Eckmanns, andreas.eckmanns@bfe.admin.ch
SFOE Programme manager: Dr. Elimar Frank, elimar.frank@frank-energy.com
SFOE Contract number: SI/501235-01

The author of this report bears the entire responsibility for the content and for the conclusions drawn therefrom.

Abstract

The combination of solar thermal and heat pump systems with ice storages, the so-called solar-ice systems, are becoming popular in Switzerland for the provision of space heating and domestic hot water. These systems can have a high efficiency, in the range of ground source heat pumps (GSHP) or higher, without being submitted to regulations of ground water protections. However, today's system cost are still higher than those from GSHP and research is needed to make solar-ice systems more efficient and cost competitive.

One approach to improve the efficiency and the investment cost of solar-ice systems is to optimize the heat exchanger area in the ice storage. Besides the aims of increasing the efficiency and reducing installation cost, an appropriate heat exchanger design can increase the ice fraction. The aim of the present project is to find suitable heat exchanger types and define the optimum heat exchanger area needed in the ice storage based on energetic and cost indicators.

This report is separated into six main chapters. Besides the first (Introduction) and the last (Conclusions) chapters, the report has four main chapters. Experimental results of different heat exchangers, i.e. capillary mats, flat plates and coils are presented in chapter 2. The mathematical description of an ice storage model able to cope with all experimentally analyzed heat exchangers is presented in chapter 3. In chapter 4, results from the validation of the model using the experimental data from chapter 2 are shown. The optimum heat exchanger area for the most promising heat exchangers was evaluated from a system perspective in terms of energetic efficiency and heat generation cost. The energetic simulations of the complete solar-ice system with varying heat exchanger type and area for different collectors areas and storage volumes is presented in chapter 5. In the same chapter, the cost effective heat exchanger area was evaluated and compared with state of the art ground source heat pump systems.

The main conclusions of this project can be summarized as follows. Very high ice fraction can be reached with all heat exchangers and the casing did not show any damage under high ice fraction conditions. This means that designing an ice storage able to reach an ice fraction up to 95% or higher should be safe. Therefore, the size of the ice storage, and thus the cost of the system, have the potential to be reduced. From all the heat exchanger analyzed, the most promising designs for small ice storages (below 5 m³) are polypropylene capillary mats (CM) and flat plates (PF) of stainless steel. From these two heat exchangers, capillary mats showed the best performance considering energetic and cost indicators. Solar-ice systems using ice storages volumes from 0.3 to 0.5 m³ per MWh of yearly heating demand, and selective uncovered collectors with 1.5 to 2.5 m²/MWh in the city of Zurich were able to achieve system performance factors SPF_{SHP+} ranging from 3.5 to 6 with both CM and FP in a single family house with 10 MWh of yearly demand. Considering the cost of the system, only simulations with CM were able to achieve lower heat generation cost than that of the GSHP with higher SPF_{SHP+} (an SPF_{SHP+} of 4 was assumed for GSHP). For example, a system with a collector area of 1.5 m²/MWh and an ice storage volume of 5 m³/MWh, can reach heat generation cost of 29 Rp./kWh, 0.5 Rp./kWh below the GSHP reference cost, with an increase of SPF_{SHP+} of 20 % respect to the GSHP system. However, there targets can only be achieved using CM and with the appropriate heat exchanger area. The optimal heat exchanger area was found to be around 5 to 6 m² per m³ of ice storage for CM and around 10 to 12 m²/m³ for FP. These heat exchanger ratios correspond to a distance between heat exchangers of around 12 - 17 cm for both CM and FP. These results were obtained assuming a conservative maximum ice fraction of 80 %.

Zusammenfassung

Die Kombination von solarthermischen Wärmepumpensystemen mit Eisspeichern, sogenannte solare Eisspeichersysteme, findet in der Schweiz immer mehr Beachtung. Diese Systeme können Raumwärme und Brauchwarmwasser mit vergleichbarer oder höherer Effizienz wie Erdsondenwärmepumpen zur Verfügung stellen. Allerdings sind die aktuellen Systemkosten im Vergleich nach wie vor höher, weshalb Forschungs- und Entwicklungsarbeit nötig ist, um solare Eisspeichersysteme effizienter und wirtschaftlich konkurrenzfähig zu machen.

Ein Ansatzpunkt zur Steigerung der Effizienz und der Wirtschaftlichkeit sind die im Eisspeicher verwendeten Wärmetauscher. Neben einer erhöhter Effizienz und günstigeren Beschaffungskosten kann ein gutes Wärmetauscherdesign auch den maximal möglichen Vereisungsgrad verbessern. Das Ziel des in diesem Bericht beschriebenen Projekts ist, geeignete Wärmetauschergeometrien und -materialien zu identifizieren und die optimale Wärmetauscherfläche in Abhängigkeit von energetischen und ökonomischen Zielfunktionen zu definieren.

Dieser Bericht ist in sechs Kapitel unterteilt. Das erste Kapitel gibt eine Einführung ins Thema. Die Schlussfolgerungen aus den Arbeiten sind im Kapitel 6 zusammengefasst. Die einzelnen Arbeitsschritte sind in den Kapiteln 2 bis 5 genauer beschrieben. Die experimentellen Resultate der untersuchten Wärmetauschertypen (Kapillarmatten, Wärmetauscherplatten und Wendelwärmetauscher) sind in Kapitel 2 aufgeführt. Das mathematische Modell, welches auf der Basis der Experimente entwickelt wurde, ist in Kapitel 3 beschrieben. In Kapitel 4 ist die Validierung des Modells mittels Daten aus den Labormessungen gegeben. Die Systemsimulationen des kompletten solaren Eisspeichersystems werden in Kapitel 5 präsentiert. Die optimale Wärmetauscherfläche wird dabei aus der Systemperspektive in Bezug auf Energieeffizienz und Wärmegestehungskosten bestimmt. Zusätzlich werden die erreichten Werte des Eisspeichersystems mit heutigen Erdsondensystemen verglichen.

Die Resultate des Projekts können folgendermassen zusammengefasst werden: Sehr hohe Vereisungsgrade wurden mit allen Wärmetauschertypen erreicht, wobei der Eisspeicherbehälter in keinem Experiment Schaden genommen hat. Daraus lässt sich schliessen, dass in einem geeigneten Behälter Vereisungsgrade von 95 % möglich sind, ohne dass Schäden zu erwarten sind. Der Verzicht auf nicht genutztes Eisspeichervolumen ist folglich eine Möglichkeit zur Kostenreduktion. Von den ausgemessenen Wärmetauschertypen zeigten Kapillarmatten und Wärmetauscherplatten aus Edelstahl die beste Performance für kleine Eisspeicher mit einem Volumen von unter 5 m^3 . Die besten Resultate betreffend Systemeffizienz und Kosten weissten dabei Kapillarmatten aus. Solare Eisspeichersysteme mit Eisspeichervolumina von 0.3 bis 5 m^3 pro MWh jährlicher Wärmebedarf und unabgedeckte Kollektoren mit einer Gesamtfläche von 1.5 bis $2.5 \text{ m}^2/\text{MWh}$ zeigten in den Simulationen mit Kapillarmatten und Plattenwärmetauschern Systemjahresarbeitszahlen $\text{SPF}_{\text{SHP+}}$ von 3.5 bis 6 . Die Resultate wurden für ein Einfamilienhaus mit 10 MWh jährlichem Wärmebedarf unter den klimatischen Bedingungen von Zürich generiert. Mit Blick auf die Wirtschaftlichkeit konnten lediglich mit Kapillarmatten Simulationsbedingungen gefunden werden, welche einen höheren $\text{SPF}_{\text{SHP+}}$ bei im Vergleich mit Erdsondensystemen geringeren Kosten ermöglichten. Beispielsweise hat ein System mit einer Kollektorfläche von $1.5 \text{ m}^2/\text{MWh}$ und einem Eisspeicher mit $5 \text{ m}^3/\text{MWh}$ Volumen Wärmegestehungskosten von 29 Rp./kWh . Dies ist 0.5 Rp./kWh günstiger als die Referenzkosten eines Erdsondensystems, wobei der $\text{SPF}_{\text{SHP+}}$ dabei um 20% höher lag. Die optimale Wärmetauscherfläche liegt für Kapillarmatten generell bei $5\text{-}6 \text{ m}^2$ pro Kubikmeter Eisspeichervolumen und für Wärmetauscherplatten bei $10\text{-}12 \text{ m}^2/\text{m}^3$. Dies entspricht in beiden Fällen jeweils einer Distanz zwischen den einzelnen Wärmetauschern von $12 - 17 \text{ cm}$.

Résumé

Les systèmes composés de panneaux solaires thermiques et d'une pompe à chaleur avec stockage de glace, appelés systèmes solaire à accumulateur de glace deviennent de plus en plus populaires pour le stockage thermique aussi bien de chauffage que de l'eau chaude sanitaire en Suisse. Ces systèmes ont une efficacité élevée, similaire voir supérieure à celle obtenue à l'aide d'une pompe à chaleur (PAC) à sonde géothermique et cela sans être soumis à la réglementation de protection des eaux souterraines. Cependant, ce type de système demeure actuellement plus coûteux que les PAC à sonde géothermique un développement est encore nécessaire afin de rendre les systèmes solaire à accumulateur de glace plus efficaces et leurs prix plus compétitifs.

L'une des approches pour améliorer l'efficacité et diminuer le coût d'investissement est d'optimiser la surface de l'échangeur de chaleur dans l'accumulateur de glace. En plus des objectifs d'augmentation de l'efficacité ainsi que de réduction du coût d'installation, une conception d'échangeur de chaleur appropriée peut également permettre d'augmenter la fraction de glace. Le but de ce projet consiste à trouver des échangeurs appropriés et à définir la surface d'échange optimale nécessaire dans l'accumulateur de glace en se basant sur des indicateurs énergétiques et financiers.

Ce rapport est divisé en six chapitres. Outre le premier chapitre (introduction) et le dernier (conclusion), le rapport comporte quatre chapitres principaux. Les résultats expérimentaux de différents échangeurs de chaleur (tapis capillaires, plaques plates et bobines) sont présentés dans le chapitre 2. La description mathématique d'un modèle de stockage de glace capable de fonctionner avec tous les types d'échangeurs de chaleur analysés expérimentalement est présentée au chapitre 3. Dans le chapitre 4, les résultats de la validation du modèle utilisant les données expérimentales du chapitre 2 sont exposés. La surface d'échange de chaleur optimale des échangeurs de chaleur les plus prometteurs a été évaluée à partir des perspectives en termes d'efficacité énergétique et du coût de production de chaleur. Les simulations énergétiques du système solaire à accumulateur de glace complet en fonction du type d'échangeur ainsi que de la surface d'échange pour différentes surface de collecteurs et différents volumes de stockage sont présentés au chapitre 5. Dans le même chapitre, un tel système a été évalué sur la base de l'échangeur le moins coûteux et comparé à un système standard de PAC à sonde géothermique.

Les principales conclusions de ce projet peuvent se résumer comme suit : Une importante fraction de glace peut être atteinte avec tous les échangeurs et aucun dégât n'a été engendré à l'enveloppe de l'accumulateur par une fraction de glace importante. Cela signifie qu'un système d'accumulateur de glace à même d'atteindre une fraction de glace égale ou supérieure à 95% devrait être sécuritaire. Par conséquent, la taille du stockage de glace et donc les coûts liés peuvent être réduits. De tous les échangeurs de chaleur analysés, les conceptions les plus prometteuses pour de petits accumulateurs de glace (inférieurs à 5 m^3) sont les tapis capillaires en polypropylène et les échangeurs à plaques en acier inoxydable. De ces deux échangeurs de chaleur, les tapis capillaires ont démontré les performances les plus élevées considérant les indicateurs énergétiques et de coût. Les systèmes solaire à accumulateur de glace utilisant des volumes de stockage de glace allant de 0.3 à 0.5 m^3 par MWh de demande annuelle de chauffage et des collecteurs sélectifs non-couverts avec 1.5 à $2.5 \text{ m}^2/\text{MWh}$ dans la ville de Zürich ont pu atteindre des facteurs de performance SPFSHP+ allant de 3.5 à 6 avec des échangeurs de type tapis capillaires ou échangeurs à plaques pour une maison familiale avec des besoins annuels de chauffage de 10 MWh . En tenant compte du coût du système, seules les simulations avec échangeurs de type tapis capillaires ont été capables de générer un coût de production de chaleur inférieur à une PAC à sonde géothermique avec un facteur de performance SPFSHP+ plus élevé (un $\text{SPF}_{\text{SHP}+}$ de 4 a été considéré pour la PAC). Par exemple, un système avec une surface de collecteurs de $1.5 \text{ m}^2/\text{MWh}$ et un volume d'accumulateur de glace de $5 \text{ m}^3/\text{MWh}$ peut atteindre un coût de production de chaleur de 29 Rp./kWh , soit 0.5 Rp./kWh de moins que le prix de référence d'une PAC à sonde géothermique, avec une augmentation de 20% du facteur de performance $\text{SPF}_{\text{SHP}+}$ par rapport à un système de PAC à sonde géothermique. Cependant, ces objectifs ne peuvent être atteints qu'en utilisant des échangeurs de type tapis capillaires et une surface d'échange de chaleur appropriée. La surface d'échange de chaleur optimale est d'environ 5 à 6 m^2 par m^3 de volume d'accumulateur de glace pour des échangeurs de type tapis capillaires tandis qu'elle est de 10 à 12 m^2 par m^3 pour les échangeurs à plaques. Ces rapports correspondent à des distances entre les échangeurs de chaleur d'environ $12 - 17 \text{ cm}$ pour des échangeurs de type tapis capillaires ou échangeurs à plaques. Ces résultats ont été obtenus en assumant une valeur de fraction de glace maximale conservative égale à 80% .

Contents

1	Introduction	1
1.1	Solar-ice systems for the provision of heating and domestic hot water	1
1.2	Heat exchangers for ice storages	3
2	Experimental analyses	4
2.1	Experimental set-up	4
2.2	Heat exchangers analyzed	4
2.2.1	Ice-on-coil	4
2.2.2	Ice-on-plate	7
2.3	Performance indicators	7
2.4	Uncertainty analyses	8
2.5	Methodology	9
2.6	Experimental results	9
2.6.1	Sensible heating (S1 and S2)	10
2.6.2	Sensible cooling (S3 and S4)	10
2.6.3	Solidification (S5)	11
2.6.4	Melting (S9)	13
2.6.5	Cycling (S8)	14
2.7	Conclusions	16
3	Mathematical modelling of the ice storage	16
3.1	Literature review on ice storage models	16
3.2	Mathematical formulation	18
3.2.1	Heat from/to the surroundings	18
3.2.2	Heat exchangers	18
3.2.3	Overall heat transfer coefficient	19
3.2.4	Ice solidification and melting on the heat exchanger	19
3.2.5	Constrained calculation	21
3.2.6	Comparison between ice constraintment models	24
3.3	Conclusions	25
4	Validation of the ice storage model	25
4.1	Quantified differences between experiments and simulations	26
4.2	Sensible heating cycle	26
4.2.1	Flat plates	27
4.2.2	Capillary mats	27
4.3	Cooling cycle	31
4.3.1	Flat plates	31
4.3.2	Capillary mats	32
4.4	Icing cycle	35
4.4.1	Flat plates	35
4.4.2	Capillary mats	37
4.5	Melting cycle	38
4.5.1	Flat plates	39
4.5.2	Capillary mats	42
4.6	Cycles of icing and melting	45
4.7	Conclusions	47
5	Solar-ice system simulations	47
5.1	Methodology	47
5.2	Hydraulic scheme of the simulated system	48
5.3	System control	49
5.4	Performance indicators	49
5.5	System energetic performance with varying heat exchanger type and area	49
5.6	Cost analyses of solar-ice systems	51
5.6.1	Heat generation cost	53

5.6.2	Installation cost	54
6	Conclusions	56
	Dissemination	58
	References	58

1. Introduction

The decarbonisation of the energy supply system should be a must-have goal at a world wide level to mitigate the climate change. The transformation towards a fossil fuel free energy system is one of the priorities of the European Commission (2012) which intends to reduce the annual greenhouse gas emissions in 2050 by 80% compared to the status of 1990. The Swiss Federal Council (2013) also proposed measures to reduce the environmental emissions at a national level. According to the European Technology Platform on Renewable Heating and Cooling (2013), the heating and cooling demand of the building stock was responsible in 2010 of 26% of the total EU energy demand. Therefore, in order to achieve the ambitious goals to decrease the GHG emissions by 80%, a special attention needs to be paid to sustainable solutions for heating and cooling of buildings.

1.1. Solar-ice systems for the provision of heating and domestic hot water

An efficient way to decrease the use of fossil fuels and greenhouse gas emissions for the provision of heating and cooling in buildings is to use a heat pump, preferably if combined with clean electricity. Heat pumps can have several heat sources, such as air, ground or solar. Air source heat pumps (ASHP) are cheap and easy to install. However, the efficiency is limited and sometimes the use of these devices are not socially well accepted or even prohibited due to the noise of the fan and the external heat exchanger aesthetics and space needs in the surroundings of the building. Ground source heat pumps (GSHP) have been used for heating and cooling in Switzerland since several decades in a very efficient way. The main disadvantages of GSHP compared to ASHP are the need for available ground to drill boreholes, possible conflicts with water protection laws, and the higher investment cost.

An alternative to those two solutions consists in using solar energy as a source for the heat pump. As long as the sun shines or the ambient temperature is not too low, solar collectors can be used as a source for the heat pump directly. However, during cold nights or day periods with low irradiation, the heat extraction from solar collectors might not be high enough to run the heat pump. When the solar collectors are not able to provide the amount of energy needed by the evaporator of the heat pump, the heat transfer fluid temperature circulating between the collectors and the evaporator will decrease until the minimum temperature accepted by the heat pump¹ is reached. Under those conditions the heat pump will stop for security reasons and the back-up (gas boiler, electrical heater, etc.) will be activated, thereby increasing the undesired non-renewable energy demand considerably. A significant reduction of the back-up heating will be achieved by enhancing the use of solar energy also in times during which collectors can only provide low-temperature heat. An increased usage of solar and ambient energy can be achieved by using an ice storage which can store low-grade heat with a high volumetric storage capacity. Besides solar collectors or ambient air, other sources such as waste heat, e.g. from waste water, can be used to provide the low-grade heat. The term *solar-ice* is used for systems that include solar collectors a heat pump as well as an ice storage. A solar-ice concept is therefore a system in which solar and ambient heat provided by the collector field are the only renewable sources for heating the building. This energy is mainly stored in the form of latent heat in the ice storage, which is then used as a temporary "source" for the heat pump. As discussed above, the use of ambient air in addition to solar heat, may be very important to avoid the use of back-up heating in cloudy periods. Therefore, it is relatively common to use uncovered collectors that, besides using solar energy, can work as air to brine heat exchangers too. If the system is aimed to have a high annual performance, then a selective coating of uncovered collectors is an advantage since it enables to provide heat at domestic hot water temperature levels, i.e. 50-60 °C.

Some of the frequently asked questions and answers concerning solar-ice systems are:

- "How can a solar-ice system, which is based on a 0 °C temperature source for the heat pump, perform better than a GSHP system which has usually a higher temperature source?" The main reason is that a solar-ice system can also use solar heat directly without the need of the heat pump. During times when solar heat is used directly, the system performance in terms of heat provided divided by electricity consumed can be up to fifty times higher compared to a GSHP system (only pumps consume energy). Moreover, since solar collectors are also used directly as a source for the heat pump, the source temperatures in solar-ice systems when the sun is shining can be considerably higher than in a GSHP.

¹Usually around -8 °C

- "Whats is the use of the ice? Can it be spared?" The key aspect of the solar-ice system concept relies on reducing the need of the storage volume by making use of the high latent heat of fusion released when ice is formed. Icing a specific quantity of water releases the same energy as cooling the same amount of water from 80 °C to 0 °C. Thus, although remaining always above the solidification temperature of water would lead to higher system performance, the required storage volume would be prohibitively large for this concept.

The principal idea of a solar-ice system is shown schematically in Fig. 1.1.

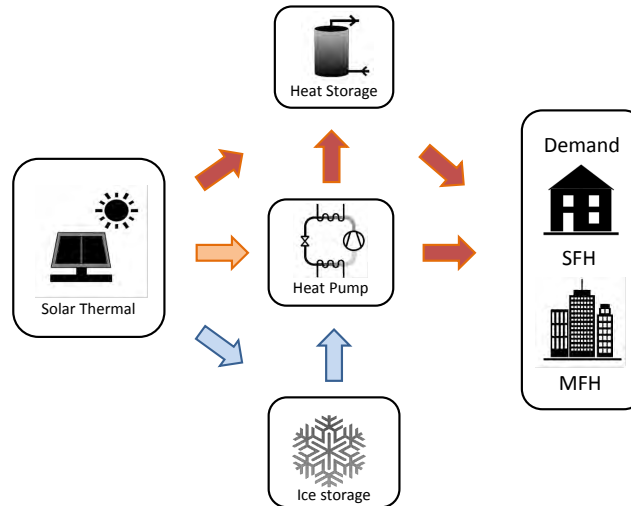


Figure 1.1: Principle concept of solar-ice systems. The arrows show the heat fluxes that are on different temperature levels, i.e. red, orange and blue for high ($>30\text{ °C}$), medium ($>10\text{ °C}$) and cold ($<10\text{ °C}$) respectively.

In summary, the following characteristics of ice storages are of interest for solar-ice systems (Carbonell et al., 2015):

- The use of phase change enthalpy in the ice storage leads to a high volumetric storage capacity, i.e. relatively small-sized ice storages can store a large amount of heat.
- The solar gains are significantly increased² due to the use of collectors at low temperatures (5-10 °C to melt the ice) and even lower ($< 0\text{ °C}$) as direct source for the heat pump.
- The impact on-site is low compared to other heat sources for heat pumps. No potential restrictions or risks for drilling boreholes as for GSHP and no aesthetics or acoustic impacts as for ASHP.
- The ice storage can be installed in different locations, e.g. buried in the ground or in the cellar of the building.
- If the ice storage is installed outside the building (especially if buried in the ground) a thermal insulation of the walls of the ice storage is not necessary.
- Ice storages usually gain heat from the surroundings, e.g. ground or cellar, during winter operation.
- Low-grade temperature heat sources like waste heat of e.g. exhaust air or waste water can deliver heat for melting the ice.
- The system design allows for flexibility, i.e. a lack of roof area can be compensated by larger ice storage volume and vice-versa.

²In solar-ice systems solar gains are usually two times larger than for state-of-the-art solar thermal systems

1.2. Heat exchangers for ice storages

Ice storages are a well proven technology for cooling applications where their main role consists in peak shaving of cooling loads at noon or in providing high cooling power for industrial processes (ASHRAE, 2007). In solar-ice systems less extraction power is needed because the ice storage serves as temporary heat source for a heat pump and not to cover peak demands. Therefore, ice storages in solar-ice systems, can be designed with less heat exchanger area per storage volume compared to cooling applications (Carbonell et al., 2016c). However, this is often not considered when companies that have been traditionally working for the cooling sector are trying to enter the solar heating market, designing the ice storage with the experience gained from cooling applications only.

In solar-ice applications, it is important to provide ice storages at low cost in order to be competitive with respect to alternative solutions such as boreholes for GSHP systems. In contrast to the typical use for cooling applications, a reduction of the capacity of the heat pump and peak load shaving are not relevant. Furthermore, ice storages have to be reliable to keep maintenance costs as low as possible.

Most of ice storages installed in Europe are based on ice-on-coil heat exchangers, and although other heat exchanger concepts exist on the market, their specific advantages and disadvantages remain unclear. Several heat exchanger concepts for extracting the latent heat from water can be used. Each concept has to ensure that the ice layer on the specific heat exchanger reaches thicknesses that are appropriate for the concept and do not result in too high heat transfer resistance, and thus, in too low source temperatures for the heat pump. When ice grows on the surface of the heat exchanger the overall heat transfer coefficient of the heat exchanger decreases. If ice is not actively removed, the heat exchanger design has to ensure that the heat transfer capacity will be enough at the maximum design mass ice fraction (see Eq. 3) or ice thickness on the surface of the heat exchangers. For example, let's assume that flat heat exchanger plates covering all the height of the ice storage are installed with a distance of 10 cm between each heat exchanger plate. If the heat transfer capacity with 3 cm of ice on the surface is not enough, the temperature of the heat transfer fluid will drop until the minimum temperature accepted by the heat pump is reached and the heat pump will be stopped for security reasons. If this occurs, the ice thickness can not exceed 3 cm and part of the latent storage capacity will be lost as 2 cm out of the theoretical maximum of 5 cm will not be used. Thus, the maximum ice fraction will never grow above 60 %. Therefore, if the heat exchanger area is too low and/or the distance between heat exchanger is too high, the desired maximum ice fraction may not be reached.

In principle, two main strategies exist for the design of heat exchangers for ice storages (Philippen et al., 2015):

- (a) **Ice-on-hx.** Typically large heat exchanger areas, homogeneously distributed throughout the whole storage volume, are necessary. Depending on the extraction power of the heat pump and on the specific characteristics of the heat exchanger, a maximum ice layer thickness ranging from several centimeters to few decimeters are typical. This maximum ice thickness determines the distribution of the heat exchanger in the storage volume and/or the volume itself. The following ice-on-hx are commonly used:
 - **Ice-on-coil:** coils or capillary mats typically made of any polymer that are mounted on a supporting structure (Jekel et al., 1993). Suppliers are e.g. Viesmann/Isocal, Fafco, Consolar, Calmac and Clina.
 - **Ice-on-plates:** flat plates made of plastic or stainless steel mounted on a supporting structure (Ismail et al., 1999). Suppliers are e.g. Energie Solaire, MEFA and BITHERM.
 - **Ice-in-spheres:** The ice storage is filled with plastic spheres with water inside (ice balls). The heat transfer fluid is pumped through the gaps between the spheres. Supplier e.g. Cristopia.
- (b) **Free-of-ice-hx.** Small heat exchanger in or outside the storage with prevention of ice formation on the heat exchanger or active removal of ice from the heat exchanger surface:
 - **Ice slurries technologies:** all ice slurry generators are avoiding the ice growth on the surface of the heat exchanger, either by a method that avoids that ice forms on the surface, e.g. by supercooling (Bédécarrats et al., 2010) or direct evaporation (Wijeysundera et al., 2004) or by actively removing the ice from the heat exchanger surface, e.g. by using scrapers (Kauffeld et al., 2005), fluidized beds (Pronk et al., 2003), supercooled water jets (Mouneer et al., 2010)

or by blowing compressed air (Zhang et al., 2008). From all these methods the most well known and established technology is the scraper type with suppliers such as Mayekawa Intertech.

- **Thermal de-icing.**

- **By hot gas:** the storage water is sprayed over a heat exchanger mounted above an open storage. A falling water film freezes on the heat exchanger which is periodically de-iced thermally by a hot gas. This system is known as an ice harvesting system (ASHRAE, 2007).
- **By solar thermal collectors :** flat immersed heat exchanger plates made of stainless steel are mounted vertically at the bottom of the storage. The plates are periodically de-iced thermally by low-grade solar heat. This method was firstly presented for solar heating applications by Philippen et al. (2012). The first ice storage model was developed and validated in Carbonell et al. (2015)) and compared to measured data of a pilot plant in Carbonell et al. (2016b,c). This method is on a demonstration phase level for solar-ice systems (Philippen et al., 2014).

From the above mentioned systems only the ice-on-hx concepts are established in the solar and heat pump heating market. The ice-on-coil and ice-on-plate concepts will be analyzed in the present project.

2. Experimental analyses

In the present chapter different heat exchangers designed to be installed into an ice storage for solar and heat pump heating applications have been experimentally investigated. Analyzed heat exchangers are capillary mats (CM), flat plates (FP) and coils (Coil) types. For CM and FP heat exchangers, different designs, materials and number of heat exchanger units have been evaluated. For the Coil type, only one heat exchanger set-up has been evaluated. For all heat exchangers two different mass flows have been used. This chapter aims at: i) characterizing different heat exchanger designs by means of measurements in a laboratory-size ice storage of 2 m³, ii) determine specific advantages and disadvantages of different heat exchanger concepts for ice storages used in combination with solar collectors and a heat pump and iii) provide a source of experimental data for model validation. Contents of this chapter have been published as Carbonell et al. (2016a).

2.1. Experimental set-up

The scheme of the experimental set-up is shown in Fig. 2.1. The inner dimensions of the ice storage are 2 x 1 x 1.3 m and it is insulated with 5 cm of Armaflex[®] ($\lambda = 0.041 \text{ W}/(\text{m} \cdot \text{K})$). The storage is filled with 2 m³ of water. The heating and cooling is provided by a chiller with approximately 6 kW heating and cooling power. Five Pt100 sensors are installed inside the storage for measuring the temperature at different heights. Three Pt100 sensors are installed at the inlet/outlet of the heat exchangers. An ultrasonic sensor is used to measure the height of the water level and to derive the total mass fraction of ice inside the storage. A volume flow sensor is installed and the volume flow is regulated by a PID control. A LabVIEW interface has been developed to run all testing sequences automatically.

2.2. Heat exchangers analyzed

2.2.1 Ice-on-coil

Two capillary mats (CM) from the manufacturer Clina, labeled as G-type and S-type, have been experimentally evaluated. All CM are made with the same kind of tubes and materials but have a slightly different design. From a practical point of view, when installing heat exchangers into an ice storage, it is desirable to have all header pipes on the upper side of the ice storage. For the S-type heat exchanger, the header pipe for flow and return are on the same side of the heat exchanger. Therefore, as can be seen in Fig. 2.2(b), the down-flow and up-flow on each tube are on the same plane when installed in the ice storage. On the other hand, G-type have one header pipe at the upper part of the hx (on a vertical view) and the other on the bottom part. Therefore, for installing G-types on the ice storage they need

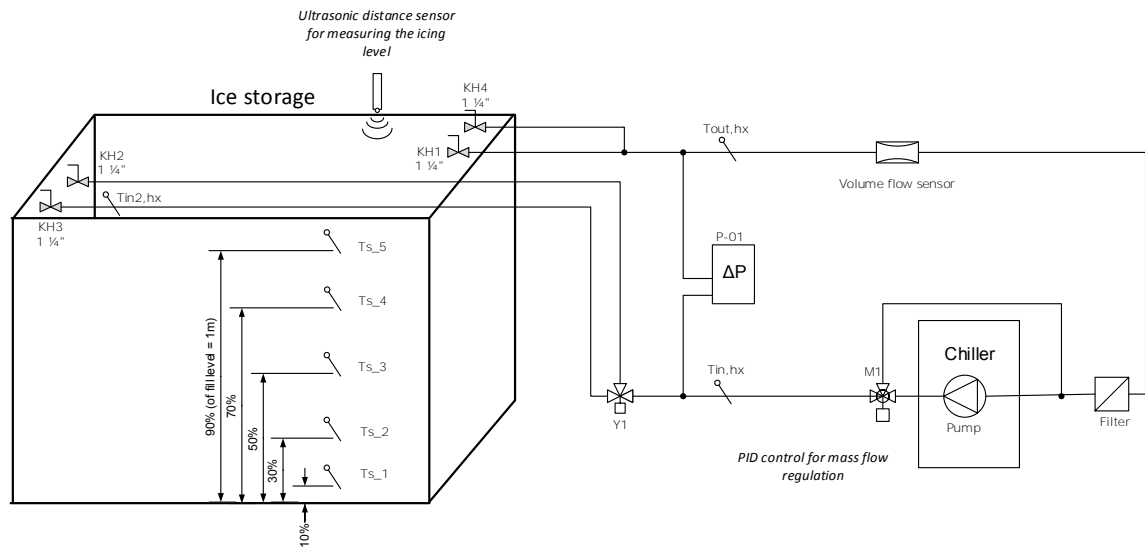


Figure 2.1: Hydraulic scheme of the experimental set-up with sensor locations.

to be bent and clipped in a U-shaped form as can be seen in Fig. 2.3(b). Thus, the length of the G-type needs to be twice the one from the S-type, leading to 22% more area per heat exchanger unit. Since the S-type does not need to be bent, it can be installed with approximately half the time compared to the G-type.

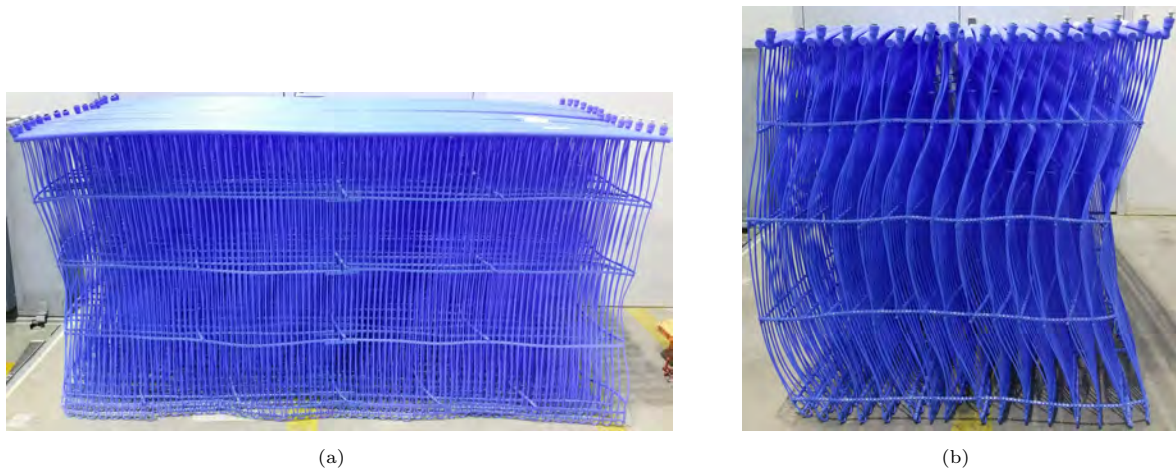


Figure 2.2: Picture of a capillary mat set-up with 16 heat exchangers of S-type in two perspectives (a) along the heat exchanger (b) between heat exchangers.

In order to keep the distance between heat exchangers and to stabilize the whole heat exchanger set-up, both the S-type and G-type designs need a plastic line where heat exchangers can be clipped. In G-type heat exchangers each U-bend was also clipped with the plastic line such that the distance between the down-flow and up-flow was equal to the distance to the following heat exchanger. The distance was kept constant for all the experimentally evaluated heat exchangers. Four clipping plastic lines were necessary between heat exchangers of S-type and G-type as can be seen in Fig. 2.2(b) and Fig. 2.3(b). In both designs, the capillary mats have been connected in parallel to the distribution pipes and are tested with two different numbers of heat exchangers, 16 and 8.

Another kind of heat exchanger, a custom made polypropylene coil heat exchanger (Coils) has been tested, which follows a similar approach as the Isocal ice storage. This heat exchanger is based on five



(a)



(b)

Figure 2.3: Picture of a capillary mat set-up with 8 heat exchangers of G-type in two perspectives (a) along the heat exchanger (b) between heat exchangers.

tubes that are bent and fixed in a supporting aluminum structure as can be seen in Fig. 2.4.

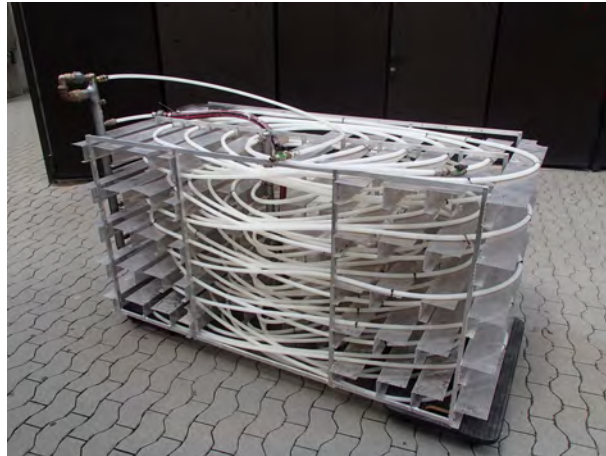


Figure 2.4: Picture of a custom-made coil heat exchanger (Coils) set-up with five coiled parallel tubes.

In total, four capillary mat combinations and one coil heat exchanger have been tested as shown in Table 2.1, where n_{hx} is the number of heat exchangers installed; n_{tubes} are the number of tubes per heat exchanger; L_{tube} is the length of each tube; d_i and d_o are the inside and outside diameters of the tubes respectively; A_{hx} is the total net external heat exchanger area; x_{tubes} is the distance between tubes in one heat exchanger and x_{hx} is the distance between heat exchangers. In the coil heat exchanger, the x_{hx} is considered to be the vertical distance between tubes on Fig. 2.4.

Table 2.1: Heat exchanger dimensions for capillary mats and coils.

Type	n_{hx} [-]	n_{tubes} [-]	L_{tube} [m]	d_i [mm]	d_o [mm]	A_{hx} [m ²]	x_{tubes} [mm]	x_{hx} [mm]
CM-Gtype-16hx	16	64	1.96	2.75	4.25	30.75	30	30
CM-Stype-16hx	16	96	0.98	2.75	4.25	24.06	20	60
CM-Gtype-8hx	8	64	1.96	2.75	4.25	15.38	30	60
CM-Stype-8hx	8	96	0.98	2.75	4.25	12.03	20	120
Coils	1	5	30.55	13	17	8.16	0-100	100

2.2.2 Ice-on-plate

Two different flat plate heat exchangers have been tested, one made of stainless steel (SS) from the manufacturer Energie Solaire and the other made of polypropylene (PP) from the manufacturer MEFA. The two flat plate types are shown in Fig. 2.5. The heat exchanger made from stainless steel have been tested with set-ups using 10, 8 and 6 units. The heat exchanger made of polypropylene was tested with 10 and 8 units³. The characteristic data of the heat exchangers is given in Table 2.2, where H_{hx} is the height of the heat exchangers.

Table 2.2: Data of the flat plate heat exchangers used in the experiments.

Type	n_{hx} [m]	L_{hx} [m]	H_{hx} [-]	A_{hx} [m ²]	x_{hx} [mm]
FP-SS-10hx	10	1.854	0.834	30.9	100
FP-SS-8hx	8	1.854	0.834	24.7	125
FP-SS-6hx	6	1.854	0.834	18.5	167
FP-PP-10hx	10	1.875	0.860	32.2	100
FP-PP-8hx	8	1.875	0.860	25.8	125



(a)



(b)

Figure 2.5: Picture of two flat plates experimentally evaluated made of (a) polypropylene (b) stainless steel.

2.3. Performance indicators

For each test sequence several indicators are calculated from measured data. The heat exchanger power \dot{Q} is calculated as:

$$\dot{Q} = \dot{m}c_p(T_{f,out} - T_{f,in}) \quad (1)$$

where \dot{m} is the mass flow, c_p the specific heat capacity and T_f the heat transfer fluid (glycol) temperature. The cumulative energy for the whole test sequence until the time t is calculated as:

$$Q = \int_{t=0}^t \dot{Q} \cdot dt \quad (2)$$

where t is the time. The integral is discretized using a time step dt of 10 seconds. The mass ice fraction is calculated as the ratio between the mass of ice and the total amount of water and ice of the storage.

$$M_r = \frac{M_{ice}}{M_T} \quad (3)$$

³Six units were not tested due to the very low performance expected from this set-up

The ice fraction is experimentally evaluated measuring the change of height of water due to the volume change between water and ice. For some processes, e.g. melting cases where the initial ice fraction is very large and the ice is above water level, the mass of ice can not be accurately obtained from experiments and therefore it is calculated from the energy exchanged between the heat exchangers and the storage, neglecting heat gains from the surroundings through the storage walls. Ice fraction results that are calculated from the exchanged energy are labeled as M_r^* .

The global heat transfer rate of the heat exchanger UA is obtained from:

$$UA = \frac{\dot{Q}}{LMTD} \quad (4)$$

where the logarithmic mean temperature difference LMTD is calculated as:

$$LMTD = \frac{(T_{f,out} - T_{w,av}) - (T_{f,in} - T_{w,av})}{\ln\left(\frac{T_{f,out} - T_{w,av}}{T_{f,in} - T_{w,av}}\right)} \quad (5)$$

where $T_{w,av}$ is the averaged water temperature in the storage. As long as ice exists in the storage, $T_{w,av}$ is assumed to be 0 °C.

The heat transfer coefficient of the heat exchanger is calculated as:

$$U = \frac{UA}{A_{ext}} \quad (6)$$

where A_{ext} is the external surface area of the specific heat exchanger analysed.

2.4. Uncertainty analyses

In the measurement procedure, there are different uncertainties that affect the confidence interval of the results. In order to obtain a high precision, the 4-wire Pt100-temperature sensors (Class A) have been calibrated for the temperature range of the test cycles (from -10 °C to 40 °C). Based on the calibration, the output values of each temperature sensor were corrected according to a 1st order polynomial. The remaining uncertainty of the Pt100 sensors after calibration was in the order of 0.03-0.04 K. An electromagnetic flow meter that has been calibrated for volume flows between 500 and 1400 l/h was used for volume flow rate measurements. The relative uncertainty of the volume flow rate measurement after the calibration of the flow sensor was determined to be 0.6 %. For the glycol concentration, an acceptable range of 31.9 %-34.7 % has been defined. The maximal relative uncertainty of the mixture's specific heat capacity is then estimated with respect to this range and the uncertainty of the temperature measurement. For the analyzed experimental data it was generally smaller than 1.3%. These uncertainty values are used to calculate the total uncertainty of the derived values such as power or heat transfer coefficient.

The power extracted from the ice storage by the heat exchangers is calculated by:

$$\dot{Q} = c_p \rho \dot{V} \Delta T = c_p \rho \dot{V} (T_{out} - T_{in}) \quad (7)$$

This equation consists only of multiplications. Therefore, the uncertainty of the power can be calculated by:

$$\left(\frac{u\dot{Q}}{\dot{Q}}\right)^2 = \left(\frac{u\dot{V}}{\dot{V}}\right)^2 + \left(\frac{u\rho}{\rho}\right)^2 + \left(\frac{uc_p}{c_p}\right)^2 + \left(\frac{u\Delta T}{\Delta T}\right)^2 \quad (8)$$

The error of the cumulative energy over a testing sequence can be computed by the sum of the uncertainties of the power weighted with the length of the measurement time steps.

$$uQ^2 = \sum_{\bar{i}=0}^t u\dot{Q}^2 \cdot \Delta t \quad (9)$$

The heat transfer coefficient rate (UA-Value) is calculated by Eq. 4, where $T_{storage}$ is measured also with five Pt-100 temperature sensors. The total uncertainty of UA is then calculated by:

$$\begin{aligned}
uUA^2 &= \left(\frac{\partial UA}{\partial T_{out}}\right)^2 \cdot (uT_{out})^2 + \left(\frac{\partial UA}{\partial T_{in}}\right)^2 \cdot (uT_{in})^2 \\
&+ \left(\frac{\partial UA}{\partial T_w}\right)^2 \cdot (uT_w)^2 + \left(\frac{\partial UA}{\partial \dot{V}}\right)^2 \cdot (u\dot{V})^2 \\
&+ \left(\frac{\partial UA}{\partial c_p}\right)^2 \cdot (uc_p)^2 + \left(\frac{\partial UA}{\partial \rho}\right)^2 \cdot (u\rho)^2
\end{aligned} \tag{10}$$

The ice fraction is calculated from the total Volume $V_{tot} = 2 \cdot 1 \cdot h_{tot}$ of the ice water mixture as

$$M_r = 100 \cdot \frac{\rho_{ice}}{m_0} \cdot \frac{m_0 - \rho_w V_{tot}}{\rho_{ice} - \rho_w} \tag{11}$$

The variable m_0 describes the total mass that was filled into the ice storage at the beginning of a test cycle. The uncertainty related to the ice fraction values is then:

$$uM_r^2 = \left(\frac{\partial M_r}{\partial h_{tot}}\right)^2 \cdot (uh_{tot})^2 + \left(\frac{\partial M_r}{\partial m_0}\right)^2 \cdot (um_0)^2 + \left(\frac{\partial M_r}{\partial \rho_{ice}}\right)^2 \cdot (u\rho_{ice})^2 \tag{12}$$

The uncertainty of m_0 was determined by the difference of the mass value displayed by the flow meter at the water inlet of the ice storage and the value that has been derived from the height measurement. The uncertainty of the ice density was estimated by computing the difference of the ice density at average storage temperature and at 0 °C. It is assumed that all the water is at 0 °C and therefore, ρ_w is not affected by any uncertainty when ice is present.

The relative uncertainty of the extracted power is in the order of 2 %. The calculated heat transfer coefficient is affected by an uncertainty that ranges from 2.5 % up to 14 %. High uncertainty values are caused by small temperature differences when the ice storage temperature approaches the chiller set point temperature and therefore the heat exchanger's inlet and outlet temperature are close together. Thus, system operating points with significant energy transfer are not affected by large uncertainty values. The ice fraction calculation was computed based on the changing water level in the storage tank when ice is formed or melted. The ultrasonic sensor has a precision of 0.5 mm which results in an uncertainty of the icing fraction in the order of 0.5% - 1%.

2.5. Methodology

In order to test the heat exchangers an experimental sequence has been defined and programmed in LabView. The testing sequence is summarized in Table 2.3. All heat exchangers have been tested with two volume flows regulated with a PID control (1000 l/h and 2000 l/h). Each test lasted around one week for each mass flow and a total of ten heat exchanger set-ups have been evaluated.

Table 2.3: Testing sequences considered for each heat exchanger.

Test phase	Name	Mass Flow	T_{set} of the chiller	Begin of sequence	End of sequence
Sensible heating	S1	1000 l/h	20 °C	Storage at 10 °C or end of S8	steady state
	S2	2000 l/h	40 °C		End of S1
Sensible cooling	S3	1000 l/h	-10 °C	End of S1	$T_{s,av} \approx 0$ °C
	S4	2000 l/h	-10 °C	End of S2	$T_{s,av} \approx 0$ °C
Solidification	S5	1000-2000 l/h	-10 °C	End of S3 or S4	$V_r \approx 95\%$ (or 3 days)
Cycling : Ice/melt	S6	1000-2000 l/h	-10 °C (40 min) 10 °C (20 min)		
Melting	S7	1000-2000 l/h	10 °C	End of S8	steady state

2.6. Experimental results

The experimental results are split into sensible heating, sensible cooling, icing, melting and cycling of icing/de-icing. Results for flat plates made of polypropylene with a volume flow of 1000 l/h are not shown in the following sections because problems with flow distribution were detected.

2.6.1 Sensible heating (S1 and S2)

The overall heat transfer coefficients (U) for sensible heating processes are shown in Fig. 2.6 . Circle marks are for 2000 l/h and for S2, i.e. the storage is heated from 20 °C to 40 °C. Filled triangles are for 1000 l/h and for S1, i.e the storage is heated from 10 °C to 20 °C.

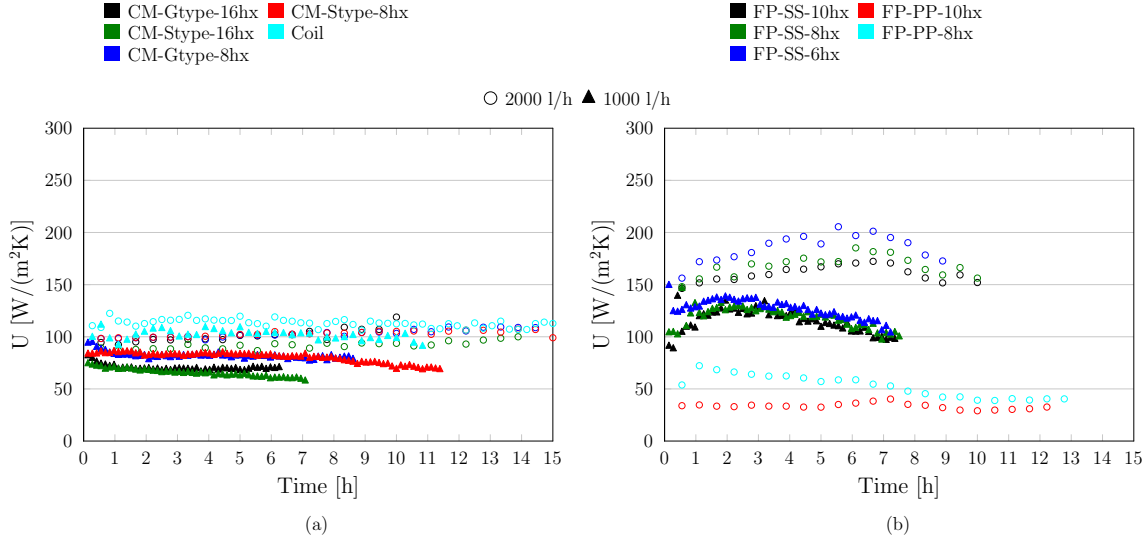


Figure 2.6: Overall heat transfer coefficient results for sensible heating sequences S1 and S2 for (a) ice-on-coil heat exchangers and (b) ice-on-plate heat exchangers. Circle marks are for 2000 l/h and S2 (heating from 20 °C to 40 °C) and filled triangles are for 1000 l/h and S1 (heating from 10 °C to 20 °C).

FP-SS show better capabilities for providing energy to the storage by means of sensible heat. For a flow rate of 2000 l/h, U is in the range of 90-110 $W/(m^2K)$ for CM heat exchangers and between 150-200 $W/(m^2K)$ for FP with SS. For 1000 l/h U values are decreased to values between 70 and 90 $W/(m^2K)$ for CM and to 100-140 $W/(m^2K)$ for FP-SS approximately. Coils shows the best performance of the ice-on-coil solutions with around 100-120 $W/(m^2K)$ for 1000 l/h and 2000 l/h respectively. However, the total area of Coils is substantially lower than that of CM and usually low A_{hx} shows better performance per m^2 of heat exchanger area due to the higher temperature difference at the end of the heat exchanger.

The main difference between the two designs of capillary mats, G and S types, is the heat exchanger area as U values are very similar. FP-PP show a much lower performance compared to FP-SS and the performance of ice-on-coil heat exchangers is better than the one of FP-PP but worse than the one of FP-SS. Except for FP-SS, the performance of all heat exchangers remains relatively constant during the heating process, even though the Reynolds number (Re) increases due to the lower viscosity of the fluid when it is heated. During the whole test sequence the Re number remains below 400 for 2000 l/h and below 150 for 1000 l/h and therefore it is theoretically always in a laminar regime. In a laminar flow regime the Nusselt number is relatively constant and thereby the performance of the heat exchangers are not affected by the increase of Re during the heating process and only slightly due the change of volume flow. However, FP-SS are significantly affected by the mass flow, probably because their special design enhances turbulence. Thanks to this special design, the flow is turbulent at lower Re number as compared to smooth pipes. Therefore, flow regimes are most of the time in the transition regime between laminar and turbulent. This means that the Nusselt number and, as a consequence, the heat transfer coefficient, are affected by the Re number.

2.6.2 Sensible cooling (S3 and S4)

Overall heat transfer coefficients for the sensible cooling process are shown in Fig. 2.7. Circle marks represent a volume flow of 2000 l/h and a test sequence S4 in which the storage temperature is cooled from 40 °C to 0 °C. Triangle marks represent a volume flow of 1000 l/h and a test sequence S3 in which the storage temperature is cooled from 20 °C to 0 °C.

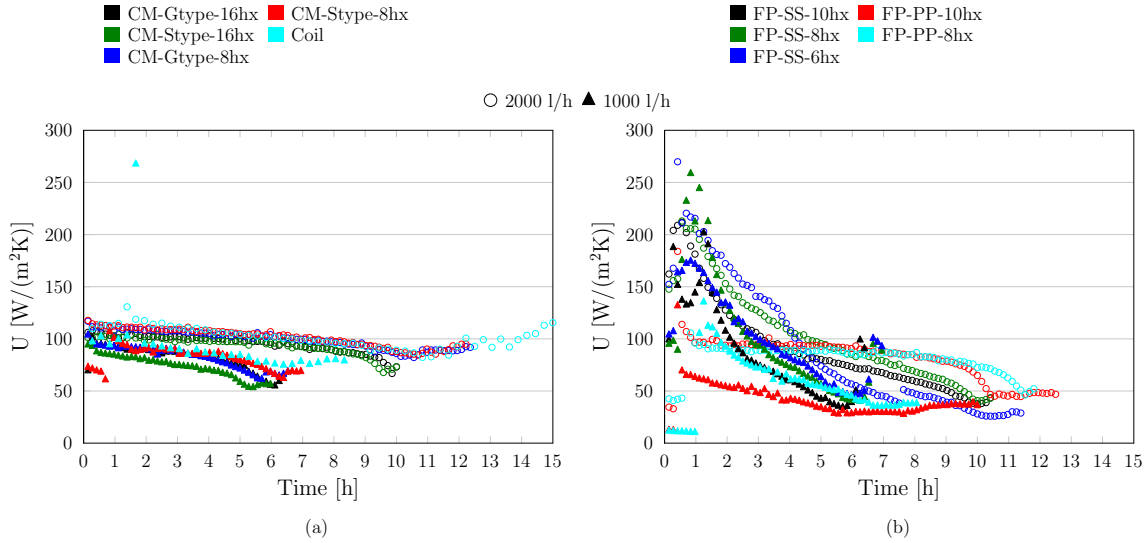


Figure 2.7: Measured overall heat transfer coefficients for sensible cooling sequences S4 for (a) ice-on-coil heat exchangers and (b) ice-on-plate heat exchangers. Solid lines are for 2000 l/h and the cycle starts at T_s of 40 °C; dashed lines are for 1000 l/h and the cycle starts at T_s 20 °C.

The overall heat transfer coefficient shows a different behavior for ice-on-coil heat exchangers and FP-SS. For FP-SS, the U values decrease significantly with time. For CM the U values remain approximately constant for a large time period. The reason for that is the same as given in section 2.6.1, i.e. ice-on-coil heat exchangers are always in a laminar regime while FP-SS are in the turbulent and transition regime. In this case, the Re number decreases along the sequence because the fluid's viscosity increases when cooled down to 0 °C. At the beginning of the test sequence, FPs perform significantly better than the ice-on-coil heat exchangers, and the opposite is true at the end of the test sequence. The U values range from 120 to 75 W/(m²K) for 2000 l/h and from 100 to 60 W/(m²K) for 1000 l/h when ice-on-coil heat exchangers are used; and they range from 220 to 40 W/(m²K) for 2000 l/h and from 175 to 40 W/(m²K) using 1000 l/h when FP-SS are used. The evolution of U along time for FP-PP is similar to the one observed with ice-on-coil heat exchangers when 2000 l/h are used. The U values are relatively constant and in the range of 100 W/(m²K) for a large period. The efficiency of the heat exchangers is reduced when the storage water temperature is close to 0 °C.

2.6.3 Solidification (S5)

The amount of ice produced for all heat exchangers are shown in Fig. 2.8. Usually, capillary mats freeze the water of the storage faster compared to flat plates. Coils have a lower rate of icing due to the lower heat exchanger area (see Table 2.1). Ice fractions of 95 % and above are achieved. Due to the specific height of the FP used in the experiments, only 85% of the storage height was covered by the heat exchangers, limiting its capacity to ice the whole storage. However, flat plate heat exchangers can be used to achieve very high ice fractions (above 95%). Mass ice fractions higher than 85% with FP are possible. However, above 85 %, the U value is very low since ice has to grow on the surface of a compact ice cube that includes all plates and thus, the path between the heat transfer fluid in the heat exchanger and liquid storage water is long. For FP, ice fractions above 90% were achieved. During the icing experiments and also at the maximum ice fractions up to 100% no damaging of the casing could be observed with any of the heat exchangers used.

The overall heat transfer coefficient is shown in Fig. 2.9 as a function of the ice fraction. The reference area for the calculation of the heat transfer coefficient is the external heat exchanger area, as in all the other cases. From this graph, it can be observed that the decrease of U for ice-on-coil heat exchangers is much smaller compared to FP. Considering the ideal case of ice growing on a single tube, the higher thermal resistance of the ice layer when ice grows is partially compensated by the higher contact area between the outside of the growing ice radius and the surrounding water. Therefore, the heat transfer rate UA remains relatively constant when ice grows on a cylinder (Carbonell et al., 2015). However, ice-

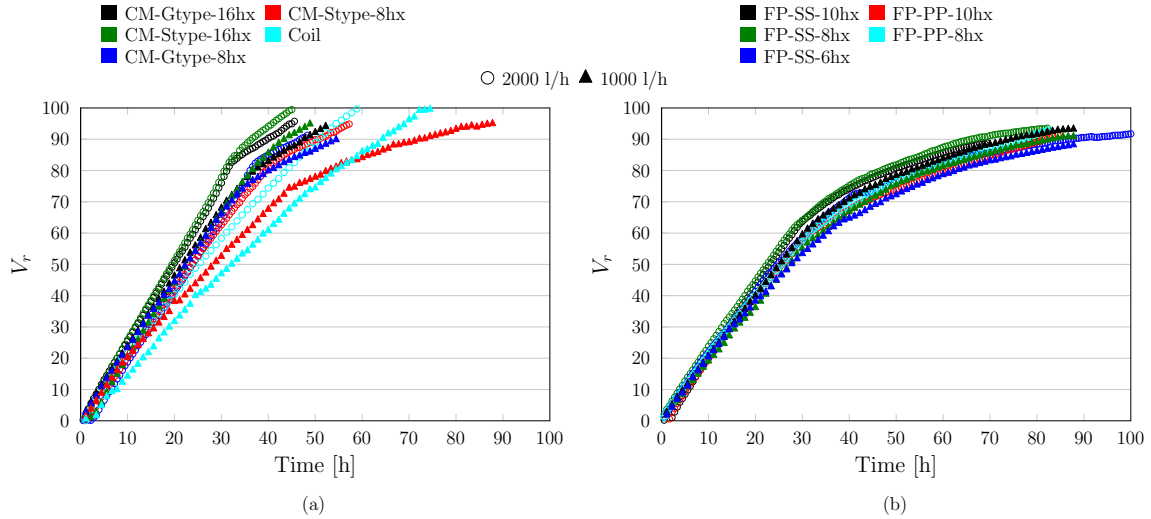


Figure 2.8: Evolution of mass ice fraction over time for the icing sequence S5 for (a) ice-on-coil heat exchangers and (b) ice-on-plate heat exchangers.

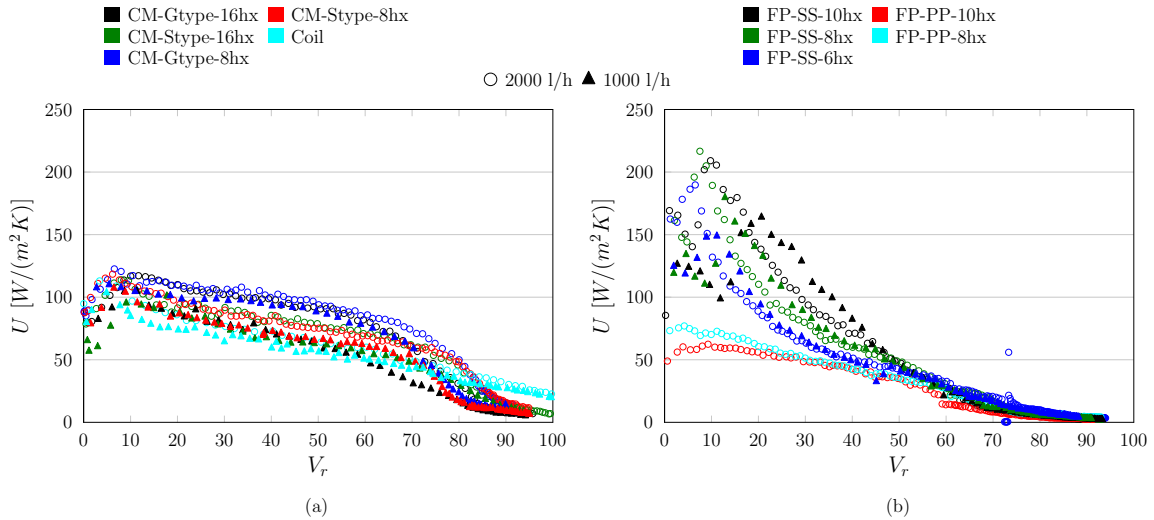


Figure 2.9: Measured overall heat transfer coefficients as a function of the ice fraction for the icing sequence T5 for (a) ice-on-coil heat exchangers and (b) ice-on-plate heat exchangers.

on-coil heat exchangers are composed of many tubes and the ideal one-dimensional growing on a single tube is only valid until growing of ice from neighboring tubes contact with each other. For example, for the S-type, the distance between tubes in one heat exchanger is 20 mm. Assuming that ice grows homogeneously on all pipes and along the whole pipe length, ice layers start to touch to each other within one heat exchanger when V_r is approximately 27% and 14% for 16 hx and 8 hx respectively. For G-type, the distance between pipes is 30 mm, this means that ice layers between pipes touch when the ice fraction is approximately 80% and 40% for 16 hx and 8 hx, respectively.

The consequences of physical contact between ice layers is usually called constrained ice growing (Jekel et al., 1993). For all CM, the heat exchangers undergo of a two step constrained ice growing, the first one when the ice is constrained within one heat exchanger (ice between adjacent tubes touch each other) and the second when ice is constrained between neighboring heat exchangers. When ice growing is constrained the overall heat transfer coefficient decreases compared to the unconstrained case because the contact area between the growing ice and surrounding storage water decreases. However, in the experimental results it is not possible to observe a sharp decrease of the U value when ice constraint occurs because ice grows unequally along the length of each tube and thus the constraint of ice growth starts at the

cold inlet and progresses slowly towards the end over a long period.

For FP, ice starts to be constrained when the ice thickness is half the distance between heat exchangers. In the experiments shown here, this corresponds always to an ice fraction of approximately 83%. At these conditions all water between heat exchangers is frozen and ice can only grow on the surface of a solid cube of ice with very low U values. Comparing all heat exchangers one can observe that for low ice fractions the U values of FP-SS are higher. However, the decrease of the U value when ice grows is much more pronounced for FP-SS compared to ice-on-coil heat exchangers. As stated before, the contact area between ice and water increases when ice grows in ice-on-coil heat exchangers. Instead, for FPs the ice surface area remains approximately constant and the U value decreases rapidly. For FP with PP, the decrease of efficiency is much less pronounced in comparison to SS because the heat transfer resistance of the polypropylene is the limiting factor, in comparison to the FP-SS, where the ice thickness is the limiting factor.

2.6.4 Melting (S9)

The energy delivered for melting the ice is shown in Fig. 2.10. Melting 2 m^3 of water needs about 185 kWh. On top of that, the energy needed to heat the sub-cooled ice to $0 \text{ }^\circ\text{C}$ and the sensible heat to raise the temperature from $0 \text{ }^\circ\text{C}$ to $10 \text{ }^\circ\text{C}$ needs to be considered. Comparing CM with FP one can observe

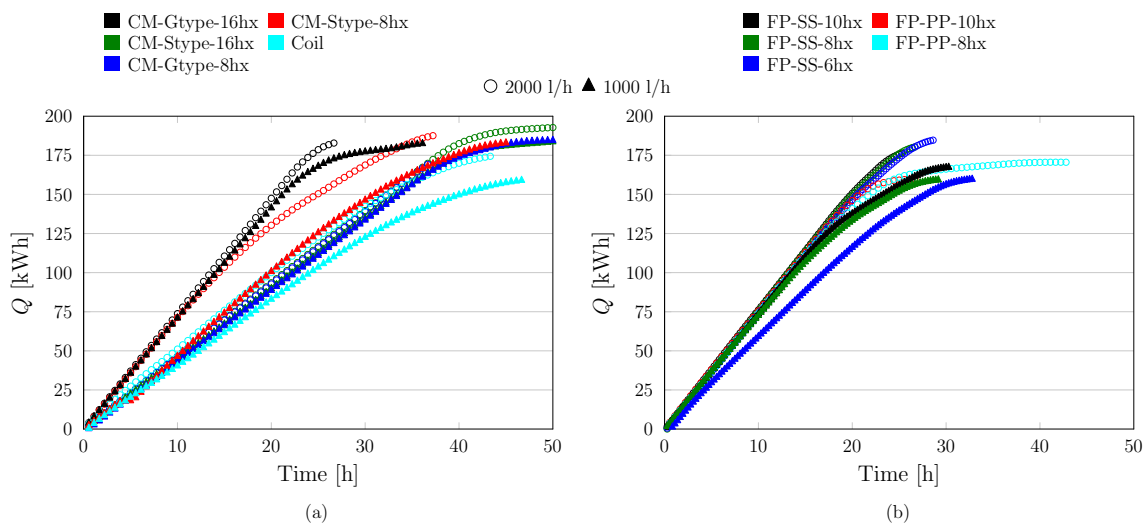


Figure 2.10: Energy delivered to the storage by the heat exchangers for the melting sequence S9 for (a) ice-on-coil heat exchangers and (b) ice-on-plate heat exchangers.

that FP-SS are usually able to melt completely the ice in less time. The measure for the ice fraction for capillary mats was not accurate with the method used in these experiments. A water layer above the ice block was not always present at high ice fraction ($\geq 95\%$) and the measurement of solid ice was disturbing the accuracy. Because the flat plates had a layer of 17 cm of water above them, the measurement of the melted ice was much more accurate. However, even in this case, with the method used, it is not possible to measure the ice fraction until the melted ice connects with the water of the storage. Ice is melted around the heat exchangers forming a cavity of liquid water. Before this cavity of melted ice connects to the bulk water, the change of density when the ice is melted creates an under-pressure around the heat exchangers that would either expand the heat exchanger or evaporate part of the water until the change of volume is filled.

Overall heat transfer coefficients are shown in Fig. 2.11. FP-SS have the highest melting capacity at high ice fractions with values above $250 \text{ W}/(\text{m}^2\text{K})$. For ice fractions below 60% the U values reduce to $50\text{-}60 \text{ W}/(\text{m}^2\text{K})$ for FP-SS. For ice-on-coil heat exchangers, the U values are more stable over the whole melting process with values between $50\text{-}80 \text{ W}/(\text{m}^2\text{K})$.

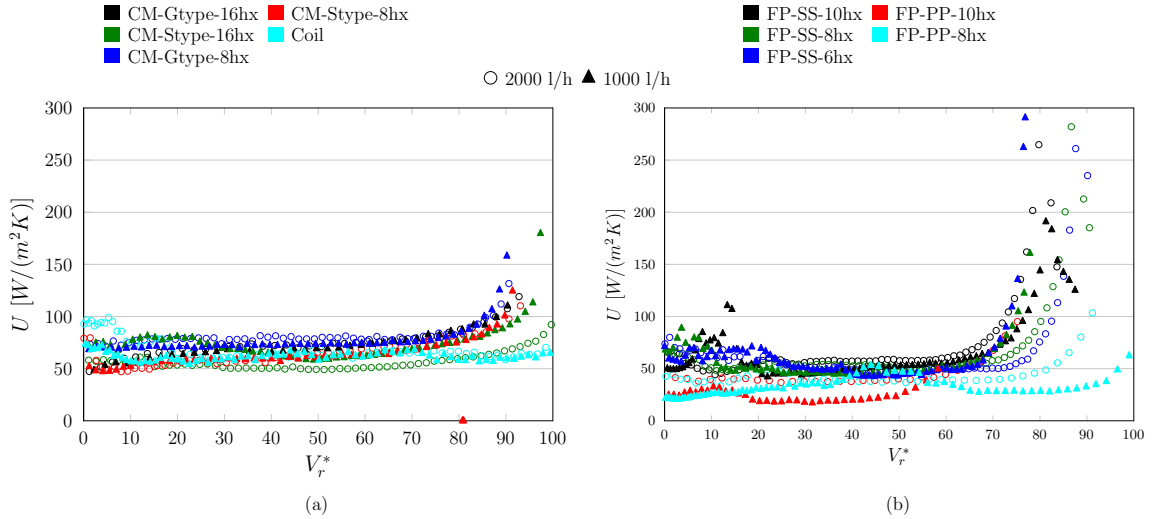


Figure 2.11: Overall heat transfer coefficient for melting sequence S9 for (a) CM and (b) FPs.

2.6.5 Cycling (S8)

The cycling experiment consist of 10 sequences of heating and cooling which are used for melting and icing. This test sequence is performed at a very high ice fraction after the icing sequence S5. Each cycle is performed with a constant time of 20 min for heating and 40 min for cooling. All experiments with CM were tested with cycles always in the subcooled zone (ice temperature was below 0 °C) and therefore melting was not always achieved. For this reason the test control was changed such that it heats up the storage until the outlet of the heat exchanger is close to zero before cycling starts. In this way it is ensured that ice is melted and solidified during each cycle. As an example, results for cycling sequences are presented in Fig. 2.12 for FP with 10 hx. For all the cycles the inlet temperature of the heat exchangers increases above 0 °C, which means that it is always possible to melt ice, at least at the entrance of the heat exchangers. For the first four cycles, the outlet temperature remains at 0 °C, which means that ice is never subcooled at the end of the heat exchanger. After the first cycles, the outlet temperature starts to drop below 0 °C which means that ice is subcooled, and the UA values are reduced because the heat of fusion is not released along the whole length of the hx.

The danger of breaking the casing of the storage is potentially higher when cycles of melting and icing are performed at high ice fractions. In normal icing conditions without any cycles, the solid ice will always push the liquid water to the surface. Therefore, as long as there is an escape way for the water, there is no risk for the casing. The problem may occur when a volume of water in contact with the casing is trapped within an ice block. If then this water is iced, the volume expansion will produce a strong force to the wall of the casing with the danger of breaking it. This situation may occur when the dynamics of the system are on a specific state, which however was never the case in the lab.

In this test several cycles of melting and icing have been performed at very high ice fractions in order to test the robustness of the heat exchangers under these dynamic conditions. The mechanical stress that was caused by the dynamics of icing and melting was neither found to be a problem for the heat exchangers nor for the storage casing. However, long term tests should be performed to investigate the robustness and stability.

The cycling sequence will also be very useful for the validation of the ice storage model (see chapter 4), since in each cycle different physical phenomena take place. Fig. 2.13 shows one cycle of melting and icing for FP-SS with 10 hx (zoom into Fig. 2.12). The sequence has been split into five zones, from I to V as shown in Fig. 2.13. Zones I to II correspond to heating/melting and zones III to V correspond to cooling/icing.

- Zone I : switch from cooling to heating.
- Zone II: the ice is heated from the subcooled state to 0 °C and melted starting from the entrance of the heat exchangers. Most likely, melting does not occur over the whole length since the outlet

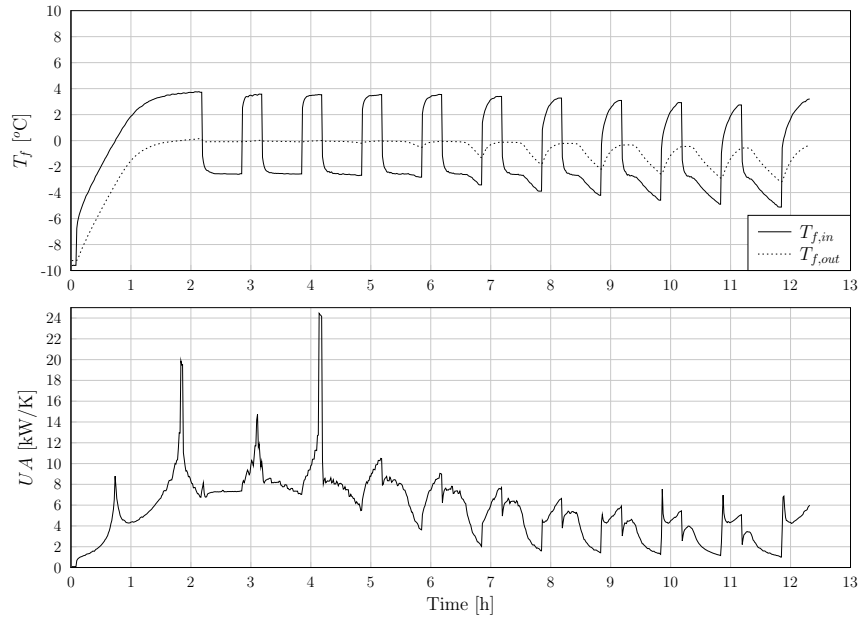


Figure 2.12: (a) Heat exchanger temperatures and (b) overall heat transfer rate UA for cycling sequence S8 and FP.

temperature does not increase above 0 $^{\circ}\text{C}$.

- Zone III: cooling of the water until freezing conditions.
- Zone IV: icing of the water.
- Zone V: subcooling of ice.

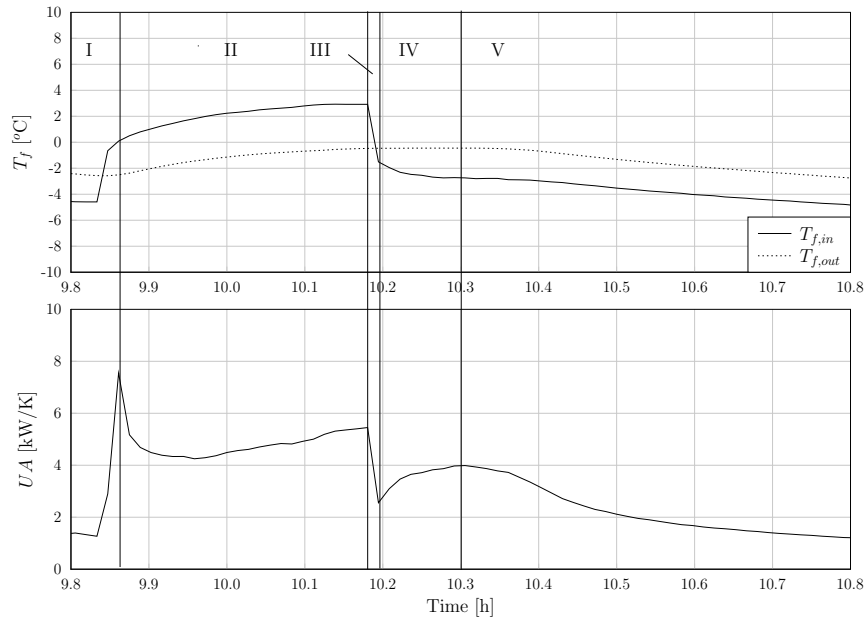


Figure 2.13: (a) Heat exchanger temperatures and (b) heat transfer rate for cycling sequence T8 and FP.

2.7. Conclusions

In the present chapter results of several heat exchangers have been analyzed, including capillary mats with different designs made of polypropylene, polypropylene coils and flat plates made of stainless steel and polypropylene. The area analyzed has been modified for each heat exchanger and all test have been performed using two different mass flow rates. In total, nine possibilities have been experimentally evaluated for several test sequences including sensible heating and cooling, icing, melting and cycling. The main conclusions of this experimental study can be summarized as:

- Very high ice fraction can be reached with all heat exchangers and mass flows.
- The casing did not show any damage under high ice fraction conditions. This means that designing an ice storages able to reach 95% ice fraction or higher should be safe.
- All heat exchangers showed to be reliable and robust under the test conditions. Long term tests were not carried out.
- Flat plates made of stainless steel are better suited compared to capillary mats or coils for sensible heating and cooling and for melting processes.
- Capillary mats or coils are better suited compared to flat plates for the icing process due to the strong decrease of performance that flat plates suffer when ice grows.
- Flat plates made of polypropylene have shown the worst thermal performance of all tested heat exchangers.
- Coil heat exchangers made of polypropylene for small ice storages were difficult to design and build. Therefore, it does not seem to be the a promising solution for low ice storage volume ($< 5 \text{ m}^3$).

3. Mathematical modelling of the ice storage

In this chapter, an ice storage model able to use capillary mats, coils and flat plate heat exchangers is described.

3.1. Literature review on ice storage models

Ice storage concepts can be classified as direct or indirect. In direct concepts, the heat exchanger is used to solidify water around the heat exchanger, while melting takes place by circulating warm water through the storage without any heat exchanger. Therefore, the ice is melted on the outside surface of the ice layer. Indirect concepts are those in which both solidification and melting is possible due the circulation of a brine solution in the heat exchanger. Since ice is melted on the surface of the heat exchanger indirect concepts are sometimes called internal melting concepts. The model presented in this paper, and thus the literature review described hereafter, is only focused on the indirect approach.

Phase change processes can be modeled at different levels of complexity, from empirical models to Computational Fluid Dynamics (CFD). In order to be able to assess the feasibility of an ice storage concept for solar heating applications yearly dynamic simulations are required. Therefore, complex models that need high computational time are not appropriate for this application. Many ice storage models have been developed until today. Most of the ice storage models can be classified into storage or heat exchanger based models. Storage models are focusing on the conservation of energy of the storage water, while heat exchanger based models are looking at the problem from the heat exchanger perspective. The second approach is usually profiting from the fact that water temperature in the storage remains close to $0 \text{ }^\circ\text{C}$ while ice exists and, thus, the storage model is simplified to an energetic balance in one control volume.

Jekel et al. (1993) developed a model based on the energy balance in the storage and heat transfer rate equations for heat exchanger predictions. The heat exchangers were modeled using a logarithmic mean temperature difference approach assuming a constant overall heat transfer coefficient from brine to bulk water along the heat exchanger length. Only one control volume was assumed for the water storage as well as for the heat exchanger. The solidification and melting was based on horizontal, spiral wound tubes spaced on a square grid. The process of extracting the sensible and latent heat from water was

split into sensible, unconstrained and constrained solidification and melting (see section 3.2.5 for further details). Averaged differences between simulations and manufacturers data were found to be up to 10% for the melting process. Because only manufacturers data was used, the validation of the model is lacking documented comparisons with experimental data. The main limitations of this model are that i) it is not valid for partial icing and melting and thus not able to predict correctly cycles of icing and melting; ii) only one control volume was assumed in both heat exchanger and storage iii) ice constraintment was considered assuming only symmetric cases and iv) the sensible heat in the ice was neglected (ice was assumed to be always at 0 °C).

Drees and Braun (1995) used the model developed by Jekel et al. (1993) and improved it by using discretization techniques in the the heat exchanger and by using more appropriate equations for forced convection inside a spiral tube geometry. Validation was provided with experiments with differences up to 6% for the energy exchanged in the melting period.

Vick et al. (1996) developed a model in which partial charge and discharge was considered by taking into account the possible existence of several and alternate layers of water and ice due to partial melting and icing. The creation of multiple layers made the model more complex. As a difference from the models cited above, two tubes were simulated to consider a counterflow arrangement. Moreover, the thermal capacity of ice, brine and tube walls was considered. As in the model of Drees and Braun (1995) the heat exchanger is discretized along the fluid flow path. The model was compared with experimental data in Nelson et al. (1996) with satisfactory results, but without quantifying differences between simulations and experiments. The main disadvantage of this model is that ice constraintment is not considered, which is a key aspect when high ice fractions are reached.

Neto and Krarti (1997a) presented a model where constrained ice growing was considered using a regular square geometry of tubes but considering different ice diameters on the tubes. The latter model was validated in Neto and Krarti (1997b) and the authors reported differences of 5% for energy exchanged at the end of the analyzed process. The model from Neto and Krarti (1997a) is the most detailed from the mentioned above. However, due to their consideration of the geometry of the coils in a detailed manner, the extension to other heat exchanger designs would be difficult. Moreover, the model is using an analytic solution for ice constraintment which is only valid for a symmetric case. As will be shown in section 4, the consideration of asymmetric cases is of relevance if capillary mats are to be modeled.

Koller et al. (2012) developed a model with similar features than those provided by Jekel et al. (1993), but natural convection around the tubes during the melting process of the water was considered. Comparisons with experimental results were provided with differences up to 10 % for the energy injected into the storage in the melting phase.

Most of the above mentioned models are focusing on the solidification and melting of ice around the heat exchangers and thus the modeling of the storage is highly simplified. Therefore, these models are valid if the temperature of the water remains close to 0 °C. For solar heating applications, the storage is used as cold source in winter and as heat sink in spring, summer and beginning of autumn. Thus, numerical models need to consider several control volumes along the height of the storage, considering the heat conduction between water layers, losses and gains from the ambient, and the density gradients of water that lead to stratification of the storage tank. Validations of the models for sensible heating and cooling of the storage water is also not usually reported in the literature. In the work presented by Carbonell et al. (2016c, 2015) those phenomena were considered. However, the ice storage concept in these publications was based on flat plate heat exchangers with thermal de-icing and therefore maximum ice thickness on the heat exchangers were low. Validation with different numbers of heat exchangers was not carried out in any of the cited articles. Thus, the model performance for other configurations than the reported ones, e.g. different heat exchanger spacing, is unknown.

The model presented in this paper considers ice constraintment for both symmetric and asymmetric cases, where different distances between pipes or heat exchangers can be defined along the width and the length of the storage. This feature is necessary if different numbers of heat exchanger units in the ice storage and thus different spacing between tubes shall be analyzed. Another important feature of this paper is that the number of experiments carried out is large, including two heat exchanger designs with different number of capillary mat units, four testing sequences (sensible heating, sensible cooling, solidification and melting) with two different volume flows (2000 l/h and 1000 l/h). The validation carried out is way more detailed, and therefore more challenging, compared to most of the publications found in the literature.

3.2. Mathematical formulation

The formulation of the ice storage model is based on the solution of the energy conservation law applied to the water of the storage Carbonell et al. (2015):

$$\rho c_p \frac{\partial T}{\partial t} + (\rho c_p)_{ice} \frac{\partial T_{ice}}{\partial t} = \frac{\partial}{\partial y} \left(\lambda \frac{\partial T}{\partial y} \right) + \frac{h_f}{V} \frac{\partial M_{ice}}{\partial t} + \dot{q}_{surr} + \dot{q}_{hx} \quad (13)$$

where c_p is the specific heat capacity of water, h_f the enthalpy of fusion, M_{ice} the mass of ice, \dot{q}_{ext} and \dot{q}_{hx} are the heat fluxes per unit volume between the storage fluid and the surroundings and heat exchanger respectively, T the water temperature, t the time, V the water volume of the storage, y the coordinate along the height of the storage, λ and ρ are the heat conductivity and density of water. The first and second term of Eq. 13 represents the accumulated sensible heat of the fluid and solid ice. The first term of the right side of Eq. 13 is the heat of conduction between control volumes and it is calculated using the conductivity of water at the specific temperature multiplied by the effective conductivity factor $\lambda_{eff} = \lambda_w(T) \cdot r_{eff}$. The latter is used in order to account for conduction in the walls of the storage. The second term of the right hand side of Eq. 13 represents the latent heat of solidification and melting and the last term two terms are the heat provided by the surroundings and heat exchangers respectively.

A drawback of this formulation is that the model is not able to handle a 100 % ice fraction in any control volume, since the energy balance is done in the liquid phase. When the water volume is extremely low, the stability of the model is penalised since any heat gains/losses means high temperatures changes in one time step.

3.2.1 Heat from/to the surroundings

The third term of the right side of Eq. 13 represents the heat losses to the surroundings through the external surface area of the storage tank A_{ext} . It is calculated assuming a constant heat transfer coefficient U_{ext} for each control volume j as:

$$\dot{Q}_{ext,j} = U_{ext,j} A_{ext,j} (T_j - T_{ext,j}) \quad (14)$$

where $\dot{Q}_{ext,j} = \dot{q}_{ext,j} V$ and T_{ext} is the temperature of the surroundings, which in the present case can be the ground or cellar temperature depending on the placement of the storage. The heat loss coefficient is provided as an input of the model for several surfaces, i.e. top, bottom and lateral sides. The latter is split into two values, one for the upper and one for the lower half of the lateral sides.

3.2.2 Heat exchangers

The heat exchanger is solved by a step-by-step model, which consists of a one-dimensional analysis in the fluid direction applying a finite control volume discretization technique. The energy balance inside the circulating fluid takes into an account the thermal losses through the external surface and convective heat transfer with the neighboring control volumes neglecting the axial heat conduction.

The discretized mesh is displaced (the node is at the fact of the CV) for \dot{m} , T and P , but is centered (the node is at the centre of the CV) for the storage water T_w and wall T_{wall} temperatures. Applying the mass conservation law in the whole domain, the mass flow rate at the outlet is directly obtained from the given mass flow rate at the inlet:

$$\dot{m}_{out} = \dot{m}_{in} \quad (15)$$

Under the above mentioned hypothesis, the energy conservation expression is discretized resulting in an algebraic equation in terms of temperature for a CV i of the form:

$$(\rho c_p V)_i \frac{\bar{T}_i - \bar{T}_i^0}{\Delta t} + \dot{m} c_{p,i} (T_{i+1} - T_i) = (UA)_i (T_{w,i} - \bar{T}_i) \quad (16)$$

The subscripts i and $i + 1$ represents the value at the inlet and outlet of the CV i respectively and the superscript 0 refers to the value at previous time step. The UA is the overall heat transfer rate coefficient

from the fluid to the bulk storage water T_w , \bar{T} represents the arithmetic average of the temperature between the temperatures at the faces of the CV i and $i+1$. The overall heat transfer coefficient is calculated as explained in section 3.2.3.

Algebraic equations resulting from the discretized energy and mass conservation laws shown above are solved from inlet to outlet following a step-by-step procedure (from CV i to the next CV $i+1$). The model needs no iterations if UA is known and the thermo-physical properties are calculated from conditions at the inlet of the CV. From the mass flow rate and temperature of the fluid at the inlet, and proper boundary conditions, the distribution of temperatures, mass flow rate (constant), and heat losses or gains throughout the physical domain are calculated.

3.2.3 Overall heat transfer coefficient

The main task in solving the heat exchanger is to calculate the overall heat transfer coefficient UA from Eq. 16. For situations where solidification/melting takes place, the UA reads:

$$UA = \frac{1}{\frac{1}{\alpha_{in}A_{in}} + \frac{1}{UA_{wall}} + \frac{1}{UA_{ice}} + \frac{1}{\alpha_{out}A_{out}}} \quad (17)$$

where the subscripts in , $wall$, ice , and out refer the internal fluid, wall, solidification and melting of ice and outside heat transfer coefficients. The α_{in} and α_{out} need to be defined for different boundary conditions and heat exchanger types. A summary of Equations used for those cases are shown in Table 3.1.

For tubes, the total heat transfer coefficient is obtained as:

$$UA = \frac{1}{\frac{1}{A_i\alpha_i} + \frac{\ln \frac{d_{p,out}}{d_{p,in}}}{2\pi L_{hx}\lambda_p} + \frac{\ln \frac{d_{ice}}{d_{p,out}}}{(2\pi - \phi_{cons})L_{hx}\lambda_{ice}} + \frac{1}{A_{ice}\alpha_o}} \quad (18)$$

where d_p is the pipe diameter, L_{hx} is the length of the pipe and ϕ_{cons} is the overlapping contact area between growing ice due to ice constraintment (see section 3.2.5 for more details). Therefore, the useful heat exchange area where ice and water are in contact is reduced by the overlapping as:

$$A_u = \left(\frac{2\pi - \phi_{cons}}{2} \right) d_{ice} L_{hx} \quad (19)$$

The heat transfer coefficient per useful area A_u is obtained from:

$$U = \frac{1}{\frac{(2\pi - \theta_{cons})}{2\pi} \left(\frac{d_{ice}}{d_{p,in}\alpha_{in}} + \frac{d_{ice}}{d_{p,out}\alpha_o} + \frac{d_{ice} \ln \frac{d_{p,out}}{d_{p,in}}}{2\lambda_p} \right) + \frac{d_{ice} \ln \frac{d_{ice}}{d_{p,out}}}{2\lambda_{ice}}} \quad (20)$$

All results presented in this report are based on a U value per external heat exchanger area as presented in Eq. 6. However, for the calculation of the model Eq. 20 is used.

3.2.4 Ice solidification and melting on the heat exchanger

The term for heat of solidification and melting appearing in Eq. 13 is defined as:

$$\dot{Q}_{lat} = h_f \frac{\partial M_{ice}}{\partial t} = h_f \rho_{ice} \frac{\partial V_{ice}}{\partial t} \quad (21)$$

Assuming a small time step, the latent heat due to ice growing on a cylinder tube surface can be linealized as:

$$\dot{Q}_{lat} = h_f \rho_{ice} \pi L \frac{(r_{ice})^2 - (r_{ice}^0)^2}{\Delta t} \approx h_f \rho_{ice} 2\pi L r_{ice}^0 \frac{r_{ice} - r_{ice}^0}{\Delta t} \quad (22)$$

where r_{ice}^0 is the radius of the previous time step. Rearranging Eq. 22, the radius for the new time step r_{ice} can be obtained:

$$r_{ice} = \frac{\dot{Q}_{lat} \Delta t}{h_f \rho_{ice} 2\pi L r_{ice}^0} + r_{ice}^0 \quad (23)$$

Table 3.1: Internal and external heat transfer coefficients for all considered cases and heat exchanger types. Nu , Re , Pr and Ra are the Nusselt, Reynolds, Prandtl and Raleigh numbers, D_h is the hydraulic diameter, f the friction factor, C and n are constants, L_{char} the characteristic length, H_{hx} the height of the flat plates

Brine fluid to heat exchanger wall		
	<i>Corrugated flat plates</i>	
Cooper and Usher (2002)	$Nu_L = 1.68 \left(\frac{Re Pr D_h}{w} \right)^{0.4}$ $Nu_T = 0.2 (Re^{0.67} Pr^{0.4})$	$Re \leq 70$ changed from Ref. $Re \geq 150$ changed from Ref. $70 < Re < 150$ Transition
	<i>Straight tubes</i>	
Gnielinski from Incropera et al. (2006)	$Nu_L = 4.36$ $Nu_T = \frac{f}{8} \frac{(Re-1000)Pr}{1+(12.7(f/8)^{0.5}(Pr^{2/3}-1)}$	$Re < 2300$ $Re < 2e^4$ $f = 0.316 Re^{-0.25}$ $Re \geq 2e^4$ $f = 0.184 Re^{-0.2}$
Heat exchanger to bulk water (without ice)		
	<i>Flat plates and pipes</i>	
Morgan (1975) (developed for pipes)	$Nu = CRa^n$	flat plates $L_{char} = H_{hx}$ pipes $L_{char} = d_{p,out}$ or H_{hx}
	<i>Flat plates</i>	
Churchill (2002) (for immersed plates)	$Nu_L = 0.68 + 0.67(Ra \cdot f(Pr))^{1/4}$ $Nu_T = 0.15(Ra \cdot f(Pr))^{1/3}$ <p>where $f(Pr) = (1 + (0.492/Pr)^{9/16})^{-16/9}$</p>	$Ra \leq 1e^9$ $Ra \geq 1e^{12}$
	<i>Tubes</i>	
Churchill and Chu from Incropera et al. (2006)	$Nu = \left(0.6 + \frac{0.387 Ra^{1/6}}{(1 + (0.559/Pr)^{9/16})^{8/27}} \right)^2$	
Ice to water		
	<i>Solidification</i>	
Churchill and Chu from Stephan (2006)	$Nu = \left(0.825 + 0.387 [Gr \cdot Pr \cdot f(Pr)]^{1/6} \right)^2 + 0.435 \frac{L_{char}}{2r_E}$	$L_{char} = L_{tube}$
	<i>Gap between melted water and ice</i>	
Koller et al. (2012)	$Nu_{gap} = 0.3 Ra^{0.238}$	$Nu_{gap} > 1$ $\lambda_w = \lambda_w \cdot Nu_{gap}$

Similarly, in case of flat plate heat exchangers, the new ice thickness can be calculated:

$$s_{ice} = \frac{\dot{Q}_{lat} \Delta t}{h_f \rho_{ice} 2\pi L} + s_{ice}^0 \quad (24)$$

Ice can be formed and melted in different configurations if partial icing is considered. Some examples are shown in Fig. 3.1 where ice is colored blue and the formed/melted ice in one time step as dashed red zone. In Fig. 3.1(a), ice forms (dashed red) at the exterior of a block of ice (in blue). If after the icing, a melting process follows, then ice is melted from inside (white zone). The melted ice in one time step is shown in dashed red. Let's now imagine that before all ice is melted, a new sequence of icing starts. Under these assumptions, as shown in Fig. 3.1(c), a second ice layer will be present. In principle, this partial icing and melting phenomena may exist in many steps. In the proposed model this process is simplified assuming that only two concentric layers of ice may exist. If a third layer is created, then the layer of ice surrounded by water, inside the outer ice layer, is assumed to attach to the inside of the outer ice layer. This simplification is used both for tubes and flat plates.

A summary of each of the heat transfer coefficients can be found in Table 3.2. From the expressions

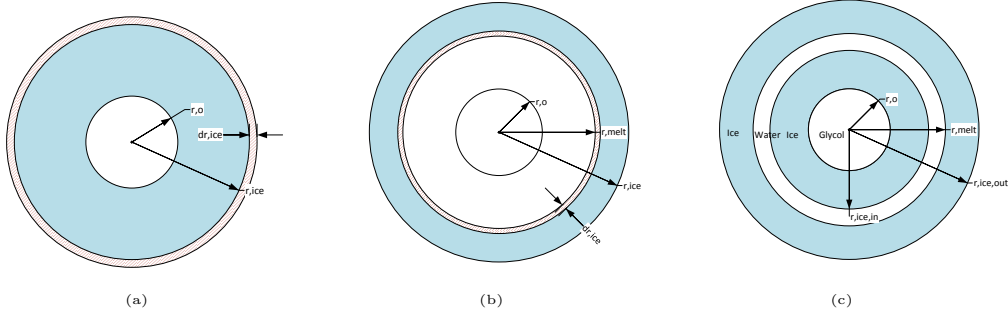


Figure 3.1: (a) Ice growing on a cylinder and (b) ice internal melting (c) partial icing and melting.

shown in this Table, the UA value for flat plates can also be derived.

Table 3.2: Equations for flat plates and cylinder heat exchangers.

Equation	Flat plate	Cylinder
α_i, α_o	see Table 3.1	Table 3.1
UA_{wall}	$A_{hx} \frac{\lambda_{wall}}{\delta_{wall}}$	$\frac{2\pi L \lambda_{wall}}{\ln(d_{out}/d_{in})}$
UA_{ice}	$A_{hx} \frac{\lambda_{ice}}{s_{ice}}$	$\frac{2\pi L \lambda_{ice} f_{cons}}{\ln(d_{ice}/d_{out})}$

3.2.5 Constrained calculation

When ice grows on a circular tube and the radius of icing is larger than half the distance to the next tube, the two ice surfaces are in contact, which leads to a decreased surface of the ice-to-water contact area and thus to a decreased heat transfer capacity. In a first approximation, it is useful to treat the problem purely geometrically. The total area of constrained surface A_{cons} , where the heat transfer is negligible because of symmetry, can be described by the overlapping angle of the cylinder ϕ_{cons} and the icing radius:

$$A_{cons} = r_{ice} \cdot \phi_{cons} \cdot L_{tubes} \quad (25)$$

where L_{tubes} is the length of the tube. Assuming a symmetric case, where all tubes are parallel (same flow) and equally distant from each other, the center of the tubes form a quadratic grid. The solution for the overlapping angle in this case was proposed by Neto and Krarti (1997b):

$$\phi_{cons} = 8 \cdot n_{tube,tot} \cdot \cos^{-1} \left[\frac{x}{r_{ice}} \right] \quad (26)$$

where x is half the distance between tubes. The present model needs to consider a grid with different distances in the two axis. Therefore, the longer and the smaller grid distances are considered, namely x_{large} and x_{small} respectively. Figure 3.2 shows the considered grid where x_{large} represents half the distance between tubes in the x-axis and x_{small} represents half the distance between tubes in the y-axis. The critical radius of the ice cylinder where the surface area is constrained is $r_{ice} > x_{large}$ and $r_{ice} > x_{small}$ respectively. When neglecting the outermost tubes that are not surrounded by four neighboring tubes, the angle related to the total surface can be calculated as:

$$\phi_{cons} = 2 \cdot \phi_{small} + 2 \cdot \phi_{large} = 4 \cdot n_{tube,x} \cdot \cos^{-1} \left[\frac{x_{large}}{r_{ice}} \right] + 4 \cdot n_{tube,y} \cdot \cos^{-1} \left[\frac{x_{small}}{r_{ice}} \right] \quad (27)$$

where $n_{tube,x}$ and $n_{tube,y}$ are the number of tubes in the two directions of the grid. Notice that Eq. 26 is a particular case of Eq. 27 where $x_{small} = x_{large} = x$.

The total active area can then be calculated from the total area as:

$$A_{active} = 2\pi r_{ice} \cdot n_{tube,x} \cdot n_{tube,y} - \phi_{cons} \cdot r_{ice} = A_{uncons} \left(1 - \frac{\phi_{cons}}{2\pi} \right) \quad (28)$$

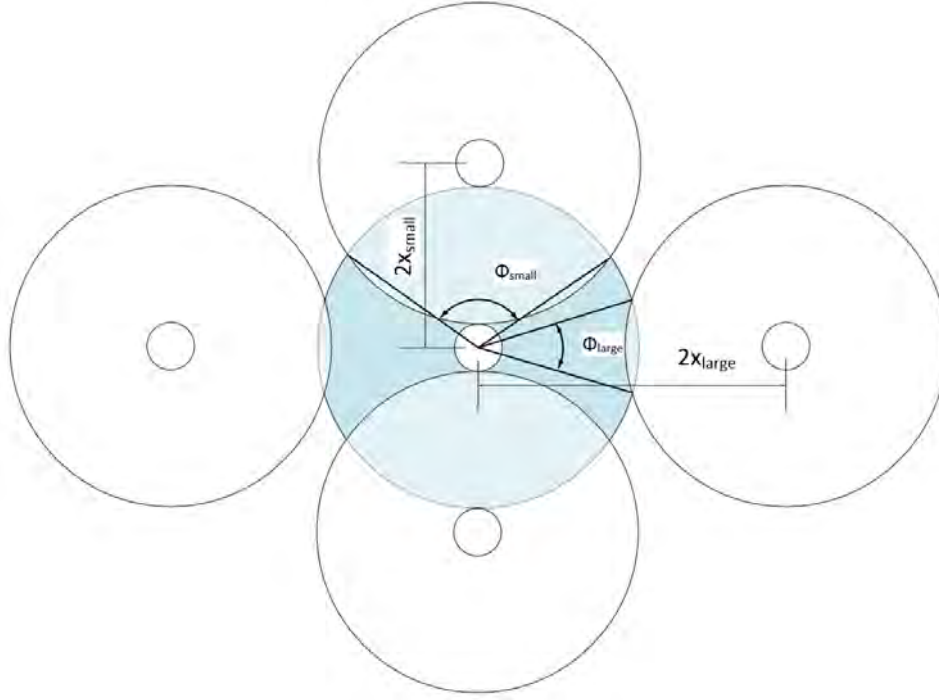


Figure 3.2: Schematic drawing of the geometry used in the constraint ice calculation.

From this equation a surface correction factor Ar can be defined as:

$$Ar = \left(1 - \frac{\phi_{cons}}{2\pi}\right) = 1 - \left(\frac{2\cos^{-1}\left(\frac{x_{large}}{r_{ice}}\right)}{\pi}\right) - \left(\frac{2\cos^{-1}\left(\frac{x_{small}}{r_{ice}}\right)}{\pi}\right) \quad (29)$$

A model based on Eq. 27 assumes that the heat flux exchanged when ice growing is constrained is proportional to the surface area between ice and water. However, since the temperature gradient and the heat flux will not be radial in the constraint case the conductance is not proportional to the active surface. Based on the ideas above, a correction factor of the conductance can be defined based on the surface correction factor Ar as:

$$f_{cons}(Ar) = \frac{\dot{Q}_{con}}{\dot{Q}_{unc}} \quad (30)$$

where \dot{Q}_{unc} is the ideal (unconstrained) heat flux through a cylindrical annulus with inner radius r_{pipe} and outer radius r_{ice} and \dot{Q}_{cons} is the real (constrained) heat flux. The factors f_{cons} and Ar were originally defined in Jekel et al. (1993) and correlated under the assumption that the ice cylinder is connected at four alternate equidistant points along the surface perimeter. In that symmetric case, the surface correction factor reduces to:

$$Ar = 1 - \left(\frac{4\cos^{-1}\left(\frac{x}{r_{ice}}\right)}{\pi}\right) \quad (31)$$

where x is the distance between equidistant tubes. In Jekel et al. (1993), a correction function was fitted to heat flux values that were calculated using a finite element calculation.

$$f_{jekel} = -1.441 \cdot Ar + 2.455\sqrt{Ar} + \left(3.116 \cdot Ar - 3.158\sqrt{Ar}\right) \frac{r_{ice,ideal}}{x_{small}} \quad (32)$$

The correction factor can also be obtained from the constrained angle from Eq. 27 considering only the geometry as:

$$f_{\phi_{cons}} = 1 - \frac{\phi_{cons}}{2\pi} \quad (33)$$

Notice that this correction factor is exactly equal to the argument Ar defined in Eq. 29 which is used to calculate f_{jekel} . Therefore, the use of the correction factor f_{jekel} , can be considered as an extension of the geometrical factor.

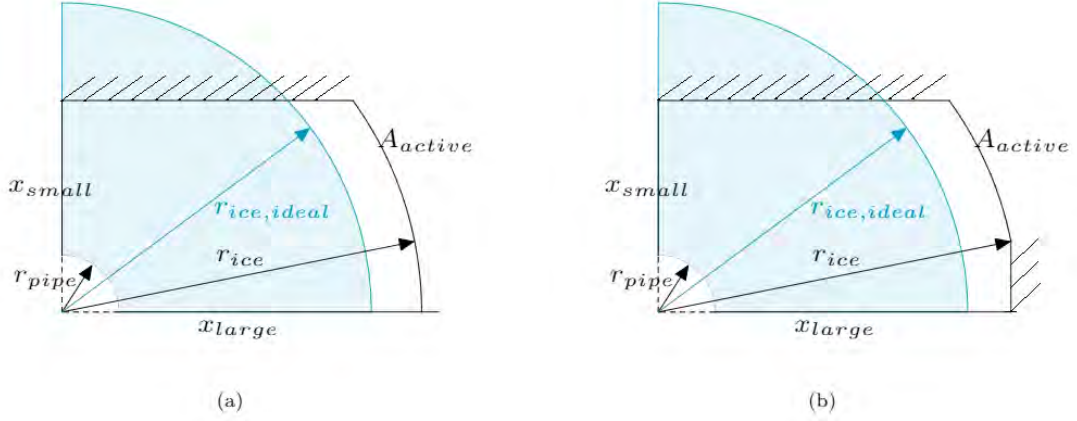


Figure 3.3: Geometry where ice is constrained in (a) the x_{small} axis and (b) in both axis. The $r_{ice,ideal}$ is defined as the unconstrained radius that leads to the same area (blue zone) as the constrained area

The method proposed by Jekel et al. (1993) has been further extended in the present project in order to consider different distances between tubes in the x and y direction of a rectangular grid. A modified correction factor f_{cons} was derived using the FEM solver of ANSYS CFX. A 2D model of a constrained ice piece was built in the shape of the constrained ice geometry shown in Fig. 3.3. The figure on the left hand side shows the case in which constraint only happens in the direction of x_{small} . The right figure shows the case in which the icing surface is constrained in all directions. All surfaces except A_{active} and the pipe surface are adiabatic due to the symmetry of the heat exchanger arrays. The heat flux values were calculated in ANSYS keeping the pipe surface at -4 °C and the active outer surface at 0 °C. The resulting correction factor of the heat flux through the surface $f(Ar, \alpha, \beta)$ is related to the ratios:

$$\alpha = \frac{x_{small}}{\min(r_{ice}, x_{large})}, \quad \alpha \in (\beta, 1] \quad (34a)$$

$$\beta = \frac{r_{pipe}}{\min(r_{ice}, x_{large})}, \quad \beta \in (0, 1) \quad (34b)$$

The function $f(Ar, \alpha, \beta)$ was evaluated on a grid of total 1100 points. The grid contains values of α in the range of $0.16 < \alpha < 1$ and values of β range of $0.064 < \beta < 0.25$. In order to implement the correction factor function $f(Ar, \alpha, \beta)$ into the simulation model, a fitting function was derived:

$$f_{cons}(Ar, \alpha, \beta) = Ar^{w_1} Ar^2 + w_2 \beta^2 + w_3 \alpha^2 + w_4 Ar \beta + w_5 Ar \alpha + w_6 \beta \alpha + w_7 Ar + w_8 \beta + w_9 \alpha + w_{10} \quad (35)$$

The function used fulfills the requirements $f_{cons}(0, \alpha, \beta) = 0$ and $f_{cons}(1, \alpha, \beta) = 1$ for all α and β . The free parameters of the function have been fitted to the FEM-results using a least squares algorithm. The resulting values of the fitting are given in Table 3.3. The fitting function resulted in an absolute RMS error of 0.018 at the evaluated points.

The used model always assumes that ice grows ideally as a perfect cylinder. The area using the the ideal radius $r_{ice,ideal}$ and the real r_{ice} differ depending on the amount of overlapping area. Starting from the total ice area it is straight forward to calculate the radius $r_{ice,ideal}$ of circular tubes around the heat exchanger (filled area in Figure 3.3) that leads to the same area (same ice volume when considering the length). However, for the fitting function, the radius of the assumed constrained ice surface r_{ice} is necessary. There is no analytic solution to the geometric equation that relates $r_{ice,ideal}$ and r_{ice} . Therefore, another fitting function $g(\gamma, \alpha, \beta)$ is used such that the following equation holds:

$$r_{ice} = g(\gamma, \alpha, \beta) \cdot r_{ice,ideal} \quad (36)$$

The used fitting function is again a quadratic function in three variables:

$$g(\gamma, \alpha_g, \beta_g) = v_1 \gamma^2 + v_2 \alpha_g^2 + v_3 \beta_g^2 + v_4 \gamma \alpha_g + v_5 \gamma \beta_g + v_6 \alpha_g \beta_g + v_7 \gamma + v_8 \alpha_g + v_9 \beta_g + v_{10} \quad (37)$$

Where the coefficient γ is defined as:

$$\gamma = \frac{r_{ice,ideal}}{r_{small}} \quad (38)$$

In Eq. 37, a modified version of α and β , namely α_g and β_g , are used:

$$\alpha_g = \frac{x_{small}}{x_{large}} \quad (39a)$$

$$\beta_g = \frac{r_{pipe}}{x_{large}} \quad (39b)$$

The above equations are not exactly the same as the ones defined in Eq. 34a and Eq. 34b because the real r_{ice} is not known beforehand. Therefore, it is not possible to know if the ice will be constrained in the x_{large} axis.

All the above definitions ensure that the following applies:

$$0 \leq r_{ice} < x_{small} \rightarrow \bar{A}r = 1, \alpha = 1, \beta = 1 \rightarrow f_{cons}(1, 1, 1) = 1 \quad (40)$$

Table 3.3: Best fit values of the generalized correction function $\bar{f}(\bar{A}r, \alpha, \beta)$

Coefficient	Fitting value	Coefficient	Fitting value
w_1	0.18142704	v_1	-0.24882159
w_2	0.12806988	v_2	3.21603436
w_3	0.59817959	v_3	-0.36384021
w_4	0.38678919	v_4	1.98830385
w_5	-1.63787425	v_5	0.38896584
w_6	-0.47262632	v_6	0.53800171
w_7	1.43174888	v_7	2.14297332
w_8	0.79350135	v_8	-3.20396299
w_9	-0.80224704	v_9	1.41740863
w_{10}	0.41533001	v_{10}	-2.38774657

The function was fitted to the calculated values that have been extracted from the ANSYS model. The best fit parameters are shown in Table 3.3. The absolute RMS of the fit function of $g(\gamma, \alpha_g, \beta_g)$ is 0.025. For a given heat exchanger geometry the correction value can be approximated in the following way:

$$r_{ice} = \max(1, g(\gamma, \alpha, \beta)) \cdot r_{ice,ideal} \quad (41)$$

The \max function introduces a lower bound to the fitting function $g(\gamma, \alpha, \beta)$ which improves the result. Values below 1 are nonphysical due to $r_{ice} > r_{ice,ideal}$. However, they can result as an artifact of fitting inaccuracy.

3.2.6 Comparison between ice constraint models

A comparison between the results of the different constraint methods explained in section 3.2.5 is shown in Fig. 3.4. The graphs show the correction factor f according to the methods described in Eq. 32 and Eq. 33 and in the present work (f_{cons}). In order to apply Eq. 32 on a non-symmetric case, the average distance between x_{small} and x_{large} is used as x .

When r_{ice}/x_{small} reaches 1 then the ice is constrained in the x_{small} axis. In the second y-axis the ratio r_{ice}/x_{large} is presented. When r_{ice}/x_{large} reached 1, then ice is constrained in both directions. This phenomena can only be considered by the present model f_{cons} , the others can not deal with constraint in two directions. As can be observed in Fig. 3.4, there are large differences between the methods, which are mainly due to different range of validity and different definitions of r_{ice} . The larger the asymmetry between tubes, the steeper the decrease of f_{cons} , and thus power, when the ice is constrained in two axis. The most asymmetric case is Stype-8hx, where the distance between tubes in the heat exchanger is 20 mm and the distance between tubes of different heat exchangers is 120 mm. For this case, when r_{ice}/x_{large} is equal to 1 the f_{cons} decay to zero rapidly, while in the Gtype-16hx (the symmetric case) the decay is slower. The correction function f_{jessel} is only valid for the symmetric case Gtype-16Hx. Both

f_{const} and f_{jekel} take into account the difference between $r_{ice,ideal}$ and r_{ice} and therefore decay to zero at the same value in the symmetric case. The geometric function $f_{\phi_{cons}}$ can be used for the rectangular grid as well but it is completely based on $r_{ice,ideal}$. Thus, the correction factor has non-negative values for large radius r_{ice} where in reality everything would be fully iced.

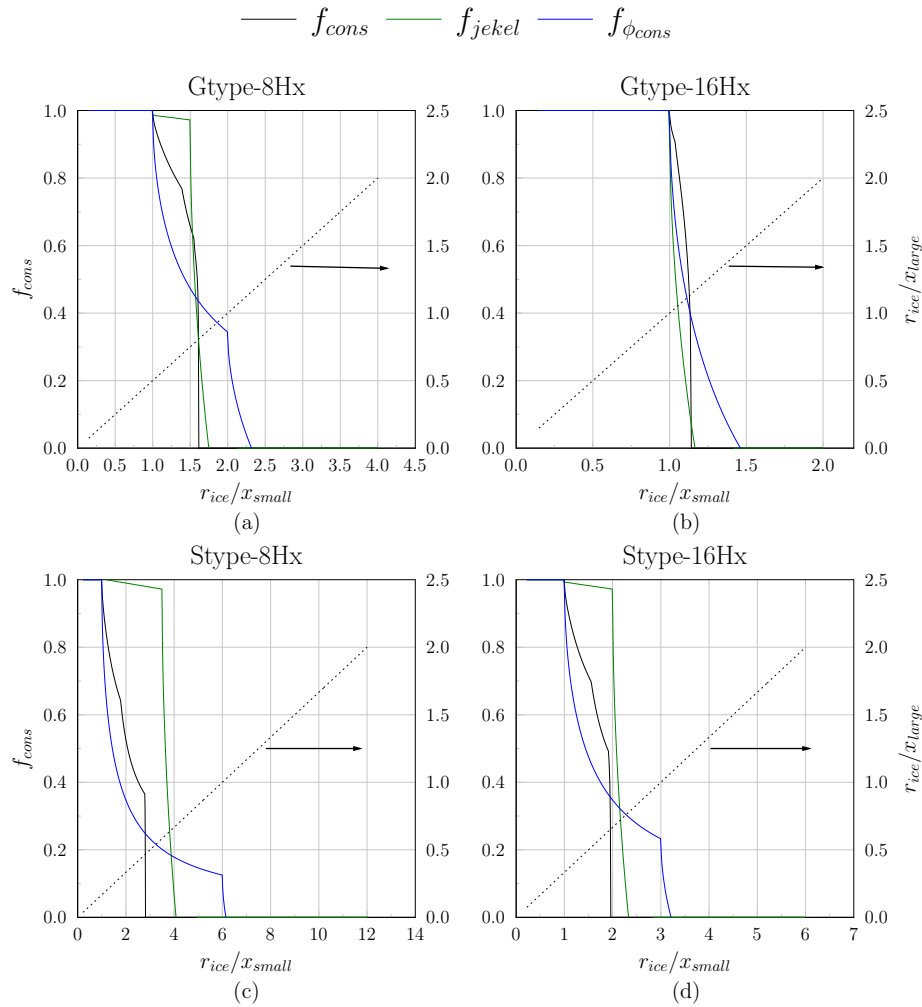


Figure 3.4: Comparison of the different correction functions f_{cons} for the particular cases of the four capillary mats experimentally evaluated in the project.

3.3. Conclusions

The mathematical formulation of an ice storage able to consider several heat exchanger types, i.e. coils, capillary mats and flat plates has been presented. The main novelty of the developed model is that it is able to simulate the solidification of ice for asymmetric tube configurations, where the distance between tubes in one heat exchanger is very different from the distance between tubes of neighboring heat exchangers. This ice constraint feature is necessary to evaluate the performance of the storage with varying number of capillary mats and coils and with different heat exchanger designs, where distances between tubes are different.

4. Validation of the ice storage model

The model described in chapter 3 has been implemented in TRNSYS using FORTRAN 90 language. The development has been implemented in a separate ice storage model Type 861 based on Type 860

developed in Carbonell et al. (2015). The experiments presented in chapter 2 are used for the validation process. From all the experimentally analyzed heat exchangers, the capillary mats S-type and G-type and the flat plates of stainless steel (FP-SS) will be used for the validation process. Flat plates made of polypropylene will not be modelled since they did not show promising results in chapter 2. Results of coil heat exchangers will not be used here since this heat exchanger concept, as built in chapter 2, does not fit very well for small ice storages.

The validation process includes all sequences tested as described in Table 2.3 for the two volume flow rates of 2000 l/h and 1000 l/h. The results of the validation are shown separately per heat exchanger type, i.e. flat plates and capillary mats.

In this chapter markers are used for experimental data and solid lines for simulations. All experimental results can be presented with their respective error band. However, this hampers the visualization and does not bring much information for most of the compared variables because the error band is quite low. The only case where the uncertainty is large and therefore shown is the analysis of the heat transfer rate UA. The UA is preferred in this chapter instead of the U value used in chapter 2 because the UA obviously changes when the number of heat exchangers is increased. Instead, all U values tend to be very close to each other when plotted in the same graph and it is difficult to see the difference between simulations and experiments.

An important aspect to take into account for the validation process is related to the parameters used in the model. Usually, some parameters can be tuned so that predictions match better to the experiments when for example, heat exchanger design, area or volume flow is modified. However, in most of practical cases where the ice storage model will be used, there is no experimental data to fit the model and therefore the model needs to rely on standard values. The strategy followed for the validation process is to define those parameters that can be fitted using common values from literature or derived in this project and use them for all simulations. Another important factor for the model validation is that the number of experiments carried out is very large, i.e. several heat exchanger designs with several number of units, several testing sequences with two different volume flows are used. The validation carried out is way more detailed, and therefore more challenging, compared to most of the publications found in the literature.

Contents of this chapter have been submitted to a peer-reviewed journal as Carbonell et al. (2017)

4.1. Quantified differences between experiments and simulations

In order to have a quantified measure of the differences between simulations and experiments, the root mean square error along the test sequence will be used:

$$\theta_{rms} = \sqrt{\frac{\sum_{i=1}^n (\theta_{exp} - \theta_{num})^2}{n}} \quad (42)$$

where θ_{rms} is the variable of interest, n the number of experimental data, and exp and num refer to experimental and numerical predictions respectively. Besides the root mean square value, its normalized form, expressed as a percentage, will also be used for some of the variables:

$$\theta_{N_r,rms} = 100 \cdot \frac{\theta_{rms}}{\sum_{i=1}^n \frac{\theta_{exp}}{n}} [\%] \quad (43)$$

The normalized form will not be used for temperatures because in the solidification process the temperature is very close to 0 °C. Each testing sequence was experimentally evaluated for different number of heat exchangers and the model is validated for all cases. Therefore, for each testing sequence there will be different simulations and in order to report one single value regarding the accuracy of the model the maximum difference over several simulations will be denoted as θ_{rms}^{max} ; and the averaged value as θ_{rms}^{avg} . The same nomenclature will be used for the normalized values, i.e. $\theta_{N_r,rms}^{max}$, $\theta_{N_r,rms}^{avg}$. All these quantified differences are shown in the Tables of the following sections.

4.2. Sensible heating cycle

The experiments for the sensible heating cycle have been presented in section 2.6.1. The cycles consist on heating the storage by circulating a warmer brine through the heat exchangers until the temperature at

the outlet of the heat exchanger stabilizes at a defined value. Two volume flows are used: i) when 2000 l/h are used the storage temperature is heated from 20 °C to 40 °C, and ii) when 1000 l/h are used, the storage is heated from 10 °C to 20 °C.

The brine from the heat exchanger is heated directly by a chiller heater without any storage in between. Therefore, the inlet temperature in the heat exchangers evolves during time. The volume flow rate and also the inlet temperature of the heat exchangers are used as inputs for the model. The same is true for all the remaining testing sequences presented in the following sections.

This section is divided in two parts, the first one is focused on flat plates and the second one in capillary mats.

4.2.1 Flat plates

Experimental and numerical results for the sensible heating test are provided in Fig. 4.1 and Fig. 4.2 for (left) 2000 l/h and (right) 1000 l/h for all FP tested. Quantified RMS differences are provided in Table 4.1.

Table 4.1: RMS differences between experiments and simulations for sensible heating tests using flat plates.

	$T_{out,rms}$ [K]	T_w,rms [K]	\dot{Q}_{rms} [kW]	$\dot{Q}_{Nr,rms}$ [%]	Q_{rms} [kWh]	$Q_{Nr,rms}$ [%]
Sensible heating from 20°C to 40°C with 2000 l/h						
FP-SS-10hx	0.17	0.10	0.45	8.37	2.50	8.07
FP-SS-8hx	0.15	0.22	0.40	7.52	1.74	5.86
FP-SS-6hx	0.13	0.22	0.32	5.68	1.06	3.81
θ_{max}	0.17	0.22	0.45	8.37	2.50	8.07
θ_{avg}	0.15	0.18	0.39	7.19	1.77	5.91
Sensible heating from 10°C to 20°C with 1000 l/h						
FP-SS-10hx	0.18	0.08	0.12	3.79	0.24	1.50
FP-SS-8hx	0.22	0.08	0.14	4.39	0.45	2.82
FP-SS-6hx	0.19	0.11	0.15	4.43	0.25	1.52
θ_{max}	0.22	0.11	0.15	4.43	0.45	2.82
θ_{avg}	0.20	0.09	0.14	4.20	0.31	1.95

The outlet temperature of the heat exchanger is shown in the upper graphs of Fig. 4.1. With both mass flow rates the numerical results agree very well with experimental data. A maximum RMS error of $T_{f,out,rms}$ of 0.22 K in all of the six simulated cases can be observed. This correspond to 0.5 % of the maximum temperature of the test. The averaged temperature in the storage (not shown in the Figures) is also very well predicted with a maximum $T_{w,rms}$ of 0.22 K in all of the six simulated cases.

The power provided by the heat exchangers to the storage is shown in the mid part of Fig 4.1. Results agree very well with the experimental data with 1000 l/h. However, some differences are observed at the end of the test for 2000 l/h with an averaged \dot{Q}_{rms}^{avg} error for the three FP simulations of 7 %. Smaller differences of 4 % are achieved for 1000 l/h. The higher differences for 2000 l/h have an effect on the cumulative energy predicted. The averaged Q_{rms}^{avg} error for the three FP simulations is of 6 % for 2000 l/h and of 2 % for 1000 l/h.

The heat transfer coefficient rate is shown in Fig 4.2. The UA value considers many phenomena and therefore it is very difficult to predict it accurately. Uncertainties at the end of the test are much higher due to the lower temperature difference between the inlet and the outlet of the heat exchanger, as well as between the outlet and the storage temperatures. Simulations with 2000 l/h show good agreement and most of the results are within or close to the uncertainty range. However, predictions show less influence on the number of heat exchangers from 8 to 10 units, i.e. the clear variation of UA observed in experiments is not seen in the model calculations.

4.2.2 Capillary mats

Simulated and experimental results for a sensible heating test are shown on Fig. 4.3 and Fig. 4.4 for both 2000 l/h (left) and 1000 l/h (right). Quantified differences between simulations and experiments

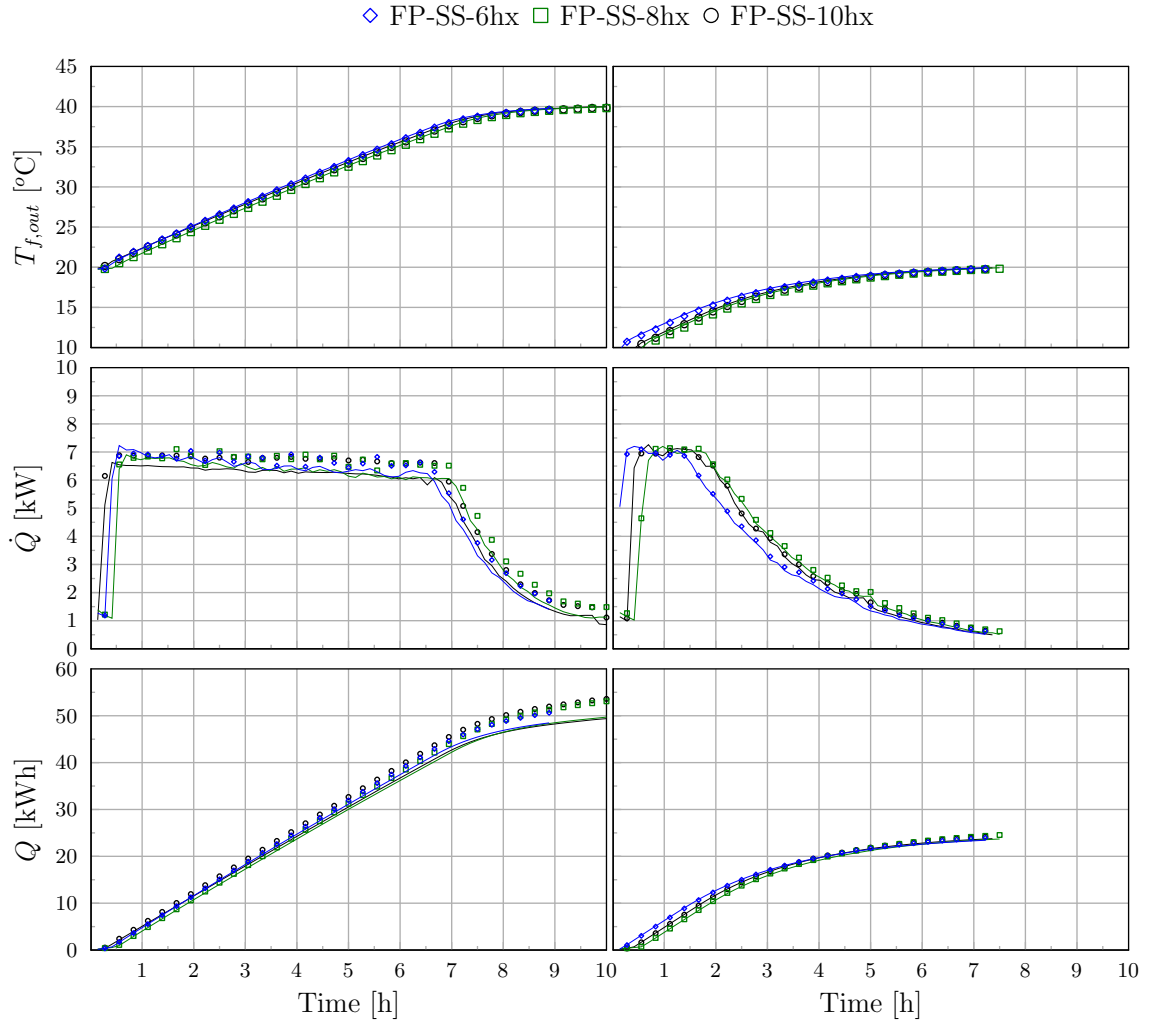


Figure 4.1: Simulation (solid lines) and experimental (symbols) results for the sensible heating test with (left) 2000 l/h and (right) 1000 l/h.

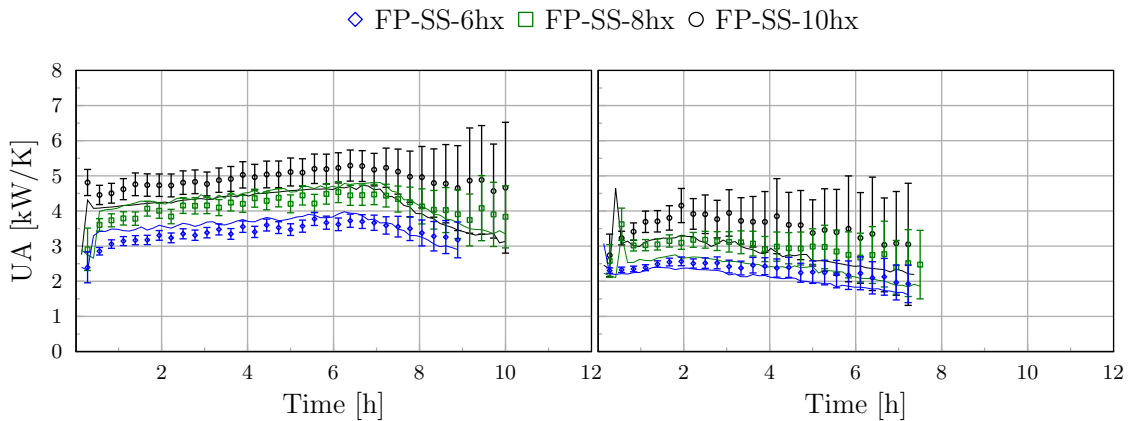


Figure 4.2: Heat transfer rate of FP for the sensible heating test with (left) 2000 l/h and (right) 1000 l/h. Simulation (solid lines) and experimental (symbols)

are provided in Table 4.2.

Table 4.2: RMS differences between experiments and simulations for sensible heating test using capillary mats.

	$T_{out,rms}$ [K]	T_w,rms [K]	\dot{Q}_{rms} [kW]	$\dot{Q}_{Nr,rms}$ [%]	Q_{rms} [kWh]	$Q_{Nr,rms}$ [%]
Sensible heating from 20°C to 40°C with 2000 l/h						
CM-Gtype-16hx	0.19	0.45	0.35	7.17	0.89	2.92
CM-Stype-16hx	0.07	0.36	0.11	3.21	0.30	1.13
CM-Gtype-8hx	0.08	0.44	0.15	4.27	0.46	1.62
CM-Stype-8hx	0.13	0.55	0.24	6.92	0.66	2.31
θ_{max}	0.19	0.55	0.35	7.17	0.89	2.92
θ_{avg}	0.12	0.45	0.21	5.39	0.58	1.99
Sensible heating from 10°C to 20°C with 1000 l/h						
CM-Gtype-16hx	0.23	0.37	0.31	12.44	0.45	4.16
CM-Stype-16hx	0.30	0.61	0.35	15.84	0.49	4.60
CM-Gtype-8hx	0.37	0.87	0.32	11.68	0.82	5.49
CM-Stype-8hx	0.28	0.69	0.33	13.72	0.84	5.55
θ_{max}	0.37	0.87	0.35	15.84	0.84	5.55
θ_{avg}	0.30	0.64	0.33	13.42	0.65	4.95

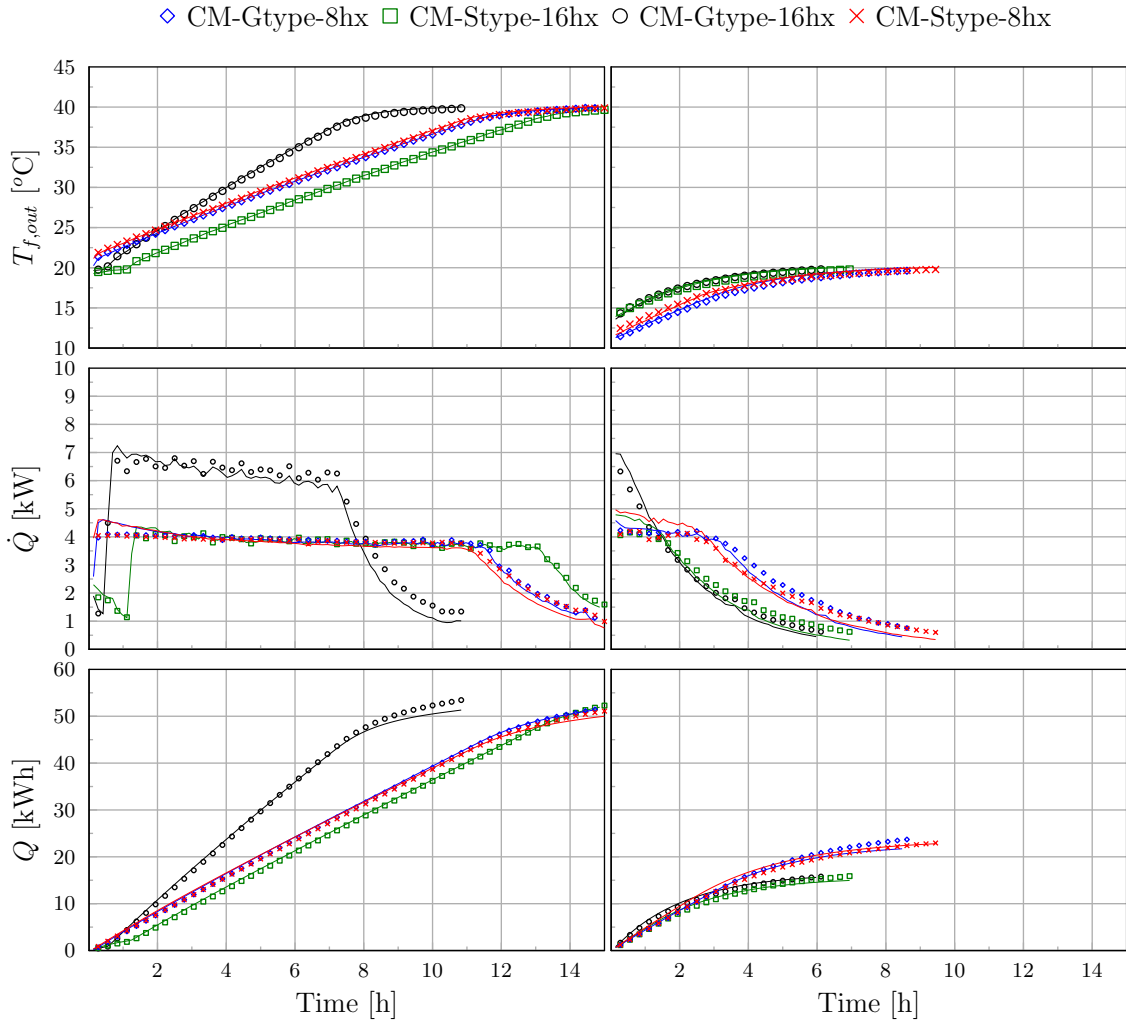


Figure 4.3: Simulation and experimental results of CM for the sensible heating test with (left) 2000 l/h and (right) 1000 l/h.

The outlet temperature of the heat exchanger is shown in the upper part of Fig. 4.3 with very good results

for both volume flow rates. Averaged heat exchanger outlet temperature RMS differences between all heat exchangers analysed presented in Table 4.2 are 0.1 K and 0.3 K for 2000 l/h and 1000 l/h respectively. These RMS temperature differences are 0.2 % and 1.5 % respect the maximum temperature of the test.

The averaged temperature in the storage (not shown in the Figures) is also well predicted with a maximum RMS difference of 0.4 K for 2000 l/h and 0.9 K in 1000 l/h. These differences represent 1 % and 4 % for 2000 l/h and 1000 l/h respect to the maximum temperature of the test.

The power exchanged by the heat exchangers is shown in the middle part of Fig. 4.3. Results agree relatively well for 2000 l/h with averaged power $N_{r,rms}$ differences of 5 %. Maximum differences of 7 % are observed for 2000 l/h, which are mainly due to under-predictions of power at then end of the test sequence, when the difference between the temperature in the heat exchanger and storage is relatively low. Results for 1000 l/h are significantly worst for all simulated cases. None of the simulated cases using 1000 l/h is able to predict correctly the beginning of the test sequence and this affects the storage temperature, which is over-predicted during the first hour, affecting the rest of the simulated time. Averaged errors in power exchanged in the range of 13 % are observed which are well above the 5 % observed for 2000 l/h. The reason for this difference is that the test sequence was not started from a steady state and therefore the dynamics of the storage and heat exchangers influence the first part of the test sequence. These dynamics of the starting period were not considered in the model and the accuracy of the whole test sequence is penalized.

The cumulative energy provided to the storage is shown in the lower part of Fig. 4.3. In terms of energy provided results are satisfactory with averaged RMS values of 2 % and 5 % for 2000 l/h and 1000 l/h respectively.

The UA values are shown in Fig. 4.4. All simulations tend to over-predict the experimental values. However, the higher values for increased number of heat exchangers seem to be well predicted since distance between lines in simulations and between marks in experiments match quite well.

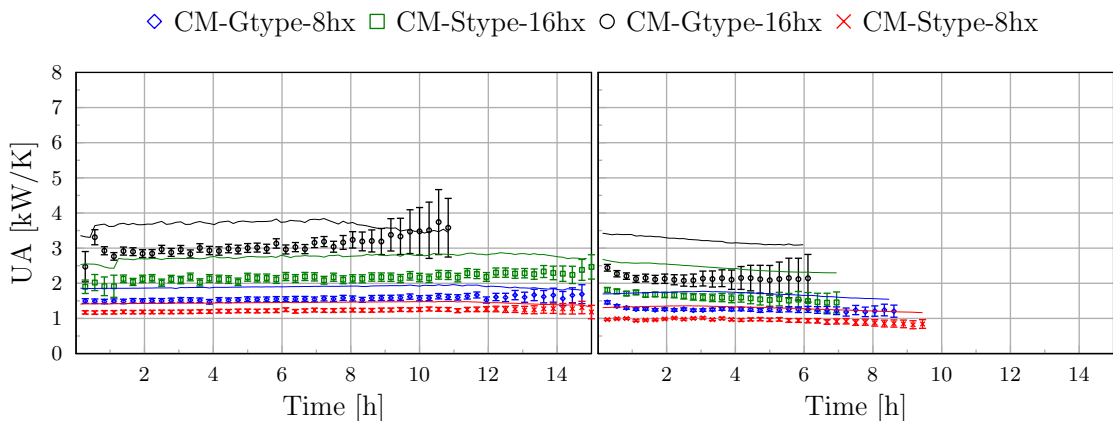


Figure 4.4: Heat transfer rate of CM for the sensible heating test with (left) 2000 l/h and (right) 1000 l/h. Simulation (solid lines) and experimental (symbols).

4.3. Cooling cycle

The experiments for the sensible cooling cycle have been presented in section 2.6.2. The cycles consist of cooling the storage from a starting temperature of 40 °C (2000 l/h) or 20 °C (1000 l/h) by circulating a colder brine through the heat exchangers until the temperature at the outlet of the heat exchanger reaches values close to 0 °C. This test sequence had no real stop in the experiments, the test was continued until the storage was fully iced (see section 4.4). However, in order to present results it is more convenient to split the test into sensible cooling and icing.

4.3.1 Flat plates

Experimental and numerical results for the sensible cooling test are provided in Fig. 4.5 and Fig. 4.6 for (left) 2000 l/h and (right) 1000 l/h for all FP tested. Quantified differences between simulations and experiments are provided in Table 4.3.

Table 4.3: RMS differences between experiments and simulations for sensible cooling tests using flat plates.

	$T_{out,rms}$ [K]	$T_{w,rms}$ [K]	\dot{Q}_{rms} [kW]	$\dot{Q}_{Nr,rms}$ [%]	Q_{rms} [kWh]	$Q_{Nr,rms}$ [%]
Sensible cooling from 40°C to 0°C with 2000 l/h						
FP-SS-10hx	0.44	0.59	0.79	9.72	2.06	4.50
FP-SS-8hx	0.49	0.50	0.89	11.09	2.22	5.11
FP-SS-6hx	0.49	3.04	0.91	11.98	1.98	4.31
θ_{max}	0.49	3.04	0.91	11.98	2.22	5.11
θ_{avg}	0.47	1.38	0.86	10.93	2.09	4.64
Sensible cooling from 20°C to 0°C with 1000 l/h						
FP-SS-10hx	0.50	0.42	0.52	8.59	0.40	1.45
FP-SS-8hx	0.49	0.39	0.52	9.19	0.65	2.41
FP-SS-6hx	0.55	0.56	0.58	10.35	0.63	2.35
θ_{max}	0.55	0.56	0.58	10.35	0.65	2.41
θ_{avg}	0.51	0.46	0.54	9.38	0.56	2.07

Predictions of the outlet temperature of the heat exchanger shown in the upper part of Fig 4.5 agree very well with an average $T_{f,out,rms}$ between the three FP of 0.5 °C for both 2000 l/h and 1000 l/h.

The averaged storage temperature is also very well predicted with values of $T_{st,rms}$ below 0.6 °C for all simulations except for FP-SS-6hx and 2000 l/h with a value of 3 °C. The reason for this difference is ???.

The heat extracted from the storage is shown in the mid part of Fig 4.5. In this case differences are significant with averaged $N_{r,RMS}$ power differences of the three FP of 11 % and 9 % for 2000 l/h and 1000 l/h respectively. At around 9 hours for 2000 l/h, a peak in the power plot, which means a decrease in cooling power, can be observed in the simulations. This peak is predicted when the storage temperature is around 4 °C, i.e. when the maximum density of water is achieved and therefore the temperature inversion occurs. In the simulations this temperature inversion is assumed to be instantaneous, which is a simplification. In the predicted values the power and therefore the heat transfer coefficient rate is decreasing before the maximum density of water is achieved. After that, the power increases again because ice starts to form. This phenomenon is not observed in the experiments and therefore the model is not able to predict the behavior around 4 °C. Nevertheless, the non accurate predictions around 4 °C are not expected to influence the model when applied to a solar-ice system because this situation will likely appear once per year. Usually, as soon as ice is formed, the ice storage will be, at least partially, iced until the end of winter.

The cumulative extracted energy is well predicted with $N_{r,RMS}$ differences of 5 % and 2 % for 2000 and 1000 l/h respectively. Therefore, the under-prediction and over-prediction of the cooling power is compensated along the testing time with a good match at energy level.

Results of the heat transfer rate are shown in Fig 4.6. The heat transfer rate is clearly over predicted at the beginning of the test for 2000 l/h for all FP tested. After this initial process of around 2 hours, the predicted UA values for 2000 l/h flow with different numbers of heat exchangers are approaching each other. This is observed also in the experimental data for 8 and 10 hx, but not for 6 hx where a decrease of the UA is observed. Therefore, the increase of the number of heat exchangers from 8 to 10 does not

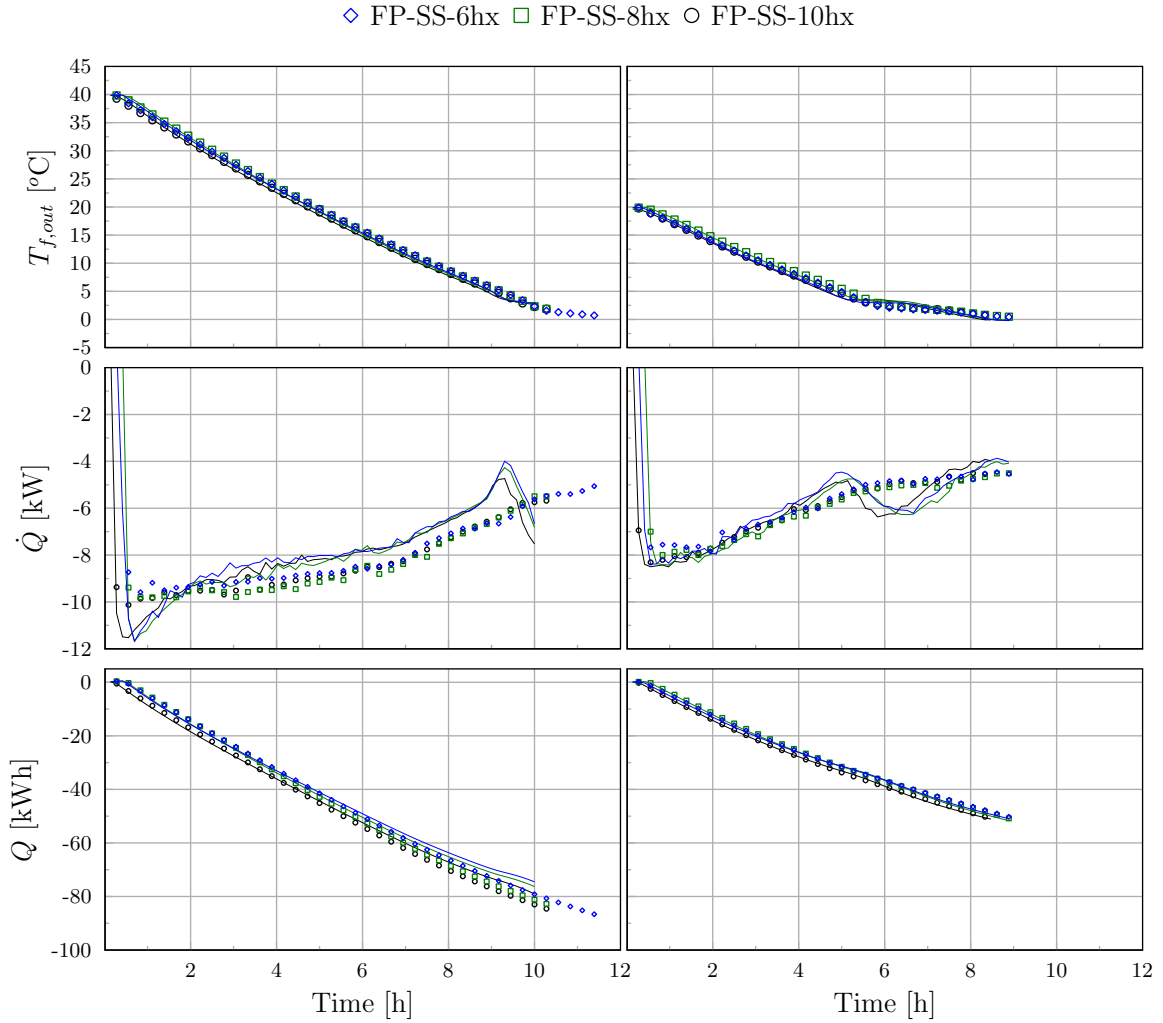


Figure 4.5: Simulation (solid lines) and experimental (symbols) results of FP for the sensible cooling test with (left) 2000 l/h and (right) 1000 l/h.

improve the performance after few hours of test. For 1000 l/h the UA values are well predicted, even at the beginning of the test. The main reason is probably the lower temperature of the storage at the beginning (20 °C instead of 40 °C). In the test with 1000 l/h there is a clear increase of the UA values both in simulations and in the experiments at around 6.5 hours. At this time ice starts to grow and the UA value is rising.

4.3.2 Capillary mats

For this testing sequence, results from CM-Stype-8hx have been disregarded due to a sudden stop in the cooling cycle caused by a problem with the chiller.

Predictions of the outlet temperature of the heat exchanger shown in the upper part of Fig. 4.7 agree very well with an average RMS difference between the four CM of 0.3 K for 2000 l/h and 0.4 K for 1000 l/h. These differences represent 0.7 % and 2 % for 2000 l/h and 1000 l/h respect to the maximum temperature of the testing sequence.

The averaged storage temperature is also very well predicted with averaged RMS values of 0.7 K and 0.4 K for 2000 l/h and 1000 l/h respectively. These represent around a 2 % difference respect to the maximum storage temperature achieved.

The heat extracted from the storage is shown in the mid part of Fig. 4.7. Averaged RMS power differences

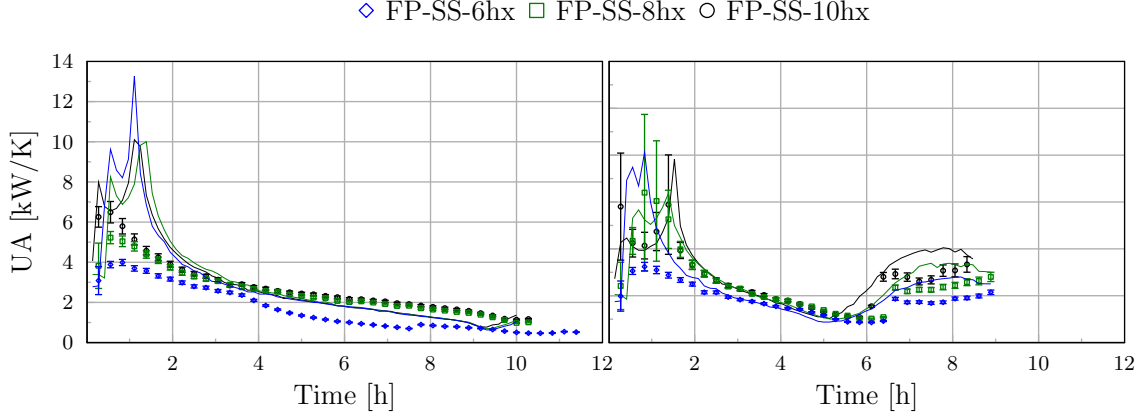


Figure 4.6: Heat transfer rate of FP for the sensible heating test with (left) 2000 l/h and (right) 1000 l/h.

Table 4.4: RMS differences between experiments and simulations for sensible cooling test using capillary mats.

	$T_{f,out,rms}$ [K]	$T_{w,rms}$ [K]	\dot{Q}_{rms} [kW]	$\dot{Q}_{Nr,rms}$ [%]	Q_{rms} [kWh]	$Q_{Nr,rms}$ [%]
Sensible cooling from 40°C to 0°C with 2000 l/h						
CM-Gtype-16hx	0.29	0.48	0.62	7.51	1.52	2.72
CM-Stype-16hx	0.33	0.63	0.71	8.48	1.49	2.67
CM-Gtype-8hx	0.34	0.76	0.72	9.43	1.23	2.35
CM-Stype-8hx	0.30	0.83	0.61	8.37	1.19	2.00
θ_{max}	0.34	0.83	0.72	9.43	1.52	2.72
θ_{avg}	0.31	0.67	0.67	8.45	1.36	2.43
Sensible cooling from 20°C to 0°C with 1000 l/h						
CM-Gtype-16hx	0.31	0.29	0.34	5.37	0.51	1.79
CM-Stype-16hx	0.35	0.60	0.40	5.88	0.31	1.09
CM-Gtype-8hx	0.49	0.62	0.58	9.58	1.19	3.56
θ_{max}	0.49	0.62	0.58	9.58	1.19	3.56
θ_{avg}	0.38	0.50	0.44	6.94	0.67	2.14

of 8 % and 7 % are observed for 2000 l/h and 1000 l/h respectively. Predictions show a decrease of power (a peak in the graphs) at the end of the test for all simulated cases. This decrease of power is not observed in experiments. The same phenomena has been observed for flat plates heat exchangers. The same reason given in section 4.3.1 for flat plate applies here, i.e. the model is not able to predict accurately heat transfer rates and the dynamics of the temperature inversions when the storage temperature is close to 4 °C.

The cumulative extracted energy is shown in the bottom part of Fig. 4.7. The energy extracted along time is very well predicted with averaged differences of $Q_{Nr,rms}$ of around 2 % for both 2000 and 1000 l/h. The instantaneous deviations of power along the test compensate with each other, leading to a good evolution of energy exchanged during time.

Results of the heat transfer rate are shown in Fig 4.8. The heat transfer rate is usually over predicted for a large time of the test for all CM and volume flow rates tested. As a consequence, all simulations tend to predict the decrease of the heat transfer rate when the storage water is close to 0 °C and ice starts to be formed earlier. The larger the area, the larger the peak decrease. Interestingly, the UA profiles follow the \dot{Q} profiles in all simulations, but this is not observed in all experiments. Experiments with 16hx shows a valley in UA that can not be seen in \dot{Q} measurements. When 8hx are used, simulations predict a valley in the UA which can not be observed in measurements.

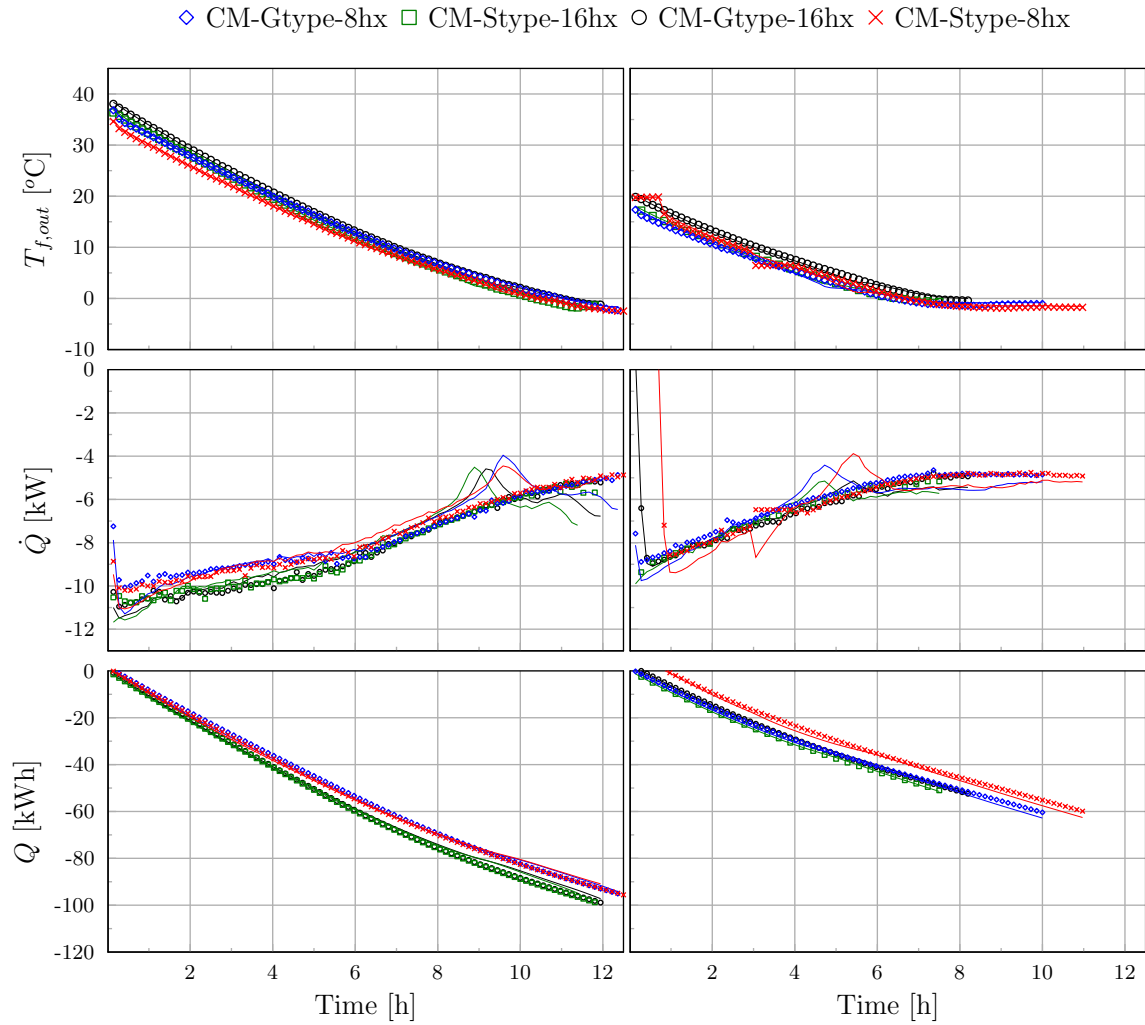


Figure 4.7: Simulation and experimental results of CM for the sensible cooling test with (left) 2000 l/h and (right) 1000 l/h.

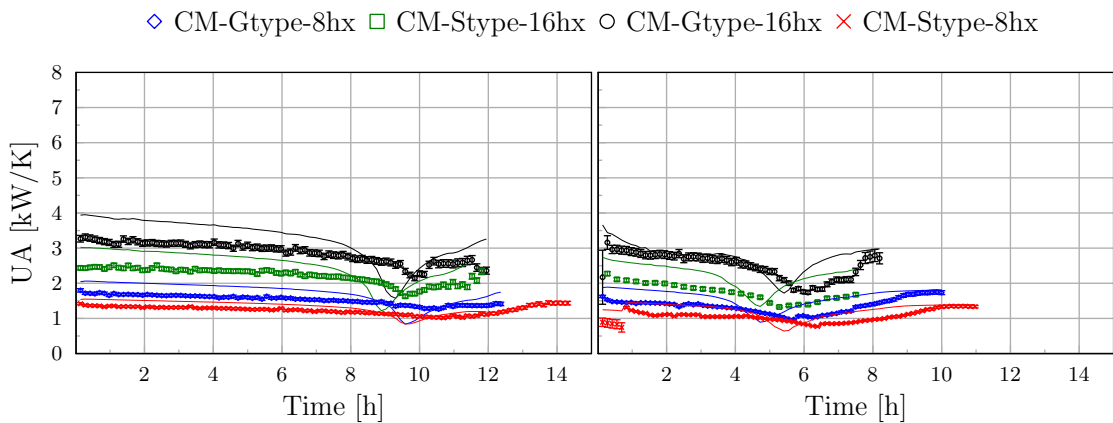


Figure 4.8: Heat transfer rate of CM for the sensible heating test with (left) 2000 l/h and (right) 1000 l/h.

4.4. Icing cycle

The experiments for the icing cycle have been presented in section 2.6.3. The cycle consist on icing the water of the storage which temperature is initially close to 0 °C by circulating a colder brine through the heat exchangers until the icing fraction is close to 98 % or testing time is larger than 3 days.

4.4.1 Flat plates

Experimental and numerical results for the icing test are provided in Fig. 4.9 and Fig. 4.10 for (left) 2000 l/h and (right) 1000 l/h for all FP tested. Quantified differences between simulations and experiments are provided in Table 4.5.

Table 4.5: RMS differences between experiments and simulations for solidification test using flat plates.

	$T_{f,out,rms}$ [K]	\dot{Q}_{rms} [kW]	$\dot{Q}_{Nr,rms}$ [%]	Q_{rms} [kWh]	$Q_{Nr,rms}$ [%]
T5 : Icing with 2000 l/h					
FP-SS-10hx	0.37	0.82	28.05	5.57	4.09
FP-SS-8hx	0.29	0.69	28.05	7.66	5.51
FP-SS-6hx	0.22	0.39	20.26	2.08	1.31
θ_{max}	0.37	0.82	28.1	7.7	5.5
θ_{avg}	0.30	0.6	25.5	5.1	3.6
T5 : Icing with 1000 l/h					
FP-SS-10hx	0.64	0.71	29.74	5.17	3.62
FP-SS-8hx	0.50	0.54	22.27	2.42	1.72
FP-SS-6hx	0.34	0.36	15.14	2.75	1.98
θ_{max}	0.64	0.71	29.7	5.2	3.6
θ_{avg}	0.49	0.5	22.4	3.4	2.4

Figures presented in this section for the icing test are modified with respect to the previous sections where sensible heating and cooling phenomena was taking place. Fig. 4.9 shows the outlet temperature of the heat exchanger (top), the ice fraction (mid) and the cumulative energy extracted from the storage (bottom) as a function of time. Fig. 4.10 shows the icing power and the UA value as a function of the ice fraction.

Predictions of the outlet temperature of the heat exchanger shown in the upper part of Fig. 4.9. It should be mentioned that the sudden change of the outlet temperature between 25 h and 30 h has nothing to do with the behavior of the ice storage but it is an artifact caused by the chiller. When the outlet temperature of the chiller (inlet of the heat exchanger) was around -7 °C the chiller activated an internal heating to avoid freezing the refrigerant. This was not foreseen and it is disturbing the interpretation of the results. This step change of the inlet is also causing some higher differences in the model which can not dynamically react as the experiments. The main reason is because the model is neglecting the sensible heat of the ice, while in reality parts of the ice are subcooled down to -7 °C. When a boundary condition is changed drastically the sensible capacity of the ice plays a role increasing the differences between simulations and experiments. The fact that the subcooling of the ice is neglected is probably one of the main reasons why the temperature is over-predicted in the last phase of the test. Nevertheless, even with all this complexity added on, the heat exchanger temperature is predicted with averaged differences of $T_{f,out,rms}$ of 0.3 °C for 2000 l/h and of 0.5 °C for 1000 l/h, which represents differences in the order of 4 % to 6 % respect to the total temperature difference along the test (8 °C in this case).

The averaged temperature of the storage and its quantified difference is not provided because almost all water is solidified and the sensors are showing the temperature of the ice and not of the remaining liquid water in the storage.

The ice fraction is shown in the middle of Fig. 4.9. Results are only compared until an ice fraction of 80 % which represents 100% of the height where the heat exchangers are active. In the experiments higher ice fractions were achieved with ice growing on the top surface of the packed ice cube with all heat exchanger plates. Growing ice on this conditions is not implemented in the model and not relevant because in a real ice storage the heat exchangers should cover all or almost all the effective height of the storage. Interesting to note that the use of several control volumes in the heat exchanger length allows to smooth the effect of the ice constraint and predictions follow the experiments results relatively well.

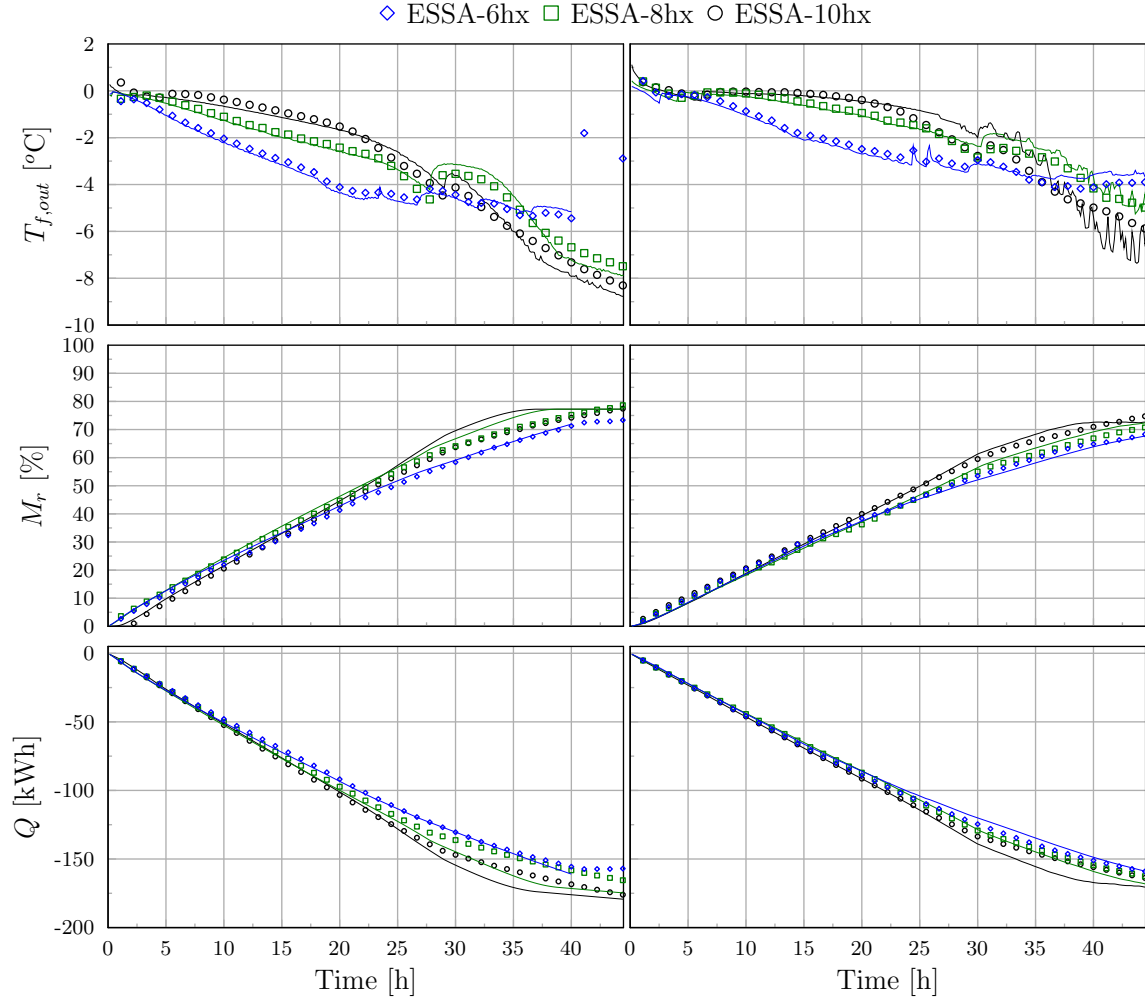


Figure 4.9: Simulation and experimental results for the icing test with (left) 2000 l/h and (right) 1000 l/h.

The cumulative energy is obviously following ice fraction profile. The only difference between both results are due to the sensible heat of ice and the heat gains from the storage walls. The averaged difference of the normalized energy extracted Q_{Nr}^{rms} is of 4 % and 2 % for 2000 l/h and 1000 l/h respectively.

Icing power and UA value as a function of the ice fraction are shown in Fig. 4.10. The icing power shows a quite stable profile until a mass ice fraction of approximately 40 %. Above this mass fraction predicted results from 8 and 10 hx show an increase of power which is not observed in the experiments. The main reason is that the inlet temperature decreases and this is increasing the simulated power because the model neglects that the ice is subcooled below 0 °C.

The step change of power observed in experiments and simulations between 50 and 65 % are an artifact due to the chiller problem explained above and have nothing to do with ice constraint. This step change in the inlet temperature due to the chiller artifact difficulties the interpretation of the results when the power is used. Results are better explained when the UA is plotted as shown in the bottom part of Fig. 4.10.

The heat transfer rate has a peak in the low mass fraction region which depends on the number of heat exchangers and mass flow rate. This peak corresponds ice thickness of few millimeters, but because of the different number of heat exchangers, the peak is moved in the ice fraction axes. After this peak, the heat transfer rate decreases until reaching very low values at 80 % ice fraction, which corresponds to 100 % of the storage volume height occupied by the heat exchanger. When the mass flow rate is reduced from 2000 to 1000 l/h the peak of UA is shifted to higher mass fractions due to the lower power extracted.

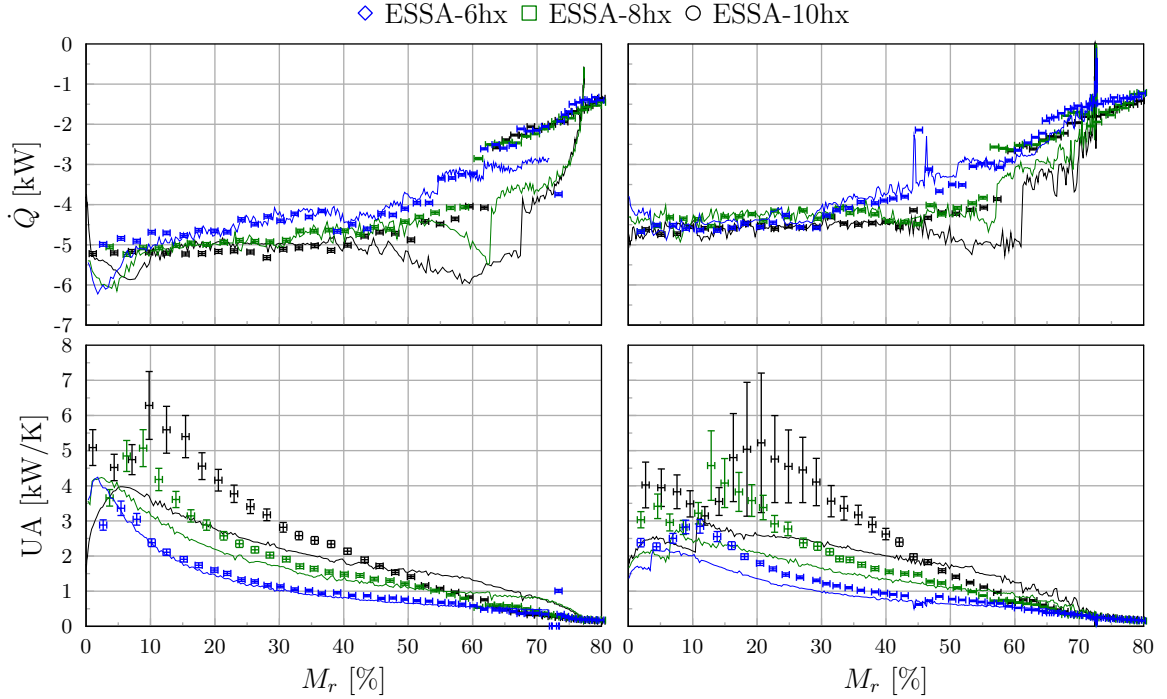


Figure 4.10: Simulation and experimental results for the icing test as function of the mass ice fraction with (left) 2000 l/h and (right) 1000 l/h.

The peak has the highest uncertainty because the outlet is closer to 0 °C reducing the logarithmic mean temperature difference. The UA is way off compared to experiments because an error in the outlet temperature leads to an error in the power predicted and also in the LMTD and, thereby, the UA adds all these errors. For example, a 6 % higher outlet temperature can lead to a 12 % lower power and 17 % higher LMTD. A division by this lower power divided by the higher LMTD leads to a 25 % lower UA.

4.4.2 Capillary mats

Experimental and numerical results for the icing test are provided in Fig 4.11 and Fig 4.12 for (left) 2000 l/h and (right) 1000 l/h for all CM tested. Quantified differences between simulations and experiments are provided in Table 4.6.

The outlet temperature of the heat exchanger is shown in the upper part of Fig. 4.11 as a function of time. Numerical predictions are in good agreement with experimental data with average differences of $T_{f,out}^{rms}$ between all CM heat exchangers of 0.3 K and 0.6 K for 2000 l/h and 1000 l/h respectively. These absolute RMS differences correspond to 3 % and 7 % respect to the total temperature difference of the test (8 K for the icing case).

The ice fraction is shown in the middle section of Fig. 4.11. Very high ice fractions were achieved for all capillary mats and mass flow rates. No damaging of the casing was observed with any of the heat exchangers used. Regarding the simulations, with the exception of S-type-8hx case, the ice fraction is over-predicted by the simulated cases until the maximum predicted ice fractions is reached. The main explanation is that the model is neglecting the heat capacity of ice and therefore the energy extracted is used completely to ice. The maximum ice fraction observed in the experiments was not achieved in the simulations for 16 number of heat exchangers, since some water volume was necessary to solve the system of equations.

The predicted cumulative energy extracted is following the same pattern as the mas fraction. Averaged normalised energy differences of all simulations $Q_{N_r}^{rms}$ in the order of 6 % and 7 % for 2000 l/h and 1000 l/h respectively are found. The model developed for ice constraintment shows to work properly even in the case of highly asymmetry between tubes, i.e. Stype-8hx. Differences between simulations and

experiments are more or less in the same order of magnitude for all cases. Thus, the model predicts similarly both symmetric and highly non-symmetric heat exchangers configurations. Variations on the volume flow are also predicted with similar accuracy.

Predictions of instantaneous power show higher differences compared to energy along the testing time. Differences in the order of 16 - 23 % of $\dot{Q}_{Nr,rms}$ are observed in all cases. Heat power predictions are shown in Fig. 4.12 as a function of the ice fraction. Differences in Fig. 4.12 might not be corresponding exactly to what has been quantified in Table 4.6, because quantified differences presented in the table are obtained with differences along the time. Fig. 4.12 shown results along the ice fraction and therefore results are coupled with prediction of the ice fraction too. The step changes in power predictions, e.g. at 50 % Mr for Stype-8hx are due to the artifact of the chiller and have nothing to do with ice constraintment. UA values are very well predicted. The heat transfer rate UA for the icing test is calculated in both experiments and simulations considering the storage water is at 0 °C. The temperature sensors for water in the ice storage were covered with ice and temperatures were measuring values down to -7 °C and were obviously not representing the temperature of the liquid remaining water. The good results of the UA show that the model is able to predict appropriately the heat transfer with constrained ice under different heat exchangers set ups. Predictions of heat power show much larger differences, partially due to the simplification of considering that ice is always at 0 °C. As said before temperature sensors in the storage were measuring values of -7 °C. Subcooling 2000 kg of ice to -7 °C needs about 8 kWh, around 4 % of the total energy needed in the icing process. Therefore, it is of relevance and should be included in future works.

Table 4.6: RMS differences between experiments and simulations for solidification test using capillary mats.

	$T_{f,out}^{rms}$ [K]	\dot{Q}^{rms} [kW]	\dot{Q}_{Nr}^{rms} [%]	Q^{rms} [kWh]	Q_{Nr}^{rms} [%]
T5 : Icing with 2000 l/h					
CM-Gtype-16hx	0.39	0.87	20.17	7.23	6.29
CM-Stype-16hx	0.37	0.79	21.54	9.60	6.91
CM-Gtype-8hx	0.33	0.73	16.83	7.00	5.90
CM-Stype-8hx	0.28	0.59	16.13	7.83	6.23
θ_{max}	0.4	0.9	21.5	9.6	6.9
θ_{avg}	0.3	0.7	18.7	7.9	6.3
Icing with 1000 l/h					
CM-Gtype-16hx	0.77	0.87	22.97	8.00	6.77
CM-Stype-16hx	0.66	0.73	16.97	5.96	4.91
CM-Gtype-8hx	0.75	0.84	23.54	7.28	6.08
CM-Stype-8hx	0.40	0.42	16.98	6.74	4.67
θ_{max}	0.8	0.9	23.5	8.0	6.8
θ_{avg}	0.6	0.7	20.1	7.0	5.6

4.5. Melting cycle

The experiments for the melting cycle have been presented in section 2.6.4. The cycle consist on melting the ice of the storage with a set fluid temperature of 10 °C. However, as already discussed before, the fluid inlet temperature in the heat exchangers is changing over time because the chiller (heating device in this case) is connected directly to the heat exchangers and has not enough power to raise the temperature from 0°C to 10 °C with the given volume flow. Each experiment started at a slightly different ice fraction due to the whole testing sequence previous to the melting test sequence. All tests from sensible heating, cooling and icing were in series for each mass flow. However, between the icing and the melting experiments, a cycling sequence was tested and thus, the initial M_r depends on the cycling test. Results from the cycling test are provided in section 4.6. The melting test sequence was finished when the storage temperature was at 10 °C approximately. After this sequence the whole process with 1000 l/h was started. This is why the sensible heating sequence for 1000 l/h starts at 10 °C and not at 20 °C.

The measurements of the ice fraction were not accurate for the melting process in all cases. Therefore, in order to plot the ice fraction from the experiments, it has been calculated based on the energy extracted considering the sensible heat of water when being heated to 0 °C, but neglecting the heat losses though the storage walls and the sensible heat stored in the ice.

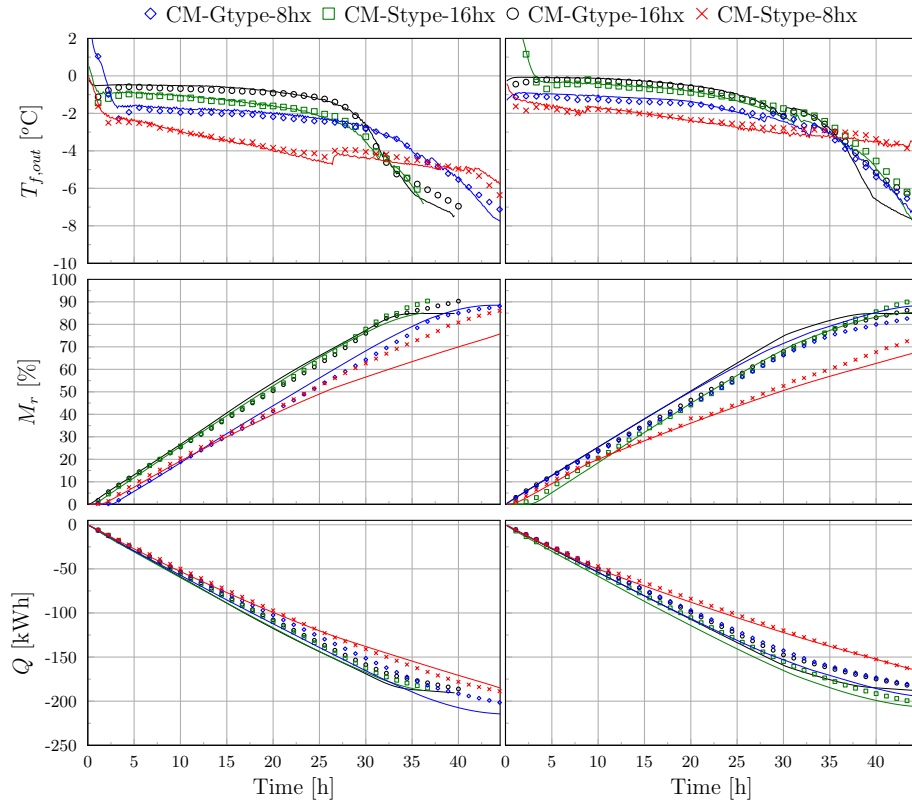


Figure 4.11: Simulation and experimental results of CM for the icing test with (left) 2000 l/h and (right) 1000 l/h.

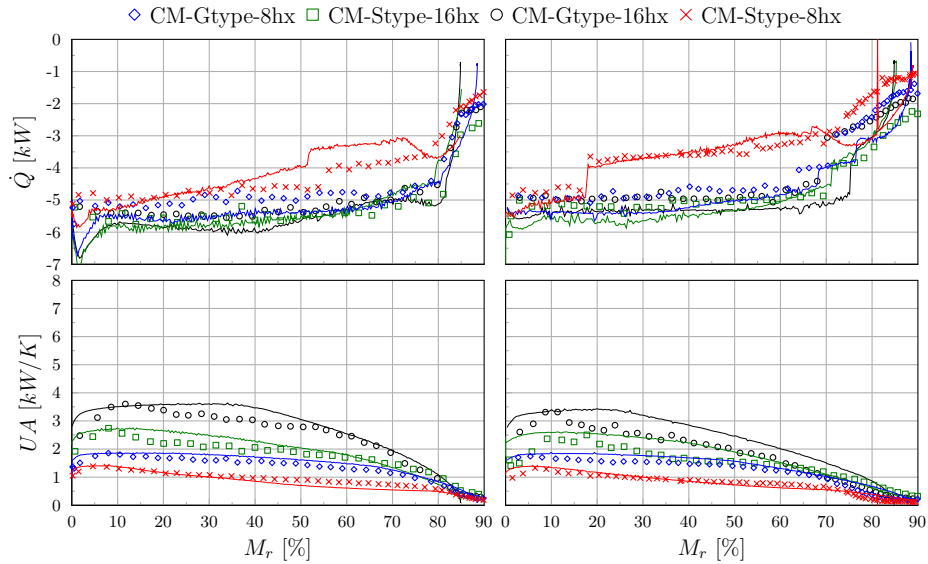


Figure 4.12: Simulation and experimental results for the icing test as function of the mass ice fraction with (left) 2000 l/h and (right) 1000 l/h.

4.5.1 Flat plates

The predicted outlet temperatures of the heat exchanger and the averaged temperature of the storage are shown in Fig 4.13. RMS differences are presented in Table 4.7

The outlet temperature of the heat exchanger is shown in the upper graphs of Fig. 4.13. Predictions follow relatively well the experimental data. However, an overprediction of $T_{f,out}$ is usually observed when the storage is being heated up, i.e. when the sensible heating phase starts to be dominant. This means that the power is underpredicted when most of the ice has been already melt. The storage temperature is shown in the middle graphs of Fig. 4.13. At beginning of the test the sensors are covered with solid ice and temperatures of -7 °C are measured. However, the value T_{store} refers to the remaining water temperature and therefore experimental results have been limited to ≥ 0 °C. Averaged RMS differences of the outlet heat exchanger temperature $T_{f,out}^{rms}$ of 0.63 K and 0.84 K are observed for 2000 l/h and 1000 l/h volume flows. These difference represent 6 % and 8 % respect to the temperature difference along the test (10 °C for melting test).

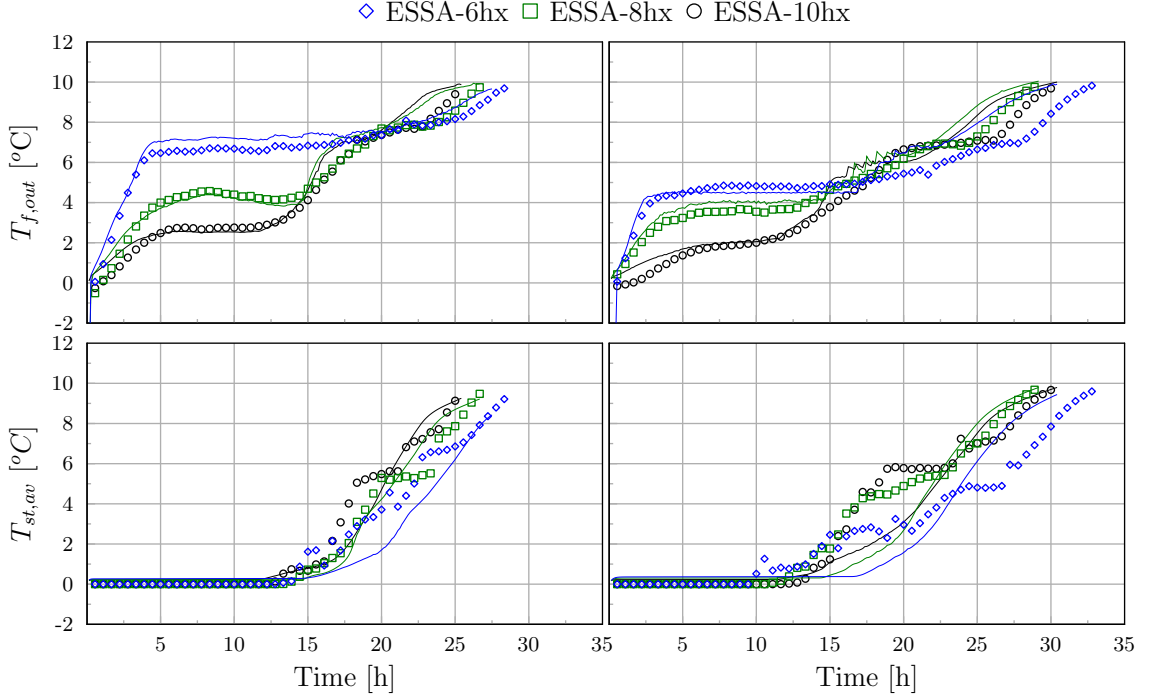


Figure 4.13: Simulation and experimental results for the melting test with (left) 2000 l/h and (right) 1000 l/h.

Table 4.7: RMS differences between experiments and simulations for melting test using flat plates.

	$T_{f,out}^{rms}$ [K]	\dot{Q}^{rms} [kW]	\dot{Q}_{Nr}^{rms} [%]	Q^{rms} [kWh]	Q_{Nr}^{rms} [%]
T9 : Melting with 2000 l/h					
FP-SS-10hx	0.64	1.36	19.58	7.34	7.69
FP-SS-8hx	0.70	1.49	22.10	6.38	6.49
FP-SS-6hx	0.54	1.10	16.38	14.91	13.97
θ_{max}	0.70	1.49	22.1	14.9	14.0
θ_{avg}	0.63	1.3	19.4	9.5	9.4
T9 : Melting with 1000 l/h					
FP-SS-10hx	0.73	0.75	13.37	5.77	5.56
FP-SS-8hx	0.61	0.61	10.98	5.68	5.77
FP-SS-6hx	1.06	1.13	20.98	4.28	4.20
θ_{max}	1.06	1.13	21.0	5.8	5.8
θ_{avg}	0.80	0.8	15.1	5.2	5.2

The predicted cumulative energy provided to the storage, shown in Fig. 4.14, is relatively well predicted except for the case with 6 hx and 2000 l/h. For this case the Nusselt number for the natural convection is underestimated. A reason could be the large distance between plates, allowing in one hand to easily detach ice plates from the heat exchangers and in the other hand enhancing natural convection. The detachment of plates is not considered in the present model and this increases the heat transfer area

of ice plates since two surfaces are used to melt instead of the one close to the heat exchanger when not detached. Averaged differences between heat exchanger units in normalized RMS cumulative energy Q^{rms} are in the order of 10 % and 63 %, with the largest difference of 14 % for 6 hx units and 2000 l/h.

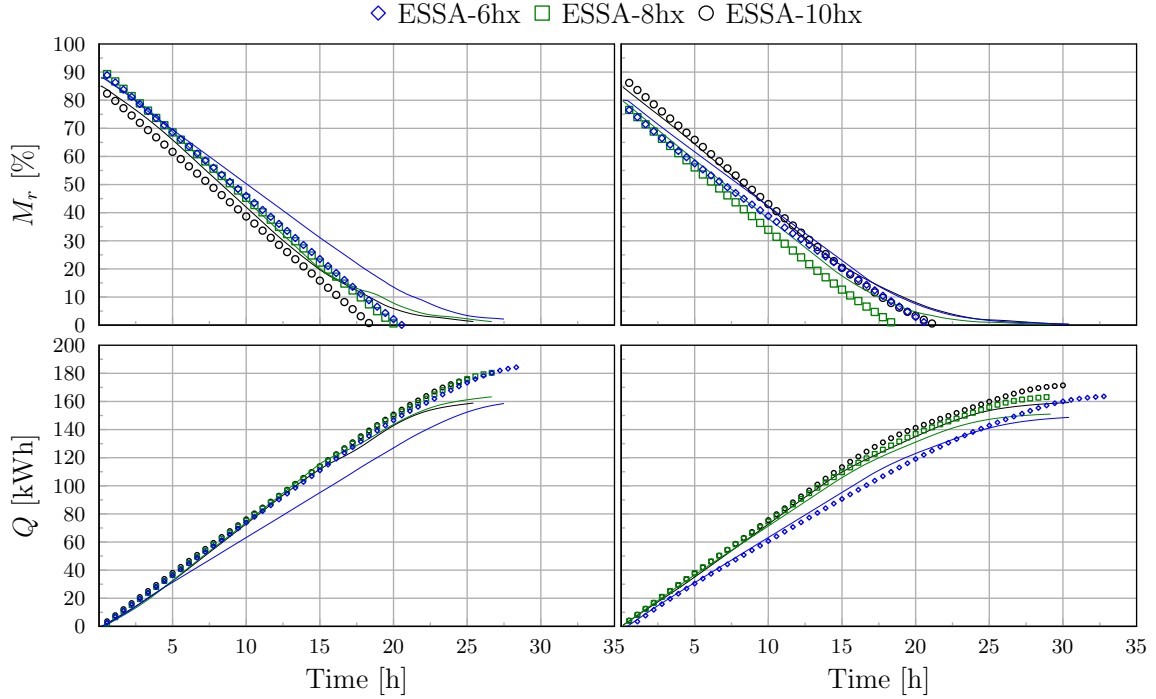


Figure 4.14: Simulation and experimental results for the melting test with (left) 2000 l/h and (right) 1000 l/h.

The mass fraction of ice has been also plotted in Fig. 4.14 in order to know what was the initial ice content for each case. For the experimental case, the M_r^* has been used, i.e. the ice fraction is calculated using the energy extracted since measures were not very accurate (see section 2.6.4 for details).

The melting power and the heat transfer rate UA are shown in Fig. 4.15 as a function of the ice fraction M_r for simulations and ice corrected fraction M_r^* for the experiments. Notice that the test starts with the highest ice fraction and, thereby, results at the beginning of the test are plotted in the right hand side of the x-axis. The melting sequence can be split in three phases, the first one where heat conduction is dominant ($M_r \geq 60$ % approx). When the melted plates are large enough, convection starts to be the dominant effect. In the third phase ($M_r \leq 10 - 20$ % approx), plates detach from heat exchangers. After the detachment, these plates are pushed towards the surface due to the density gradient between water and ice and are melted faster due to the higher temperature on the upper part of the storage and also due to the larger melting surface area, i.e. two faces per plate instead of the one close to the heat exchanger when *attached* to it are used for melting. The detachment of flat plates is not considered in the present model.

In general the model underpredicts melting UA rates when conduction is dominant and also when ice plates are floating to the surface (low M_r values). The highest different is found with 6 hx and 2000 l/h where the model clearly underestimates the melting power. Interestingly, predictions are in good agreement when 6 hx and 1000 l/h are used. For 1000 l/h both experiments and simulations show a lower melting power compared to 8 hx and 10 hx units. For 2000 l/h simulations show the same behaviors, i.e. predictions of lower melting power, but this is not observed in the experiments where the power is very similar to that when 8 hx or 10 hx units are used.

The UA values are relatively well predicted during most of the convective dominant melting ($20 \geq M_r \leq 69$). High differences are observed in the low ice fraction region ($M_r \leq 20$), specially for 1000 l/h. Both experiments and simulations show a UA valley for 2000 l/h in the region $5 \geq M_r \leq 15$. However, simulations tend to shift this valley towards higher ice fractions and the valley is more pronounced in the simulations. For 1000 l/h this valley is not observed in the experiments and only slightly in the simulations.

In fact, experiments show a peak for 8 and 10 hx units, instead of a valley, at low ice fractions when 1000 l/h are used. Probably plates are detached for these cases increasing the melting rates as explained above. Clearly, the phenomena of detachment under this conditions is somewhat chaotic and difficult to predict. In the model presented in Carbonell et al. (2015), the detachment of ice plates was modelled for a thermal de-icing concept. However, for when de-icing is used ice plates are always thin and the ice from the tow faces of the heat exchanger are never in contact. Therefore, detachment of ice plates can be controlled and thus modelled. In the present case, plates can detach or not depending on many phenomena that can not be modelled.

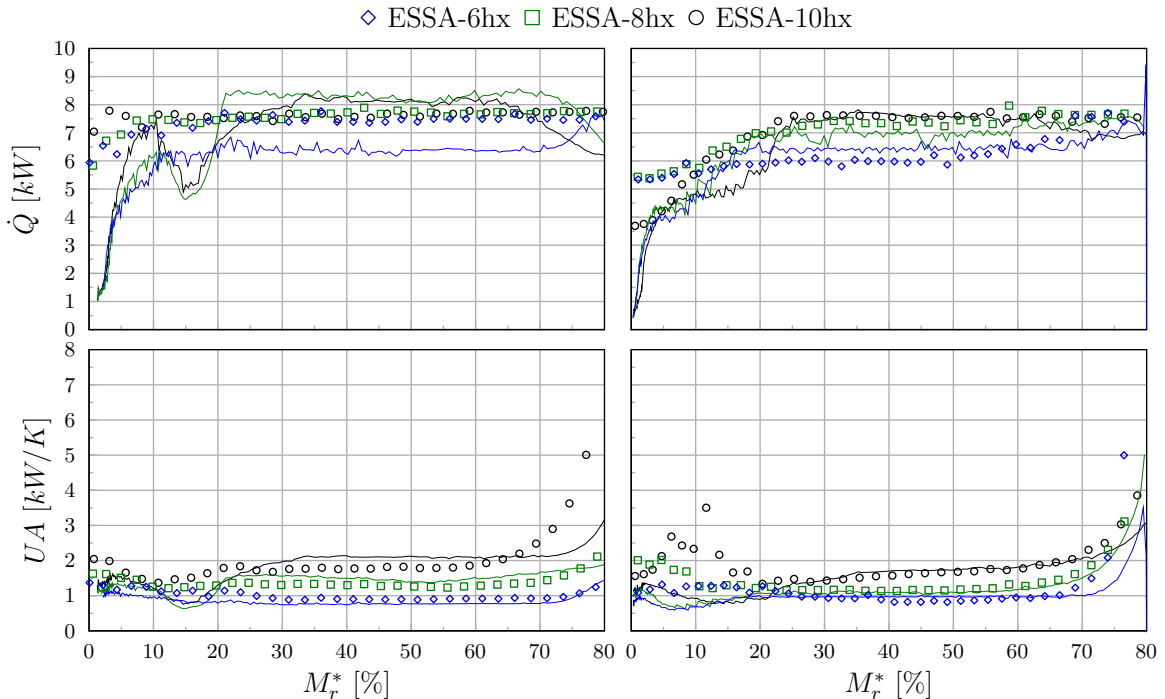


Figure 4.15: Simulation and experimental results for the melting test as function of the corrected mass ice fraction with (left) 2000 l/h and (right) 1000 l/h. M_r^* is used for experiments and M_r for simulations.

4.5.2 Capillary mats

The predicted outlet temperatures of the heat exchanger and the averaged temperature of the storage are shown in Fig 4.16. Quantified RMS differences for CM simulations are presented in Table 4.8.

The outlet temperature of the heat exchanger, shown in Fig. 4.16, is well predicted until sensible heat becomes dominant. The storage temperature shown in the bottom part of Fig. 4.16 increases faster in the simulations. This means that the power is overpredicted when most of the ice has been already melt. Averaged $T_{f,out}^{rms}$ RMS differences between all CM is of 0.6 K and 1.2 K are observed for 2000 l/h and 1000 l/h volume flows.

The cumulative energy along with the ice fraction is shown in Fig. 4.17. All simulations end the melting test with lower energy values. There are two main reasons are this. The first one is that the whole block of ice before being melted was at temperatures below 0 °C. All these energy is neglected in the model. Moreover, in some cases it is not possible to start the model with the same initial mass of ice than in the experiments because the model needs some liquid water to solve the system of equations (see Eq. 13). Besides these differences found at the end of the test, there is one case where differences are clearly larger compared to the others, i.e. Stype-16hx. For this case the model is over-predicting the cumulative energy substantially with normalized RMS $Q_{N_r}^{rms}$ of 12 %. However, the averaged values for all cases are around 6 % and 5 % for 2000 l/h and 1000 l/h respectively.

The melting power and heat transfer rates are shown in Fig. 4.18 respect to the ice fraction. Melting rates for 2000 l/h are well predicted for G-type, but for S-type large differences are found. In general

Table 4.8: RMS differences between experiments and simulations for melting test using capillary mats.

	$T_{f,out}^{rms}$ [K]	\dot{Q}^{rms} [kW]	$Q_{N_r}^{rms}$ [%]	Q^{rms} [kWh]	$Q_{N_r}^{rms}$ [%]
T9 : Melting with 2000 l/h					
CM-Gtype-16hx	0.47	0.98	14.04	1.94	2.05
CM-Stype-16hx	0.90	1.95	42.69	11.16	11.99
CM-Gtype-8hx	0.27	0.54	11.68	5.21	6.08
CM-Stype-8hx	0.70	1.53	27.84	5.06	5.01
θ_{max}	0.90	1.95	42.7	11.2	12.0
θ_{avg}	0.58	1.2	24.1	5.8	6.3
T9 : Melting with 1000 l/h					
CM-Gtype-16hx	0.77	0.83	12.62	2.05	2.12
CM-Stype-16hx	0.98	1.04	23.21	3.93	4.27
CM-Gtype-8hx	0.70	0.68	15.08	2.33	2.71
CM-Stype-8hx	1.85	0.80	16.69	2.33	2.67
θ_{max}	1.85	1.04	23.2	3.9	4.3
θ_{avg}	1.07	0.8	16.9	2.7	2.9

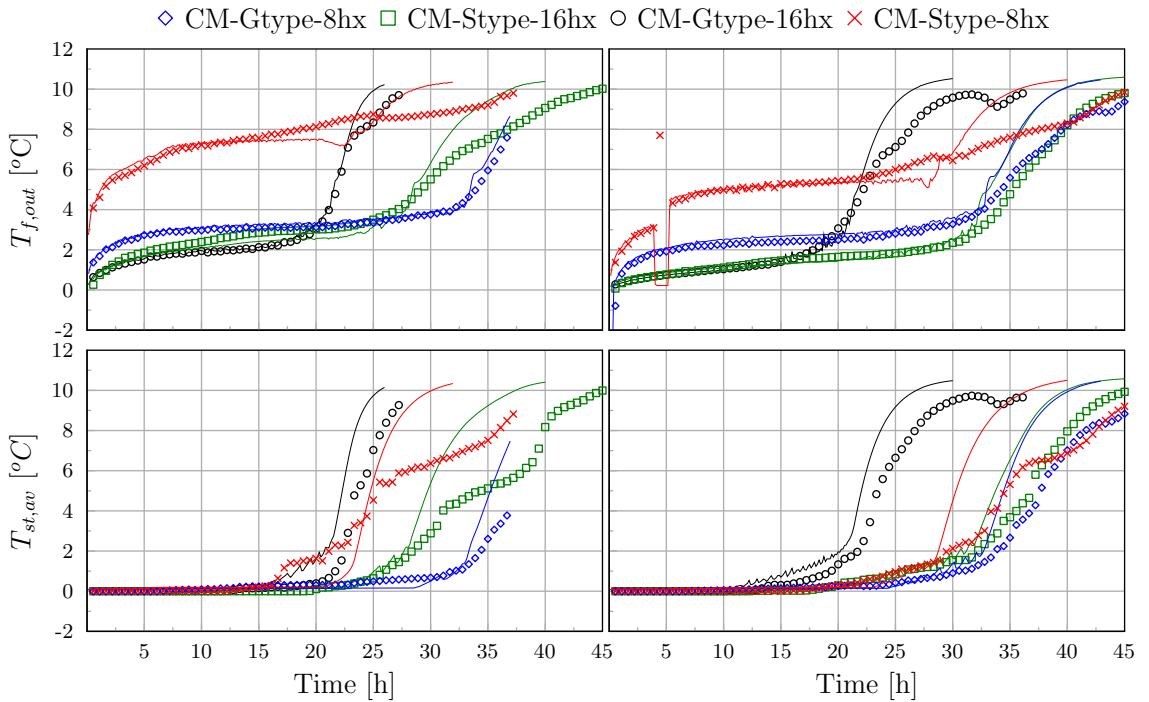


Figure 4.16: Simulation and experimental results for the melting test with (left) 2000 l/h and (right) 1000 l/h.

results for melting for S-type are significantly worse compared to the other cases. The reason, why it is like that, is not clear yet. The melting power predicted for S-type-16hx is overpredicted during all the test. For S-type-8hx the model overpredicts significantly the melting power for $M_r \leq 40$ approximately. The melting power of Stype-8hx shows a different behaviour compared to all other cases with a clear decrease of power for low ice fractions. However, the UA value shows a relatively constant value, which means that the change of storage temperature makes the difference in the power predictions. For 1000 l/h, melting power is much better predicted. Even though average normalized RMS power $\dot{Q}_{N_r}^{rms}$ is in the order of 16 % for 1000 l/h, most of the differences are at the end of the test when for simulations the power tends to zero but experimental data still shows some power values due to the larger energy that can be extracted in experiments for the higher initial ice fraction and subcooling of ice.

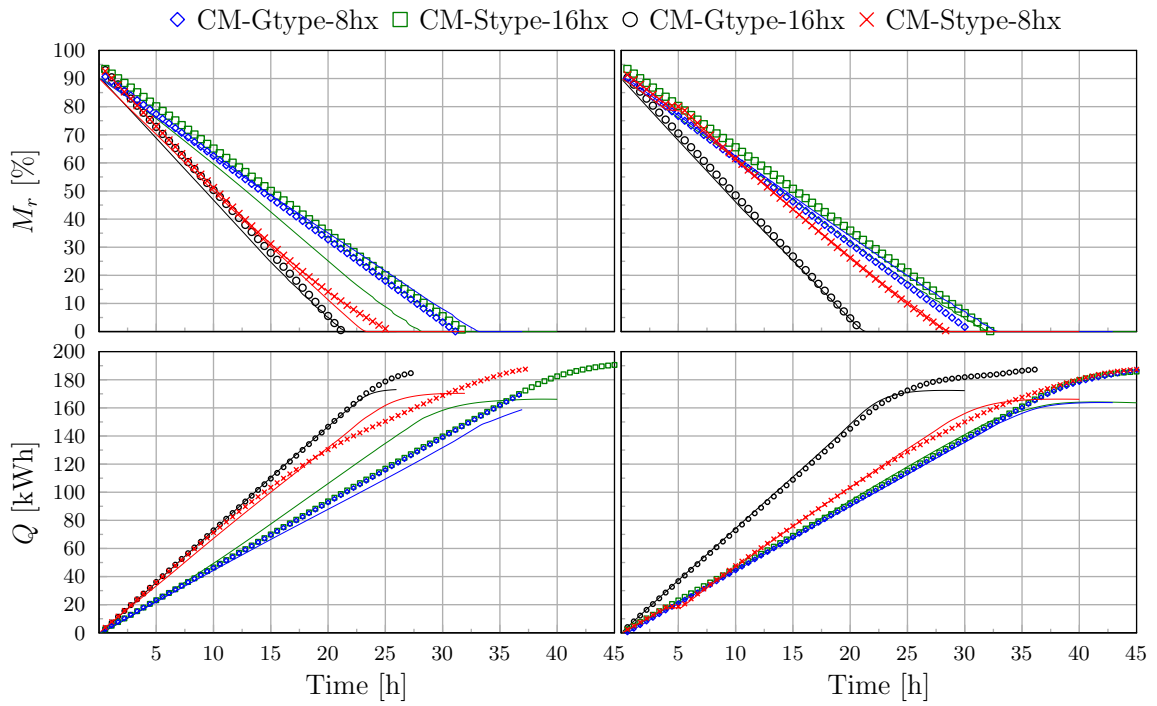


Figure 4.17: Simulation and experimental results for the melting test with (left) 2000 l/h and (right) 1000 l/h.

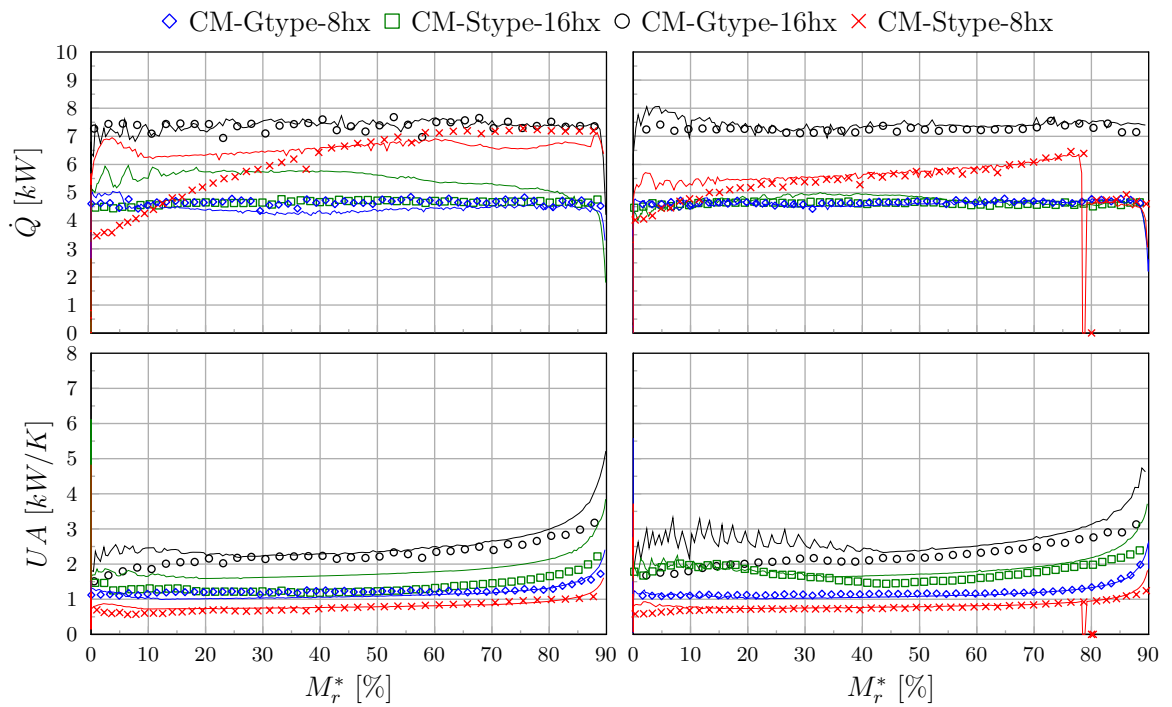


Figure 4.18: Simulation and experimental results for the melting test as function of the mass ice fraction with (left) 2000 l/h and (right) 1000 l/h. M_r^* is used for experiments and M_r for simulations.

4.6. Cycles of icing and melting

Simulated and experimental results of the test considering cycles of heating and cooling on icing and melting conditions are shown in Fig. 4.19 for 1000 l/h and in Fig. 4.20 for 2000 l/h. The three tested number of heat exchangers are shown in those figures, 6 hx in the left, 8 hx in the mid and 10 hx in the right side. In the upper part of the figures the simulated ice thickness is provided (left axes) and the inlet and outlet temperature of the heat exchangers (right axis).

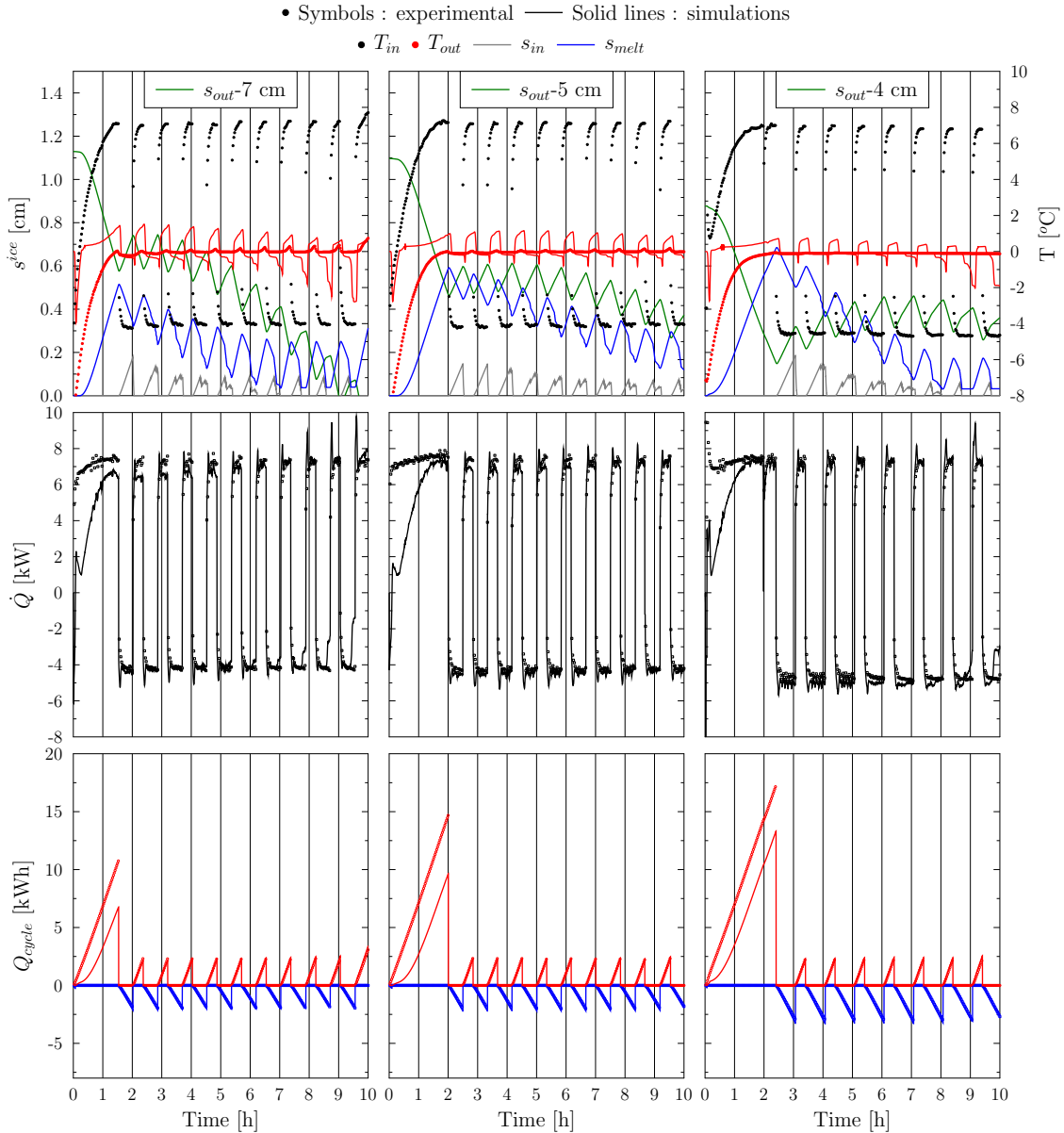


Figure 4.19: Simulation and experimental results of the icing and melting cycle T8 with 1000 l/h for (up) FP-6hx (mid) FP-8hx and (bot) FP-10hx.

The simulated ice thickness is shown for the outlet thickness s_{out} , for the internal thickness s_{in} and for the melted thickness s_{melt} . Explanations of these thickness are provided in section 3. The fix constant value per set of heat exchangers has been subtracted from the outlet ice thickness in order to plot all results with a smaller range, e.g. for 6 hx the outlet ice thickness is reduced by 7 cm in order to be plotted in the range of 0 to 1.4 cm. The power for melting and icing is shown in the mid part of the figures. The cumulative energy provided by the heat exchangers Q_{cycle} for melting and icing for each heating and cooling cycle is shown in the bottom part of each figure. All the cycling test starts with a

melting phase that last until the experimental outlet temperature of the heat exchanger is above 0 °C. This phase is needed in order to ensure that the cycling test allows to melt and ice. Otherwise the heating and cooling cycles could only change the temperature from the ice from -8 °C to 0 °C without actually melting any ice. The model is not prepared to work under the subcooled zone and the solid ice is always assumed to be at 0 °C. This is the reason why in all cases simulated results in the first meting phase are always over-predicting the temperature and thus under-predicting the power and the melted energy. In the experiments the ice is at temperatures down to -8 °C increasing the extracted power respect to the simulations where the ice is assumed to be at 0 °C. In this initial phase the outlet ice thickness decreases rapidly as the melted ice thickness increases. After this initial phase the icing and melting cycles start. In each cycle of icing and melting the internal ice thickness increases reducing the melted ice thickness and increasing the total ice thickness correspondingly. When a second cycle starts, if the internal ice thickness has not reached the melted ice the internal ice thickness is assumed to stick to the external ice thickness. As soon as the internal ice thickness reaches the melted thickness, the melted and internal ice thickness are set to zero and the whole ice thickness is in one block. This can be observed in Fig. 4.20 after the first cycle for 6 hx (left graphs), between 1 and 2 hours.

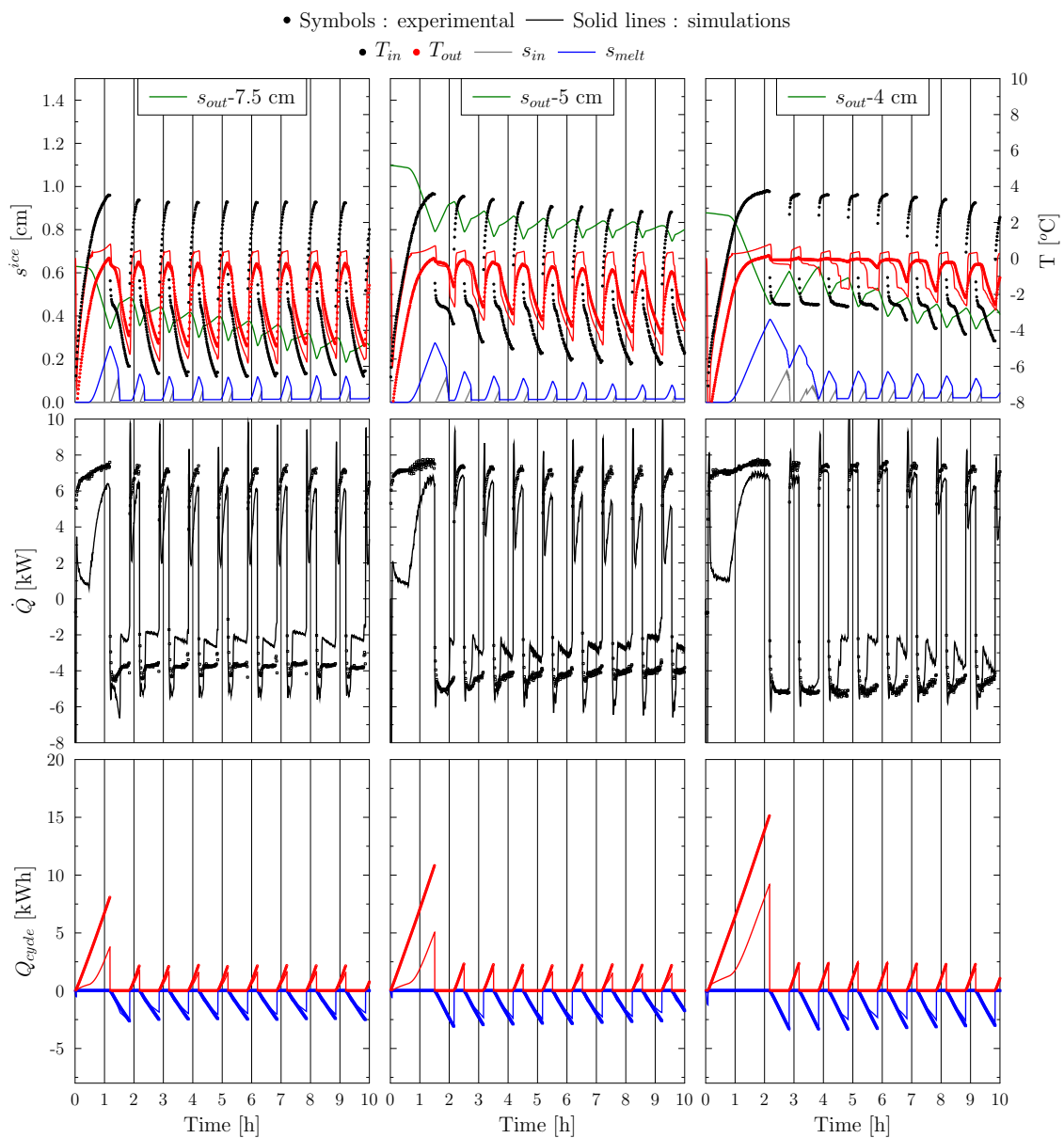


Figure 4.20: Simulation and experimental results of the icing and meting cycle T8 with 2000 l/h for (up) FP-6hx (mid) FP-8hx and (bot) FP-10hx.

Looking at the temperature of the heat exchanger for 1000 l/h it can be seen that in the experiments the outlet temperature is very stable at 0 °C even when the inlet is at 7 °C. This is probably due to the sensible “cold” accumulated in the ice. The outlet predicted temperatures in the icing mode are usually well predicted and close to 0 °C except when the internal ice thickness reaches the melted thickness. In this circumstances, the ice resistance increases because all ice thickness in in one block and therefore the outlet temperature decreases when icing. This is not observed in the experiments because in reality multiple ice layers are possible and the icing always start to form without any ice on the surface (which is not the case in the model after s_{in} reaches s_{melt}). Both the power and the energy for melting and icing agrees very well with the experimental data.

4.7. Conclusions

In this chapter, the mathematical formulation for an ice storage has been validated with experimental data from chapter 2. Validation of the model has been conducted using a large number of simulated cases, including difference testing sequences, heat exchanger types, number of heat exchangers and mass flow rates. The parameters of the model were constant for all cases, without any specific tuning per case of heat exchanger type. The main conclusions of this chapter are:

- The sensible heating test is very well predicted by both FP and CM heat exchanger models. The normalized averaged energy differences Q_{Nr}^{rms} are between 2 % and 6 % depending on mass flow and heat exchanger type. The normalized averaged power \dot{Q}_{Nr}^{rms} shows differences between 4 % and 7 % for FP. For CM and 2000 l/h, differences of 5 % were observed. For CM and 1000 l/h, higher differences up to 13 % were observed. However, this was thought to be related to the non-steady conditions at the beginning of the test and not to the mass flow rate influence.
- The sensible cooling test is not as well predicted as the heating case due to the differences between simulations and experiments around 4 °C, where the maximum density of water is found. Differences in this region lead to higher differences in power predictions, with averaged \dot{Q}_{Nr}^{rms} between 7 % to 11 % depending on mass flow and heat exchanger type. Nevertheless, differences in energy predictions were found to be good with Q_{Nr}^{rms} between 2 % to 5 %.
- The validation of the icing test was found to be very challenging for the CM and specific functions to mode the ice constraintment were necessary to handle different distances between tubes in two spatial direction. In FP these functions are not necessary due to the unidirectional growing of the ice in the heat exchanger plates. Energy differences and thus ice fraction evolution were found to be satisfactory with averaged differences of Q_{Nr}^{rms} between 2 % to 6 %. However, power predictions had larger errors with difference of \dot{Q}_{Nr}^{rms} around 22 to 25 % for FP and around 20 % for CM.
- The validation of the melting process lead to similar results to the icing test. Averaged Q_{Nr}^{rms} were between 5 % to 9 % for FP and between 3 % to 6 % for CM. Averaged differences in power were between 15 % to 19 % for FP and between 17 % to 25 % for CM depending on mass flow rate.

5. Solar-ice system simulations

The aim of the present chapter is to analyze flat plates (FP) and capillary mats (CM) heat exchangers for solar-ice systems. The optimum heat exchanger area needed in the ice storage is based on energetic transient system simulations and on cost indicators. In section 5.1 the methodology followed to solve the system of equations is described, in section 5.2 the hydraulics of the system are presented. In section 5.5, the results of the simulation from an energetic point of view are presented and the cost of the systems are discussed in section 5.6.

5.1. Methodology

Dynamic system simulations are used in order to assess the heat exchanger area and heat exchanger type on a system level. The simulations have been conducted with the simulation environment TRNSYS-17 (Klein et al., 2010). The basic components to model a solar-ice system are: collectors, heat pump, ice storage, sensible thermal storage, building, climate and control. The ice storage model has been

explained in chapter 3. The formulation of the remaining component models were provided in Carbonell et al. (2016c), where a complete solar-ice system based on a de-icing concept was validated with monitored data on one pilot plant.

The time step of yearly simulations is set to 120 seconds. As a verification process several systematic checks are done for all simulations. Heat balances are checked in all individual components, hydraulic loops and also from the system perspective. The convergence criteria from TRNSYS is set to $5e-4$, which allows to achieve heat imbalances always below 1.% in respect to the total demand. Iteration problems are also checked for all simulations and are always below 10 time steps per year simulated. In most cases iteration problems are in the order of 1 - 5 per year.

5.2. Hydraulic scheme of the simulated system

The hydraulic scheme of the complete solar-ice heating system is shown in Fig. 5.1. The main components of the heating system are the collector field, the combi-storage, the heat pump and the ice storage.

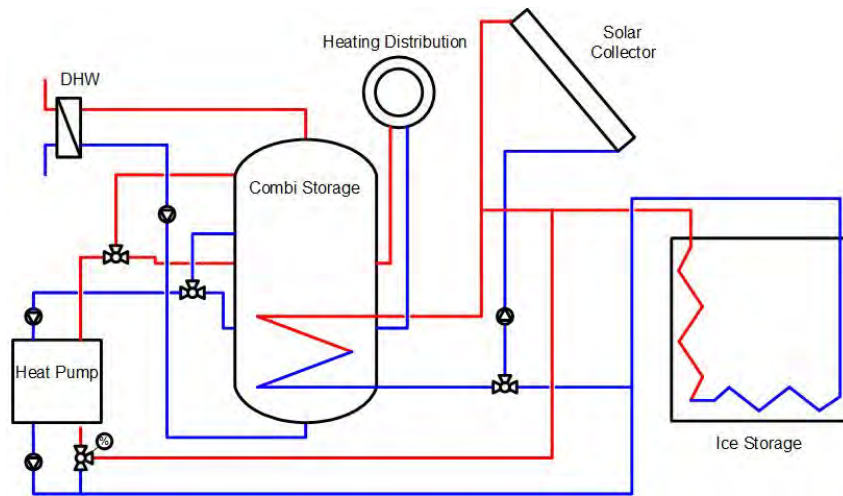


Figure 5.1: Simplified hydraulic scheme of the analysed heating system.

The main energy source of the system is the solar irradiation. Some additional energy is extracted from the air, especially when uncovered collectors are used ⁴. Part of the total solar irradiation is transformed by the collectors to useful heat for the system. This energy is transferred, either to the heat pump, to the ice storage or to the combi-storage. When the heat pump is running, two operation modes are possible, depending on whether the collectors are able to provide energy or not: i) the heat pump uses the solar energy directly in a series operation mode or ii) the heat pump uses the ice storage as its source. With the hydraulic set-up proposed here, when the heat pump is running with solar energy as a source, the mass flow from the solar collector field is divided: one part goes to the heat pump and the other part goes to the ice storage. The split of the mass flow is basically controlled by each pump, i.e. solar and heat pump evaporator. If these mass flows are not equal, its difference will flow to the ice storage. On these conditions, if more energy is available from the collector field than is needed by the heat pump, the ice storage is also loaded while the heat pump is running. On the contrary, if the collector output is lower than the heat pump needs, both, the ice storage and the collector field are used to provide heat to the evaporator of the heat pump. If none of these heat sources are available, which means that the ice storage is full of ice and the solar radiation and the ambient temperature are very low, the temperature of the heat pump evaporator drops below the minimum allowed value and the heat pump stops. In this case, a direct electric back-up is used. A method to reduce the need of back-up in winter times is to send the whole mass flow from the collector to the heat pump. This can be done with this hydraulic scheme by setting the mass flow from the collector equal to the one demanded by the heat pump. This tends to reduce the working temperature of the circuit and as a consequence decrease the heat pump COP. However, it reduces the times where the ice storage is used and thus the times where the direct electric back-up is used. Usually, reduction of the time use of the back-up is compensated by the loss of heat pump performance.

⁴All results shown in this project are obtained with selective uncovered collectors.

5.3. System control

The system part on the secondary side of the heat pump, i.e. the heating distribution and the DHW-preparation, and the heat pump itself are mostly controlled in a standard way. The brine cycle on the primary side, on the other hand, needs some special operation modes to decide how to use the solar heat. The backup needs to be controlled too, such that it runs when there is a heating demand in the building and the ice storage is fully iced (no source available for the heat pump). Further, season-based priorities regarding the use of the solar heat are implemented. The solar-ice system has a global control with three main priorities in the following hierarchy:

1. Use of direct solar heat to provide the space heat to the building without switching on the heat pump.
2. Switching on the heat pump when not enough energy is available in the combi-storage in order to provide the space heat. When heat pump is on, solar energy is prioritized as energy source.
3. Use solar heat to load the combi-storage and ice storage when the heat pump is off. Loading the combi-store is usually referred as direct solar heat. Direct solar heat is usually prioritized in spring, summer and autumn, but in winter the loading of the ice storage is prioritized.

The control has to cope with the fact that the ice storage is a cold sink for a long time during the year. Unless a logic is implemented, that switches to loading of the combi-storage when appropriate, the ice storage would be loaded predominantly. The control mode that actively stops the loading of the cold storage and tries to divert the solar heat on a higher temperature level to the combi-storage is called warm storage priority. If the warm storage priority is not active, the control mode cold storage priority is on, which loads the ice storage. For small sized systems is usually a better option to use the a cold storage priority in winter in order to avoid the time when the direct electric back-up is needed. As soon as there is no risk to fully ice the storage, then warm storage priority should be used.

5.4. Performance indicators

The main performance indicator for the systems is the System Performance Factor calculated as described in Malenkovic et al. (2012):

$$SPF_{SHP+} = \frac{Q_{DHW} + Q_{SH}}{P_{el,T}} = \frac{Q_D}{P_{el,T}} \quad (44)$$

Q is the yearly heat load energy and $P_{el,T}$ the total yearly electric energy consumption. The subscripts SHP , DHW , SH and D stand for solar and heat pump, domestic hot water, space heating, and total demand respectively.

The total electricity consumption is calculated as:

$$P_{el,T} = P_{el,pu} + P_{el,hp} + P_{el,cu} + P_{el,aux} + P_{el,pen} \quad (45)$$

where the subscripts pu , hp , cu , aux and pen refer to circulation pumps, heat pump, control unit, auxiliary and penalties respectively. The symbol "+" in the $SHP+$ from Eq. 44 refers to the consideration of the heat distribution circulating pump in the electricity consumption. Therefore, the system performance indicator used in this work includes all circulation pumps of the system and also all thermal losses/gains from storages and piping. Penalties for not providing the heating demand at the desired comfort temperature are calculated according to Haller et al. (2012). $P_{el,aux}$ is the energy used from the direct electric back-up system.

5.5. System energetic performance with varying heat exchanger type and area

Dynamic yearly system simulations have been carried out for different heat exchanger areas and for two types of heat exchangers, capillary mats (CM) and flat plates with stainless steel (FP-SS). Simulations have been performed for ice storage volumes of 3 m³, 4 m³ and 5 m³ and collector areas of 15 m², 20 m² and 25 m².

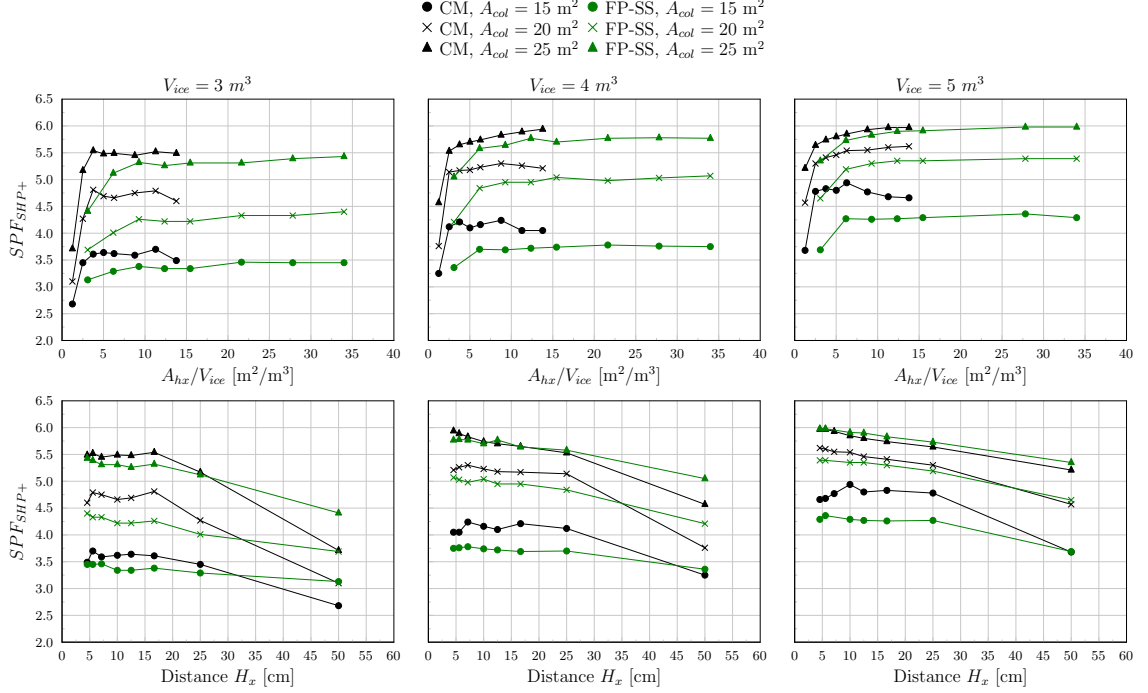


Figure 5.2: Yearly system performance as function of (top) heat exchanger area divided by ice storage volume and (bottom) distance between heat exchangers for three ice storage volumes of (left) 2 m^3 , (mid) 4 m^3 and (right) 5 m^3 .

Results for the $\text{SPF}_{\text{SHP}+}$ are shown in Fig. 5.2 as a function of the ratio between the heat exchanger area and the ice storage volume and as a function of the distance between heat exchangers. The same distances between heat exchangers are used both for CM and FP-SS. However, since FP-SS have almost twice the area⁵ compared to CM, results for FP-SS are shifted towards higher A_{hx}/V_{ice} . Both heat exchanger types are able to provide very high $\text{SPF}_{\text{SHP}+}$, up to 6 for the sizes used in these simulations. System performances above 4 (as GSHP) are always achieved if the collector area is $\geq 20 \text{ m}^2$. For collector areas in the order of 15 m^2 , an $\text{SPF}_{\text{SHP}+}$ above 4 can be achieved with CM and $V_{ice} = 4 \text{ m}^3$ and with FP-SS if $V_{ice} = 5 \text{ m}^3$. Using 15 m^2 and 5 m^3 both heat exchangers are able to provide $\text{SPF}_{\text{SHP}+}$ above 4.

Very high system performances, in the order of 5 to 6, can be achieved with different component sizes. These results confirm the flexibility of the system concept, i.e. the same $\text{SPF}_{\text{SHP}+}$ can be obtained using different configurations of ice storage volume and collector area. This allows to achieve a specific $\text{SPF}_{\text{SHP}+}$ even if there are restrictions such as small cellar capacity or available roof area. However, there is a limit on the lowest size of the collector field since the solar-ice system is based purely on solar energy as heat source. The system flexibility of solar-ice systems was discussed in Carbonell et al. (2014). Of particular interest are results with 4 m^3 , since this storage volume could fit in many cellars of single family homes using two separated storages of 2 m^3 allowing to achieve an $\text{SPF}_{\text{SHP}+} \geq 5$ with collector areas of 20 m^2 .

Regarding the heat exchanger type, it seems clear that the $\text{SPF}_{\text{SHP}+}$ is usually higher for CM compared to FP-SS except for large distance between heat exchangers, e.g. $> 25 \text{ cm}$ for $V_{ice} = 3 \text{ m}^3$. System performances for CM when distances between heat exchangers are small are higher because of the better heat transfer coefficient when icing at high ice fractions. The $\text{SPF}_{\text{SHP}+}$ of CM is worse than that of FP-SS for cases where the distance between heat exchangers is way higher than that between the tubes in one CM. One can imagine a CM like a FP with empty spaces between tubes. Let's imagine the limit case where all tubes in one CM are in contact to each other. Under those circumstance CM would be worst than FP because of the higher resistance of polypropylene compared to stainless steel. When ice fills all the gaps between tubes, there is the added limitation that not all area is used due to the spaces between tubes.

⁵The two faces of the flat plate heat exchanger are considered as heat exchanger area.

Differences between FP-SS and CM are more prominent for low collector areas and low ice storage volumes. Results for 25 m² and 5 m³ tend to an asymptotic solution where differences between CM and FP-SS are negligible. In those situation the direct electric back-up is not used because the system components are sized largely enough such that not all the latent heat capacity of the storage is necessary. The direct electric back-up is shown in Fig. 5.3 as a function of the ratio between A_{hx} and V_{ice} . Clearly,

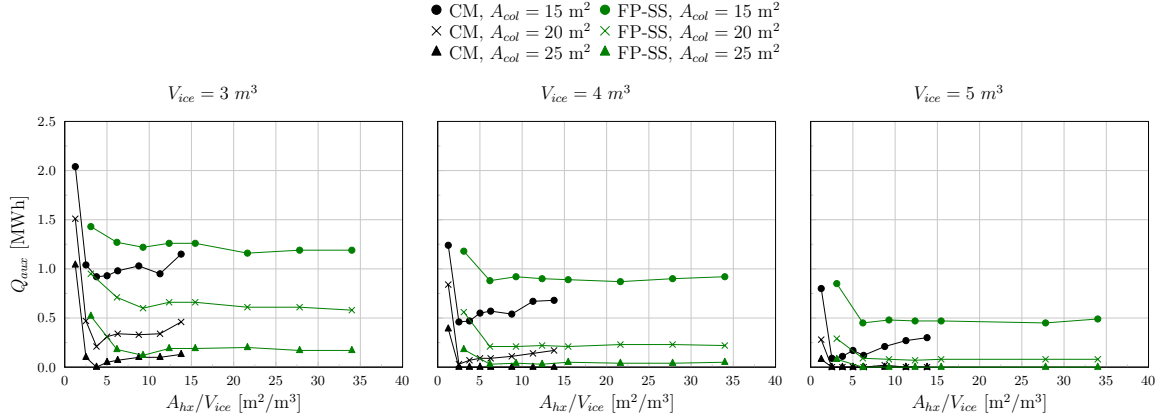


Figure 5.3: Direct electric back-up as a function of heat exchanger area divided by ice storage volume for three ice storage volumes of (left) 2 m³, (mid) 4 m³ and (right) 5 m³.

the increase of collector area and storage volume decrease the use of the direct electric back-up. The direct electric back-up is used exclusively in winter, when the ice storage is full (maximum ice fraction of 80 % has been assumed) and there is not enough solar energy to provide the heat for the evaporator of the heat pump. The use of the electric back-up is the dominant factor that influences the SPF_{SHP+} . Once the electric back-up is avoided, the system performance is quite independent of the heat exchanger area and less dependent on the collector area or ice storage volume. A SPF_{SHP+} value below 5.5 is usually indicates the need of direct electric back-up.

In order to establish the optimum heat exchanger area in terms of SPF_{SHP+} it is of importance to investigate the maximum ice fraction achieved, as shown in Fig. 5.4. If the heat exchanger area is too low for the specific system design, some latent heat may not be used because the heat transfer coefficient will be too low at the maximum ice thickness achieved. This would lead to a situation where the heat pump would not be able to extract enough power from the ice storage while there is still liquid water present. For CM the maximum ice fraction of 80 % is reached approximately for ratios of A_{hx}/V_{ice} of 5-10 m²/m³. For FP the maximum ice fraction is reached at higher ratios of 10-15 m²/m³. For both cases these ratios correspond to a distance of around 7-12 cm between heat exchangers.

For some configurations, it is not possible to use all latent heat of the storage. For example for $V_{ice} = 5$ m³ and $A_{col} = 25$ m², none of the heat exchangers setup can achieve an ice fraction of 80 %. This indicates that the system is oversized and either the ice storage or the collector area could be decreased and the system performance would not be penalized much. For example in Fig. 5.2 the SPF_{SHP+} of $A_{col} = 25$ m² is almost the same if the storage volume is 4 m³ or 5 m³. Another way to make use of the latent heat and also to increase the SPF_{SHP+} would be to give more priority to the warm storage loading.

5.6. Cost analyses of solar-ice systems

In sections above the system performance in terms of energy have been provided. In this section, costs are taken into consideration in order to further evaluate different system designs. For all analyzed heating systems, investment costs and heat generation costs for prices of the Swiss energy market in 2016/2017 are calculated. The comparison of costs is used to find the optimum heat exchanger area considering both energetic system performance and a good value for the money.

The investment costs of the solar-ice systems are based on real costs that were gathered from several sources. Some data was obtained from the realization of two demonstration projects of solar-ice systems in Rapperswil-Jona, Switzerland. The data from the solar part was obtained from the SFOE project

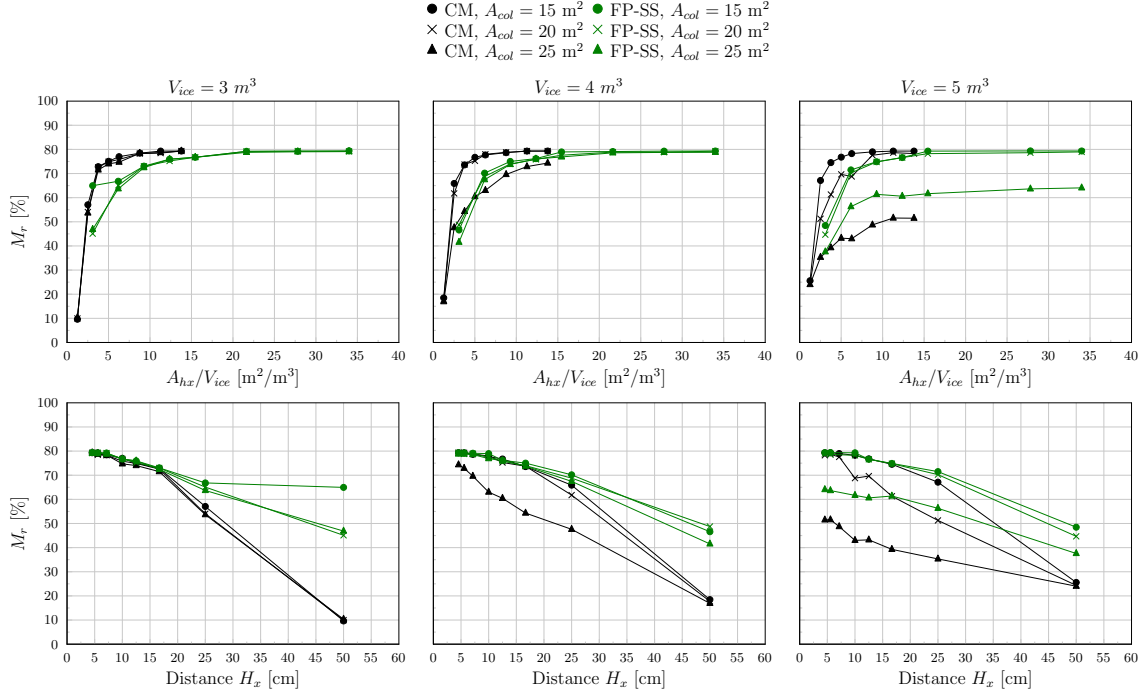


Figure 5.4: Maximum yearly mass ice fraction as a function of (top) heat exchanger area divided by ice storage volume and (bottom) distance between heat exchangers for three ice storage volumes of (left) 2 m^3 , (mid) 4 m^3 and (right) 5 m^3 .

ReSoTech (Philippen et al., 2016). This data was used to derive cost functions per component. The cost functions are then used to calculate investment costs per specific system size simulated.

A ground source heat pump system is used as a reference to compare the system performance in terms of energetic efficiency and cost. Using a borehole length of 130 m for a single family house in the region of Zurich an $\text{SPF}_{\text{SHP}+}$ around 4 is expected. Investment costs for GSHP are based on two offers of Swiss sellers for a GSHP system that supplies heat to a single family house (Causi, 2010). The cost functions were derived from average costs of the two offers. All received cost functions were verified by a Swiss seller of heating systems in terms that they represent actual average market prices.

For each system the present value of costs and the annuity are calculated following the methodology of VDI (2012) and Bangerter (1985) with some simplifications. Main assumptions for the economic analysis are given in Table 5.1 and details for the calculation method were provided in Philippen et al. (2015). The electricity prices are taken from the price list of a regional Swiss utility and represent typical prices for small customers. The increase of electricity cost is based on the assessment of this utility.

Table 5.1: Assumptions for calculation of heat generation costs.

Rate of interest	2.0 % p.a.
Analysis period	25 years
Yearly Maintenance	0.25 % of investment costs
Lifetime ice storage casing and bore holes	50 years
Electricity costs (incl. VAT)	Fixed costs: 171 Fr. per year Variable costs: 0.13 Fr. per kWh
Increase of electricity costs	1. % p.a.

5.6.1 Heat generation cost

The system performance (top) and the heat generation cost (bottom) are shown in Fig. 5.5 as a function of the ratio A_{hx}/V_{ice} for CM and FP-SS for three collector areas and storage volumes analyzed in sections above. The SPF_{SHP+} is repeated here in order to compare directly graphs of SPF_{SHP+} and cost. The reference values for the GSHP system are included in all graphs. The objective is to achieve a solar-ice system with same or higher performance than GSHP with same or lower cost. Therefore, the focus is on solar-ice systems with an $SPF_{SHP+} \geq 4$. The only configurations where this target is not met are the systems with $A_c = 15 \text{ m}^2$ and $V_{ice} = 3 \text{ m}^3$. For $V_{ice} = 5 \text{ m}^3$ all systems performance are above 4 and for $V_{ice} = 4 \text{ m}^3$ only performance of the case with 15 m^2 and FP-SS are below 4.

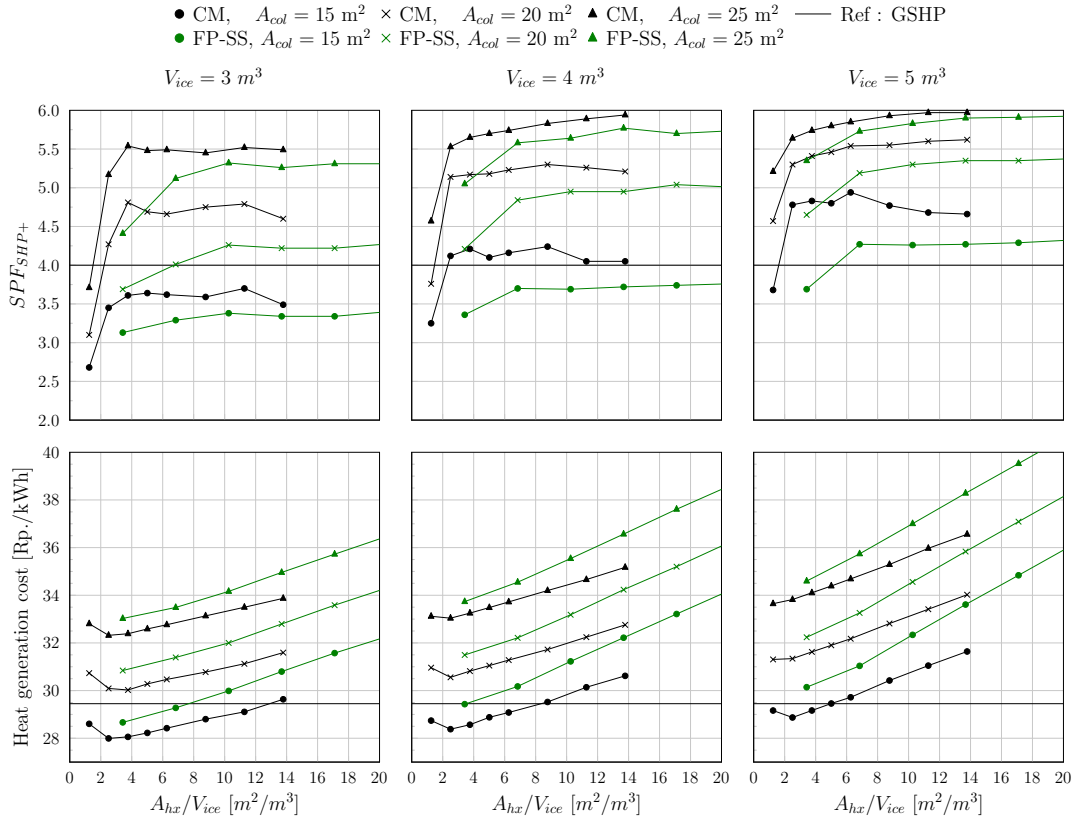


Figure 5.5: System performance (up) and heat generation cost (bottom) as function of heat exchanger area divided by ice storage volume. Three ice storage volumes are used: (left) 3 m^3 , (mid) 4 m^3 and (right) 6 m^3 .

The heat generation cost are shown in bottom part of Fig. 5.5. There are two configurations where the $SPF_{SHP+} \geq 4$ and the heat cost are below that from the GSHP. Both configurations are using CM and 15 m^2 , for 4 and 5 m^3 storage volumes. These two system set-ups are of particular interest due to the low cost and high efficiency. All systems using FP which performance is above 4 have higher heat generation cost compared to that of the GSHP. It should be noted that cost calculations are based on many assumptions that affect significantly the results. Therefore, heat generation cost should be seen as orders of magnitude. Unfortunately, the error band is not easy to assess.

Using the cost function alone is not a good approach to decide the heat exchanger area. For example in FP the lowest area seems to provide the cheapest system even when the energetic performance is relatively low. Besides the cost function, the SPF_{SHP+} and also the maximum ice fraction achieved as shown in Fig. 5.4 should be used. Considering all these values it seems that the optimum heat exchanger area is in the order of $4\text{-}5 \text{ m}^2/\text{m}^3$ for CM and around $10\text{-}14 \text{ m}^2/\text{m}^3$ for FP-SS. Those ratios correspond approximately to 12-17 cm for both heat exchangers.

The heat generation cost along with the system performance are shown in Fig. 5.6 as a function of the

collector area. The heat generation cost increases linearly with collector area. The minimum of the function can not be observed with the simulated collector area. From this plot and the sizes chosen, it seems that is a better option to reduce the collector area and increase the ice storage volume. For example CM with $V_{ice} = 5 \text{ m}^3$ and 15 m^2 has higher SPF_{SHP+} and lower cost compared to CM with 20 m^2 of collector area. The cost of the selective uncovered collectors are based on a single manufacturer. Considering the cost of other manufacturers could change this trend.

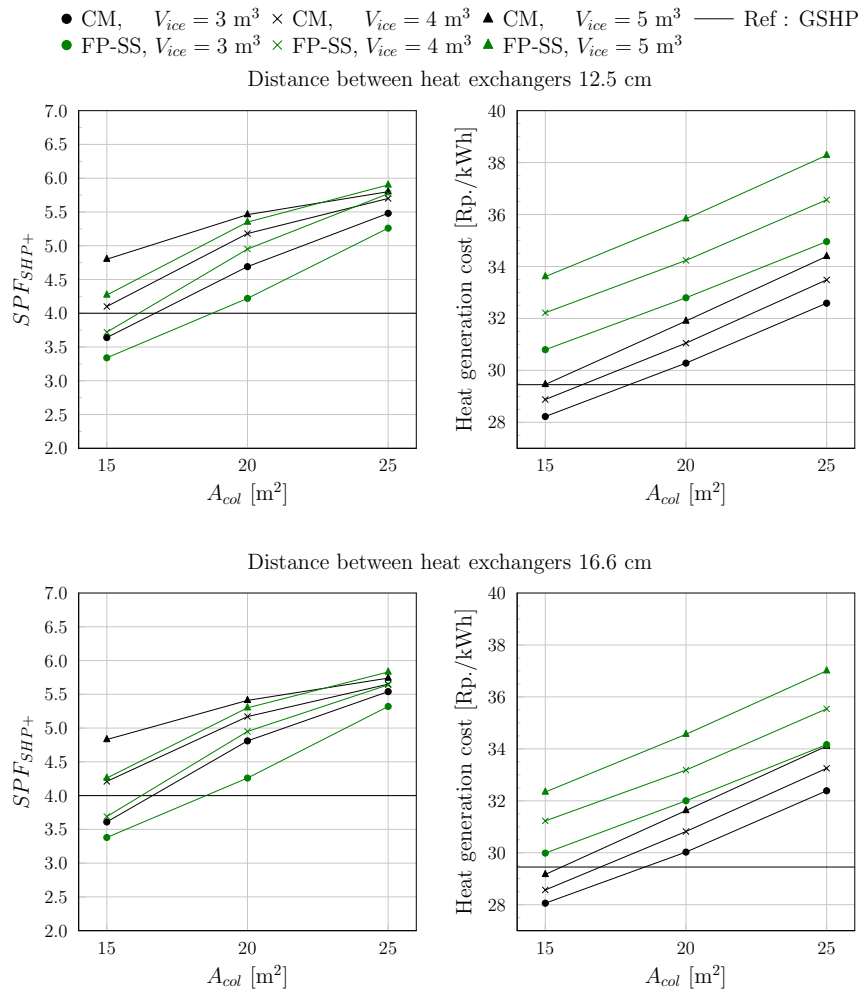


Figure 5.6: System performance (left) and heat generation cost (right) as function of the collector area and ice storage volume for a distance of 12.5 cm (up) and 16.6 cm (bottom) between heat exchangers.

5.6.2 Installation cost

Installation costs for an ice storage volume of 4 m^3 with a distance of 16.6 cm between each heat exchanger and a collector area of 15 m^2 are shown in Fig. 5.7. As a reference, the installation cost of GSHP are calculated as 53'048 Fr. The installation cost using CM heat exchangers, with a total amount of 48'460 Fr., is 8.6 % lower than that of the GSHP and the case with FP-SS with 52'980 Fr. is almost the same.

An example of the calculation cost for the CM is shown in Table 5.2. The installation cost using FP-SS only differ on the heat exchangers used in the ice storage. The cost of the ice storage for FP-SS is given in Table 5.3.

The conclusions of the cost-energetic study of chapter 5 are provided at the end of the following chapter 6.

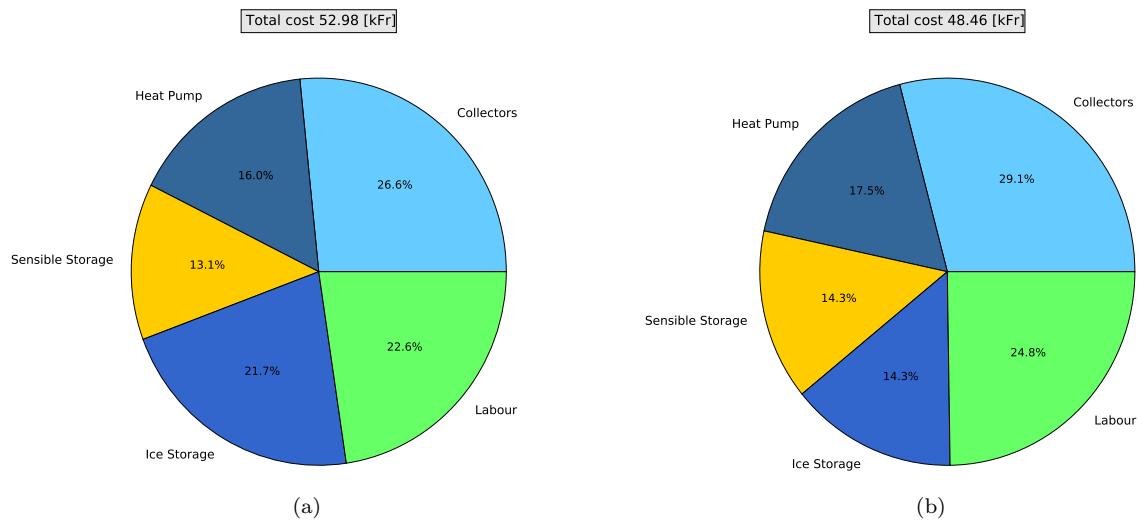


Figure 5.7: Shares of installation cost for an ice storage of 4 m³ with a distance of 15 cm between heat exchangers and a collector area of 15 m² for (a) FP-SS (b) CM.

Table 5.2: System and Heat generation costs for an ice storage of 4 m³, a distance of 16.6 cm between heat exchangers and a collector area of 15 m² using CM heat exchangers (all values incl. 8% VAT).

Component	Component	Costs [Fr.]	Total Costs [Fr.]
Ice Storage	Stainless steel storage with insulation	5288	6953 (14%)
	CM heat exchangers	816	
	Piping	248	
	Mounting heat exchangers and pipes	600	
	Total Ice storage		
Collectors	Selective uncovered	7935	14098 (29%)
	Hydraulic roof to cellar (solar)	6163	
	Total Collectors		
Heat pump	Heat pump unit	7904	8490 (18%)
	Hydraulic heat pump to combi-storage	186	
	Insulation pipes	400	
	Total Heat pump		
Thermal storages	Basic costs storage	6915	6915 (14%)
	Total combi-storage		
Labor cost	Installation	8000	12000 (25%)
	Third parties + Divers	4000	
	Total Labor costs		
Total Investment Cost			48456

Table 5.3: Ice storage cost for a volume of 4 m³ and a distance of 16.6 cm between each FP-SS heat exchanger (all values incl. 8% VAT).

Component	Component	Costs [Fr.]	Total Costs [Fr.]
Ice Storage	Stainless steel storage with insulation	5288	11478 (22%)
	FP-SS heat exchangers	4021	
	Piping	248	
	Mounting heat exchangers and pipes	1920	
	Total Ice storage		

6. Conclusions

In this research study a experimental and numerical analyses of different heat exchangers, i.e. capillary mats, flat plates and coils were carried out. An ice storage model able to cope with all analyzed heat exchangers has been developed and validated with the experimental data. The energetic simulations of the complete solar-ice system has been used to find the optimum heat exchanger area for the most promising heat exchangers in terms of energetic efficiency and heat generation cost.

In chapter 2, results of several heat exchangers have been analyzed, including capillary mats with different designs made of polypropylene, flat plates made of stainless steel and polypropylene and a custom-made polypropylene coil. The area analyzed has been modified for each heat exchanger and all tests have been performed using two different mass flow rates. In total, ten possibilities have been experimentally evaluated for several test sequences including sensible heating and cooling, icing, melting and cycling. The main conclusions of this experimental study can be summarized as:

- Very high ice fraction can be reached with all heat exchangers and mass flows.
- The casing did not show any damage under high ice fraction conditions. This means that designing an ice storages able to reach 95% ice fraction or higher should be safe.
- All heat exchangers showed to be reliable and robust under the test conditions. Long term tests were not carried out.
- Flat plates made of stainless steel are better suited compared to capillary mats or coils for sensible heating and cooling and for melting processes.
- Capillary mats or coils are better suited compared to flat plates for the icing process due to the strong decrease of performance that flat plates suffer when ice grows.
- Flat plates made of polypropylene have shown the worst thermal performance of all tested heat exchangers.
- Coil heat exchangers made of polypropylene for small ice storages were difficult to design and build. Therefore, it does not seem to be the a promising solution for low ice storage volume ($< 5 \text{ m}^3$).

From all the heat exchangers analyzed experimentally, capillary mats made of polypropylene and flat plates made of stainless steel are the most promising solutions.

In chapter 3 the mathematical model for an ice storage has been presented. The validation of the ice storage has been presented in chapter 4 using the experimental data from chapter 2. The main conclusions of the validation procedure are:

- The sensible heating test is very well predicted by both FP and CM heat exchanger models. The normalized averaged energy differences $Q_{N_r}^{rms}$ are between 2 % and 6 % depending on mass flow and heat exchanger type. The normalized averaged power $\dot{Q}_{N_r}^{rms}$ shows differences between 4 % and 7 % for FP. For CM and 1000 l/h, higher differences up to 16 % were observed. However, this was thought to be related to the non-steady conditions at the beginning of the test and not to the mass flow rate influence.
- The sensible cooling test is not as well predicted as the heating case due to the differences between simulations and experiments around 4 °C, where the maximum density of water is found. Differences in this region lead to higher differences in power predictions, with averaged $\dot{Q}_{N_r}^{rms}$ between 7 % to 10 % depending on mass flow and heat exchanger type. Nevertheless, differences in energy predictions were found to be good with $Q_{N_r}^{rms}$ between 2 % to 5 %.
- The validation of the icing test was found to be very challenging for the CM and specific functions to mode the ice constraintment were necessary to handle different distances between tubes in two spatial direction. The use of these functions were found to be satisfactory, since results using them lead to slightly better results for CM compared to FP. In FP these functions are not necessary due to the unidirectional growing of the ice in the heat exchanger plates. Energy differences and thus ice fraction evolution were found to be satisfactory with averaged differences of $Q_{N_r}^{rms}$ between 5 % to 6 %. However, power predictions had larger errors with difference of $\dot{Q}_{N_r}^{rms}$ around 18 to 20 % for CM and between 25 to 30 % for FP depending on mass flow rate.

- The validation of the melting process lead to similar results to the icing test. Averaged Q_{Nr}^{rms} were between 4 % to 6 % for FP and between 9 % to 10 % for CM. Averaged differences in power were around 20 to 23 % for both FP and CM.

In general results are satisfactory considering the large number of simulated cases, including difference testing sequences, the use of different heat exchanger types, number of heat exchangers and the use of different mass flow rates. Moreover, the parameters of the model were constant for all cases, without any specific tuning per case of heat exchanger type. Therefore, results should be compared with caution to other publications were only one case was simulated. Tuning each case could reduce the differences significantly.

In chapter 5 the complete solar-ice system has been simulated with the validated ice storage model from chapter 3. From the system simulations the following conclusions can be drawn:

- A solar-ice system with ice storages volumes between 0.3 to 0.5 m³ per MWh of yearly heating demand, and collector areas between 1.6 to 2.6 m²/MWh can reach an SPF_{SHP+} in the range of 3.5 to 6 in Zurich for a single family home with 9.5 MWh total (SH + DWH) heating demand.
- Besides the sizes of the ice storage and collector field areas, the most relevant factor affecting the SPF_{SHP+} is the electric back-up necessary to run the system in winter periods. Control strategies should be focus on reducing it as a first target. When the electric back up is minimized, control strategies should focus on the maximization of direct solar heat.
- Solar-ice systems can reach very high SPF_{SHP+} regardless of the heat exchanger type, but when the heat generation cost are included, only capillary mats are able to provide higher SPF_{SHP+} compared to GSHP at a lower cost. However, the heat exchanger area needs to be well design to reach these targets. An ice storage volume of 0.5 m³/MWh with capillary mats and 1.6 m²/MWh of collector area can reach heat generation costs of 29 Rp./kWh (0.5 Rp./kWh below the GSHP) with an SPF_{SHP+} of 4.8, which represents an increase of SPF_{SHP+} of 20 % respect to GHSP.
- Considering both energetic and economic indicators, capillary mats are found to be the most promising solutions for solar-ice applications when compared to the other heat exchangers analyzed along the project. Nevertheless, other factors could be used to choose other heat exchangers. For example, one may choose flat plates made of stainless steel instead of capillary mats due to the robustness of the heat exchanger, with a life time guarantee of 25 years. Another reason to select stainless steel heat exchangers can be that they are oxygen tight and therefore an expensive stainless steel piping system in the collector loop can be avoided. The cost of the stainless steel piping system needed when plastic capillary mats are used could overcome the more expensive heat exchangers. However, this has not been considered in the cost calculations, where the piping system was the same for all heat exchangers. Moreover, one should keep in mind that cost calculations have a large degree of uncertainty.
- A strategy to reduce the direct electric back up is to reduce the working temperature of the primary brine loop connecting the solar collectors, ice storage and heat pump. For cost economic systems, priority should be set to use the collectors as primary source for the heat pump in winter, even that the working temperature decreases well below 0 °C. For those circumstances, the use of the ice storage would increase the instantaneous COP of the heat pump. However, it would increase the operating times of the direct electric back-up. The better instantaneous heat pump COP can hardly compensate the higher use of the electric back-up at a COP of 1. For oversized systems, where the back-up is seldomly used in winter, the control should give priority to the combi-storage. Those systems will have roughly an SPF_{SHP+} in the order of 5.5 or above.

Dissemination

Project results have been presented in the two international conferences and one national. Moreover, the mathematical formulation and validation of the ice storage model using capillary mats heat exchangers have been submitted to a peer-reviewed journal.

Conference proceedings

- Carbonell, D., Granzotto, M., Battaglia, M., Philippen, D. and Haller, M. Y. Experimental investigations of heat exchangers in ice storages for combined solar and heat pump systems. In *11th ISES EuroSun Conference*, Palma (Mallorca), Spain, 2016. International Solar Energy Society (ISES).
- Philippen, D., Carbonell, D., Battaglia and Haller, M. Y. Eisspeicher in der Forschung und im praktischen Einsatz. In *23. Tagung des BFE-Forschungsprogramm „Wärmepumpen und Kälte“*, HTI Burgdorf, Schweiz, 2017. Bundesamt für Energie BFE.
- Carbonell, D., Philippen, D., Battaglia, M. and Haller, M. Y. Cost energetic analyses of ice storage heat exchangers in solar-ice systems. In *International Conference on Solar Heating and Cooling for Buildings and Industry*, Abu Dhabi, United Arab Emirates, 2017. IEA Solar Heating and Cooling Program.

Oral presentations were held in Mallorca (Spain) and Burgdorf (Switzerland). A poster will be presented in Abu Dhabi (United Arab Emirates).

Journal paper with contributions from this project

Project results regarding the modelling of the ice storage have been submitted to a peer-reviewed journal.

- Carbonell, D., Battaglia, M., Philippen, D., and Haller, M. Y. Numerical and experimental evaluation of ice storages with ice on capillary mat heat exchangers for solar-ice systems. *International Journal of Refrigeration (submitted)*, 2017.

References

- ASHRAE (2007). *Handbook : HVAC Applications*. American Society of Heating, Refrigerating and Air-Conditioning Engineers, Inc.
- Bangerter, H. (1985). *Baukostendaten 1985, Rentenbarwert- und wahre Mittelwertfaktoren*. Band 1.
- Bédécarrats, J.-P., David, T., and Castaing-Lasvignottes, J. (2010). Ice slurry production using super-cooling phenomenon. *International Journal of Refrigeration*, 33(1):196–204.
- Carbonell, D., Battaglia, M., Philippen, D., and Haller., M. Y. (2017). Numerical and experimental evaluation of ice storages with ice on capillary mat heat exchangers for solar-ice systems. *International Journal of Refrigeration (submitted)*.
- Carbonell, D., Granzotto, M., Battaglia, M., Philippen, D., and Haller, M. Y. (2016a). Experimental investigations of heat exchangers in ice storages for combined solar and heat pump systems. In *11th ISES EuroSun Conference*, Palma (Mallorca), Spain. International Solar Energy Society (ISES).
- Carbonell, D., Philippen, D., Granzotto, M., and Haller, M. Y. (2016b). Simulation of a solar-ice system for heating applications. System validation with one-year of monitoring data. *Energy and Buildings*, 127(0):846 – 858.
- Carbonell, D., Philippen, D., Granzotto, M., Haller, M. Y., and Frank, E. (2014). Simulation of combined solar thermal, heat pump, ice storage and waste water heat recovery systems. Design criteria and parametric studies. In *Proceedings of EuroSun*, Aix les Bains, France. International Solar Energy Society (ISES).

- Carbonell, D., Philippen, D., and Haller, M. Y. (2016c). Modeling of an ice storage buried in the ground for solar heating applications. Validations with one year of monitored data from a pilot plant. *Solar Energy*, 125:398–414.
- Carbonell, D., Philippen, D., Haller, M. Y., and Frank, E. (2015). Modeling of an ice storage based on a de-icing concept for solar heating applications. *Solar Energy*, 121:2–16.
- Causi, A. (2010). *Simulation und Vergleich von Wärmepumpen-Heizungen welche Erdsonden respektive Eisspeicher und Solarkollektoren als Wärmequellen nutzen*. Bachelor Thesis, Hochschule für Technik Rapperswil, Institut für Solartechnik SPF, Switzerland.
- Churchill, S. W. (2002). *Free convection around immersed bodies*, pages 2.5.7–1–2.5.7–31. *Heat Exchanger Design Handbook*, Hewitt G.F., Washington: Hemisphere Publishing Corporation.
- Cooper, A. and Usher, J. D. (2002). *Plate heat exchangers*, pages 3.7.5–1. *Heat Exchanger Design Handbook*, Hewitt G.F., Washington: Hemisphere Publishing Corporation.
- Drees, K. H. and Braun, J. E. (1995). Modeling of area-constrained ice storage tanks. *HVAC&R Research*, 1(2):143–158.
- European Technology Platform on Renewable Heating and Cooling (2013). Strategic Research and Innovation Agenda for Renewable Heating & Cooling. Technical report, International Energy Agency IEA.
- European Commission (2012). Energy roadmap 2050. Technical report, European Commission.
- Haller, M. Y., Dott, R., Ruschenburg, J., Ochs, F., and Bony, J. (2012). The reference framework for system simulation of the IEA SHC Task44/HPP Annex 38: Part A : General simulation boundary conditions. Technical Report IEA-SHC Task44 Subtask C.
- Incropera, F. P., Dewitt, D. P., Bergman, T. L., and Lavine, A. S. (2006). *Fundamentals of Heat and Mass Transfer*. John Wiley & Sons, 6th edition.
- Ismail, K. A. R., Quispe, O., and Henríquez, J. R. (1999). A numerical and experimental study on a parallel plate ice bank. *Applied Thermal Engineering*, 19(2):163–193.
- Jekel, T. B., Mitchell, J. W., and Klein, S. A. (1993). Modeling of ice storage tanks. *ASHRAE Transactions*, 99(1):1016–1024.
- Kauffeld, M., Kawaji, M., and Egolf, P. W. (2005). *Handbook on Ice Slurries - Fundamentals and Engineering*. International Institute of Refrigeration (IIR), 1st edition.
- Klein et al. (2010). Trnsys 17: A transient system simulation program, solar energy laboratory. Technical report, University of Wisconsin, Madison, USA, <http://sel.me.wisc.edu/trnsys>.
- Koller, T., Spindler, K., and Müller-Steinhagen, H. (2012). Experimental and theoretical investigations of solidification and melting of ice for the design and operation of an ice store. *International Journal of Refrigeration*, 35(1):1253–1265.
- Malenkovic, I., Eicher, S., and Bony, J. (2012). *Definition of main system boundaries and performance figures for reporting on SHP systems*. IEA-SHC Task44 Subtask B.
- Morgan, V. T. (1975). The overall convective heat transfer from smooth circular cylinders. In *Advances in Heat Transfer*, volume 11, pages 199–264, New York. Academic Press Inc.
- Mouneer, T. A., El-Morsi, M. S., Nosier, M. A., and Mahmoud, N. A. (2010). Heat transfer performance of a newly developed ice slurry generator: A comparative study. *Ain Shams Engineering Journal*, 1(2):147–157.
- Nelson, D. J., Vick, B., and Yu, X. (1996). Validation of the algorithm for ice-on-pipe brine thermal storage systems. *ASHRAE Transactions*, 102(1):55–62.
- Neto, J. H. and Krarti, M. (1997a). Deterministic model for an internal melt ice-on-coil thermal storage tank. *ASHRAE Transactions*, 103(1):113–124.

- Neto, J. H. and Krarti, M. (1997b). Experimental validation of a numerical model for an internal melt ice-on-coil thermal storage tank. *ASHRAE Transactions*, 103(1):125–138.
- Philippen, D., Caffish, M., Brunold, S., and Haller, M. Y. (2016). *ReSoTech - Reduction of Market Prices of Solar Thermal Systems due to New Technological Approaches – Phase 1: Analysis of Potentials and Possible*. Institut für Solartechnik SPF for Swiss Federal Office of Energy (SFOE), Research Programme Solar Heat and Heat Storage, CH-3003 Bern.
- Philippen, D., Carbonell, D., Granzotto, M., Zenhäusern, D., Haller, M. Y., and Brunold, S. (2015). *High-Ice - System development for high solar thermal gains with ice storage and heat pump*. Institut für Solartechnik SPF for Swiss Federal Office of Energy (SFOE), Research Programme Solar Heat and Heat Storage, CH-3003 Bern.
- Philippen, D., Carbonell, D., Haller, M. Y., Frank, E., and Brunold, S. (2014). Auslegung und Betrieb einer hocheffizienten Solarthermie-Wärmepumpen-Heizung mit Eisspeicher. In *24. OTTI Symposium Thermische Solarenergie*, Kloster Banz, Germany.
- Philippen, D., Haller, M. Y., Logie, W., Thalmann, M., Brunold, S., and Frank, E. (2012). Development of a heat exchanger that can be de-iced for the use in ice stores in solar thermal heat pump systems. In *Proceedings of EuroSun*, Rijeka and Opatija, Croatia. International Solar Energy Society (ISES).
- Pronk, P., Meewisse, J. M., Ferreira, C. A. I., and Witkamp, G. J. (2003). Ice slurry production with a circulating fluidized bed heat exchanger. In *International Congress of Refrigeration*, Washington D.C., USA.
- Stephan, P. (2006). *VDI-Wärmeatlas*. VDI e.V. | Springer.
- Swiss Federal Council (2013). Botschaft zum ersten massnahmenpaket der energiestrategie 2050. Technical Report 2013-0462.
- VDI (2012). *VDI-Richtlinie, Economic efficiency of building installations, Fundamentals and economic calculation, Part 1*.
- Vick, B., Nelson, D. J., and Yu, X. (1996). Model of an ice-on-coil brine thermal storage component. *ASHRAE Transactions*, 102(1):45–54.
- Wijeyesundera, N. E., Hawlader, M. N. A., Andy, C. W. B., and Hossain, M. K. (2004). Ice-slurry production using direct contact heat transfer. *International Journal of Refrigeration*, 27(5):511–519.
- Zhang, X. J., Qiu, L. M., Zhang, P., Liu, L., and Gan, Z. H. (2008). Performance improvement of vertical ice slurry generator by using bubbling device. *Energy Conversion and Management*, 49(1):83–88.